

---

# **Surface Stress, Kinetics, and Structure of Alkanethiol Self-Assembled Monolayers**

---

**Michel Godin**

Department of Physics  
McGill University  
Montréal, Québec  
Canada  
August, 2004

A Thesis submitted to  
McGill University  
in partial fulfillment of the requirements for the degree of  
Doctor of Philosophy

© Michel Godin, 2004



Library and  
Archives Canada

Bibliothèque et  
Archives Canada

Published Heritage  
Branch

Direction du  
Patrimoine de l'édition

395 Wellington Street  
Ottawa ON K1A 0N4  
Canada

395, rue Wellington  
Ottawa ON K1A 0N4  
Canada

*Your file    Votre référence*

*ISBN: 0-494-12848-8*

*Our file    Notre référence*

*ISBN: 0-494-12848-8*

#### NOTICE:

The author has granted a non-exclusive license allowing Library and Archives Canada to reproduce, publish, archive, preserve, conserve, communicate to the public by telecommunication or on the Internet, loan, distribute and sell theses worldwide, for commercial or non-commercial purposes, in microform, paper, electronic and/or any other formats.

The author retains copyright ownership and moral rights in this thesis. Neither the thesis nor substantial extracts from it may be printed or otherwise reproduced without the author's permission.

#### AVIS:

L'auteur a accordé une licence non exclusive permettant à la Bibliothèque et Archives Canada de reproduire, publier, archiver, sauvegarder, conserver, transmettre au public par télécommunication ou par l'Internet, prêter, distribuer et vendre des thèses partout dans le monde, à des fins commerciales ou autres, sur support microforme, papier, électronique et/ou autres formats.

L'auteur conserve la propriété du droit d'auteur et des droits moraux qui protègent cette thèse. Ni la thèse ni des extraits substantiels de celle-ci ne doivent être imprimés ou autrement reproduits sans son autorisation.

---

In compliance with the Canadian Privacy Act some supporting forms may have been removed from this thesis.

Conformément à la loi canadienne sur la protection de la vie privée, quelques formulaires secondaires ont été enlevés de cette thèse.

While these forms may be included in the document page count, their removal does not represent any loss of content from the thesis.

Bien que ces formulaires aient inclus dans la pagination, il n'y aura aucun contenu manquant.

  
**Canada**

# Table of Contents

<b>TABLE OF CONTENTS.....</b>	<b>III</b>
<b>ABSTRACT.....</b>	<b>V</b>
<b>RÉSUMÉ.....</b>	<b>VII</b>
<b>ACKNOWLEDGMENTS .....</b>	<b>IX</b>
<b>STATEMENT OF ORIGINALITY.....</b>	<b>XI</b>
<b>1 INTRODUCTION .....</b>	<b>1</b>
<b>2 CANTILEVER-BASED SENSING.....</b>	<b>5</b>
2.1 CANTILEVER-BASED SENSING APPLICATIONS .....	8
2.1.1 <i>Surface Stress Sensing</i> .....	8
2.1.2 <i>Heat Sensing</i> .....	11
2.1.3 <i>Mass Sensing</i> .....	13
2.1.4 <i>Mixture Detection</i> .....	14
2.2 SURFACE STRESS .....	15
2.2.1 <i>Definition</i> .....	17
2.2.2 <i>Measurement of Surface Stress</i> .....	19
<b>3 EXPERIMENTAL METHODS .....</b>	<b>20</b>
3.1 DIFFERENTIAL CANTILEVER-BASED SENSOR.....	20
3.1.1 <i>Cantilevers</i> .....	22
3.1.2 <i>Deflection Sensing</i> .....	25
3.1.3 <i>Cell</i> .....	31
3.1.4 <i>Analyte Introduction</i> .....	32
3.1.5 <i>Cell Volume and Alkanethiol Vapor Diffusion</i> .....	33
3.1.6 <i>Alkanethiol Purity</i> .....	36
3.1.7 <i>Reference Cantilever Preparation</i> .....	38
3.1.8 <i>Temperature Control</i> .....	40
3.2 COMBINED ELLIPSOMETRY AND CANTILEVER-BASED SENSING .....	42
3.2.1 <i>Setup</i> .....	42
3.3 SCANNING TUNNELING MICROSCOPY .....	47
3.4 SAMPLE PREPARATION .....	48
<b>4 CALIBRATION.....</b>	<b>52</b>
4.1 CANTILEVER DEFLECTION MEASUREMENT .....	53
4.1.1 <i>Deflection Calibration: Simple Method</i> .....	53
4.1.2 <i>Deflection Calibration: Fiber Interferometer</i> .....	54
4.1.3 <i>Implementation</i> .....	57
4.2 QUANTIFYING SURFACE STRESS.....	60
4.2.1 <i>Methodology</i> .....	60
4.2.2 <i>Implementation</i> .....	65
4.3 INSTRUMENT SENSITIVITY AND RESOLUTION .....	67
<b>5 ALKANETHIOL SELF-ASSEMBLED MONOLAYERS .....</b>	<b>69</b>
5.1 CHEMICAL SELF-ASSEMBLY .....	69
5.2 KINETICS OF ALKANETHIOL SAM FORMATION .....	72
5.3 SURFACE STRESS OF ALKANETHIOL SELF-ASSEMBLED MONOLAYERS .....	76

5.3.1	<i>Effect of Gold Surface Morphology</i> .....	77
5.3.2	<i>Features in the Kinetics of SAM Formation</i> .....	85
5.3.3	<i>Diffusion Effect on SAM Formation</i> .....	87
5.3.4	<i>Aging of Gold Substrate</i> .....	92
5.3.5	<i>Sensor Drift</i> .....	93
5.4	SUMMARY AND IMPLICATIONS ON CANTILEVER-BASED SENSORS .....	95
<b>6</b>	<b>ORIGINS OF SURFACE STRESS</b> .....	<b>97</b>
6.1	MOTIVATION .....	97
6.2	CHAIN LENGTH INDEPENDENCE OF SURFACE STRESS.....	98
6.3	GOLD GRAIN SIZE EFFECTS ON SURFACE STRESS.....	100
6.4	MODELING.....	102
6.4.1	<i>Chain-Chain Interactions: Van der Waals</i> .....	102
6.4.2	<i>Electrostatic Repulsion Model</i> .....	108
6.4.3	<i>Discussion</i> .....	113
6.5	SUMMARY/DISCUSSION .....	116
<b>7</b>	<b>SUMMARY AND OUTLOOK</b> .....	<b>119</b>
7.1	SUMMARY.....	119
7.2	OUTLOOK.....	122
	<b>APPENDIX</b> .....	<b>127</b>
	<b>REFERENCES</b> .....	<b>130</b>

---

## Abstract

---

The surface stress induced during the formation of alkanethiol [HS(CH<sub>2</sub>)<sub>n</sub>CH<sub>3</sub>] self-assembled monolayers (SAMs) on gold from the vapor phase was measured using a differential cantilever-based sensor. This custom-built system is capable of surface stress measurements with a sensitivity of  $5 \times 10^{-5}$  N/m using commercially-available atomic force microscopy cantilevers. A second system combining cantilever-based sensing and ellipsometry was also designed and built, capable of yielding simultaneous *in situ* surface stress and film thickness measurements. Scanning tunneling microscopy (STM) with molecular resolution was also performed *ex situ* in order to characterize the structure of the resulting SAMs. The complementary use of these tools has provided an all-around view of the self-assembly process.

These measurements were performed in order to gain insight into the mechanisms involved in the self-assembly process and into the origins of the associated surface stress. Moreover, these studies were used to characterize and optimize the response of cantilever-based sensors based on functionalized SAM technology in terms of reliability, sensitivity, and reproducibility.

The evolution of the surface stress induced during alkanethiol SAM formation reveals features associated with coverage-dependent structural phase transitions. These results show that both the kinetics of SAM formation and the resulting SAM structure are strongly influenced by the surface structure of the underlying gold substrate, by the impingement rate of the alkanethiol molecules onto the gold surface, and by the cleanliness of the gold surface. In particular, it was found that a minimum gold grain size is necessary in order for the SAM to achieve the standing-up phase, for which large compressive surface stresses ( $\sim 10$  N/m) are measured. In addition, these results show that alkanethiol SAMs can

become kinetically trapped in metastable intermediate states (lying-down phase) for formation on small-grained gold surfaces and/or at low alkanethiol vapor concentrations. Theoretical modeling of the origins of the induced surface stress reveals that inter-molecular Lennard-Jones interactions and electrostatic repulsion between adsorbed species play minimal roles in the development of the surface stress. Changes in the electronic structure of the underlying gold substrate are more likely to account for the large compressive surface stresses observed during alkanethiol SAM formation.

---

## Résumé

---

La tension de surface associée à la formation de monocouches auto-assemblées d'alcanethiol  $[\text{HS}(\text{CH}_2)_n\text{CH}_3]$  sur des surfaces d'or a été mesurée à l'aide d'un microlevier utilisé comme capteur chimique. Ce système de détection chimique bénéficie d'une sensibilité de  $5 \times 10^{-5}$  N/m. Un second système combine ce type de capteur chimique et un ellipsomètre, offrant la capacité de produire des mesures simultanées de tension de surface et d'épaisseur lors de l'adsorption moléculaire sur une surface. La microscopie à balayage à effet tunnel (STM), donnant accès à de l'information structurale à l'échelle moléculaire, complète la gamme d'instruments utilisée à fin d'étudier les phénomènes associés à l'auto-assemblage moléculaire.

Cette étude a été réalisée dans le but d'établir une compréhension générale des mécanismes impliqués lors de la formation de monocouches auto-assemblées et de déterminer l'origine de la tension de surface y étant associée. De plus, ces mesures nous permettent de caractériser et d'optimiser la performance en terme de fiabilité et de sensibilité de ces nouveaux types de capteurs chimiques.

La mesure de la tension de surface procure de l'information sur les différentes transitions de phases structurales observées lors de la formation de monocouche d'alcanethiol. Nous avons établi que la morphologie de la surface d'or, la concentration gazeuse d'alcanethiol, ainsi que la propreté de l'or ont une grande influence sur la cinétique de formation et sur la structure finale de ces monocouches. En effet, une grosseur de grains d'or minimale est nécessaire afin que la monocouche puisse atteindre la phase finale « debout » caractéristique d'une monocouche de haute qualité, dont la tension de surface se mesure à environ -10 N/m, tandis que la formation sur de plus petits grains et/ou formées à plus faible concentration résulte en une monocouche de moindre qualité.

produisant une tension de surface considérablement plus petite. Une interprétation théorique de l'origine de cette tension de surface révèle que les interactions inter-moléculaires de type Lennard-Jones et électrostatique ne peuvent produire la grande tension de surface observée. Des changements dans la distribution électronique de la surface d'or, induite par l'adsorption d'alcanethiol, sont sans doute à l'origine de la tension de surface mesurée.



---

## Acknowledgments

---

I would like to acknowledge the support of a number of people who have contributed to the development of this thesis and to my overall experience as a graduate student at McGill University.

Firstly, I would like to sincerely thank my supervisor, Dr. Peter Grütter, for giving me the opportunity to work on this interesting project. His enthusiasm, support, and insightful guidance made a considerable impact on my success during my graduate studies. He gave me the freedom to explore new ideas while keeping me focused on my goals.

I must thank my colleague and friend, Vincent Tabard-Cossa, for his day-to-day input. I am indebted to him for many hours of fruitful discussions concerning all aspects of my project. His guidance and support helped me establish and attain my goals.

Dr. Peter Williams' contribution to this project and to my overall graduate studies must be emphasized. I had the opportunity to work alongside him during his 10 month sabbatical stay at McGill. His enthusiasm, work ethic and sense of humor had a great impact on many of us in the laboratory. His logical approach to research is exemplary and led me down new paths. I must also thank Dr. Luc Beaulieu for his contribution to this project as a post-doctoral member of our group. His down-to-earth approach to research and his untiring work ethic were inspirational. I also thank Dr. Bruce Lennox for sharing the chemists' perspective on this project.

Brian Seivewright, Dr. Hélène Bourque, Olivier Laroche all deserve to be recognize for their input through useful discussions and technical help on several

aspects of this project. I must also acknowledge all of the group members that I have worked with in the lab over the years. Although too many to name individually, they all deserve recognition for their help and friendship.

Dr. Chao-Cheng Kaun and Professor Hong Guo deserve my thanks for helpful discussions and calculations concerning some of the more theoretical aspects of this project.

I also thank Robert Gagnon, Eddie Del Campo, Steve Kecani, and Frank Van Gils for their help in terms of samples preparation and/or for their assistance in the machine shop. Much appreciation goes out to the administrative staff of the main office for their efficient problem-solving skills. For their financial assistance, I would like to thank Dr. Peter Grütter, « Le Fonds Québécois de la Recherche sur la Nature et les Technologies » (doctoral fellowship), and McGill University (fellowship).

Most importantly, I thank my wife Karine and my family for their continual support and encouragement throughout my studies. Merci!

---

## Statement of Originality

---

The author claims the following aspects of the thesis constitute original scholarship and an advancement of knowledge. Some of these findings have been published [57,97,138].

- The design, construction, and commissioning of a differential cantilever-based sensor, and of a combined cantilever-based sensor and ellipsometer. The first system uses commercially-available atomic force microscope cantilevers and is capable of quantitative surface stress measurements with a sensitivity of  $5 \times 10^{-5}$  N/m. This system uses one cantilever as an active sensor, and a second dodecanethiol self-assembled monolayer-covered cantilever used as a reference. The second system is capable of providing simultaneous *in situ* surface stress and film thickness measurements. This unique system provides complementary information used in the study of molecular adsorption on surfaces.
- Development of a methodology used to convert a measured cantilever deflection into a measure of surface stress. This methodology overcomes a major limitation inherent in Stoney's formula, specifically the need to know the cantilever's Young's modulus, which has been shown to have a large degree of uncertainty for the case of commonly-used silicon nitride cantilevers. This new method replaces the need to know Young's modulus of the cantilever material by using the cantilever's spring constant, which is easily measurable.
- The measurement of the compressive surface stress induced during the formation of high-quality alkanethiol self-assembled monolayers (SAM) on Au(111). It was established that there is a strong correlation between

the morphology of the underlying gold surface and the measured surface stress. This correlation was attributed to the fact that the resulting SAM structure was of a much higher quality when formed on an Au(111) surface exhibiting large grains, as opposed to those formed on smaller-grained gold. In fact, SAM formation on smaller-grained gold remained in a metastable structural phase (stacked lying-down phase), not able to undergo the transition into the final standing-up phase. The surface stress associated with a high-quality SAM was found to be at least an order of magnitude larger than that of a SAM formed on small-grained gold.

- These metastable SAMs formed on small-grained gold surfaces were found to be further kinetically trapped when formed at low alkanethiol vapor concentrations. Self-assembled monolayers formed on small-grained gold from the vapor phase were found to remain in an unstacked lying-down phase when formed at low vapor concentrations. This is evident from real-time surface stress profile, as they exhibit a characteristic release in surface stress. The monolayers formed on the same type of gold surfaces under similar conditions but at higher alkanethiol vapor concentrations were able to undergo the transition into the higher density stacked lying-down phase, but still unable to undergo the transition into the standing up phase.
- The surface stress induced as the result of the formation of high-quality alkanethiol SAMs was measured as a function of molecular chain length for hexanethiol (C6), octanethiol (C8), and decanethiol (C10). It was found that there is no chain length dependence, in contradiction with the only previously published report on the subject.
- The surface stress induced as the result of alkanethiol SAM formation was measured as a function the underlying gold surface grain size. It was

found that the measured surface stress increases linearly with gold surface grain area.

- The theoretically expected surface stress resulting from electrostatic repulsion between adsorbed alkanethiols was calculated. It was found that this electrostatic contribution to the overall surface stress account for only part (10% at best) of the overall measured surface stress.
- The large compressive surface stress associated with alkanethiol SAM formation was attributed as being the driving force responsible for the creation of vacancy islands (etch pits) commonly observed on SAM-covered Au(111) by scanning tunneling microscopy.



# 1 Introduction

Molecular self-assembly is at the heart of many physical, chemical and biological processes. Nature routinely uses self-assembly to make complex structures ranging from living biological organisms to crystals given the right environmental conditions. Following nature's lead, scientists are increasingly looking into using self-assembly to make structures for a multitude of applications. The idea of building structures from the bottom-up, molecule by molecule or atom by atom, is one of the core concepts of nanoscience and promises to revolutionize many industries. For example, researchers in the field of molecular electronics are investigating the use of molecular self-assembly to build new types of transistors and switches that could potentially replace today's dependence on silicon electronics [1,2,3]. The pharmaceutical industry is also pushing hard to find ways to use self-assembly to increase the efficiency of drug delivery processes [4]. Other industries are seeking to use self-assembled monolayers (SAM) as protective layers to chemically functionalize a surface to control its reactivity [5,6]. However, if self-assembly is to become a useful technology, it is imperative to understand the fundamental mechanisms that drive this process, both from a kinetics and structural point of view. A micromechanical cantilever-based sensor was used to measure the surface stress induced during the formation of self-assembled monolayers. This type of measurement is aimed at gaining some insight into the origins of the induced stresses and inter-molecular forces involved during the formation of these self-assembled structures. An understanding of the driving forces involved during chemical self-assembly is imperative as scientists seek to build devices on the molecular scale.

The advent of atomic force microscopy (AFM) in the mid-1980s [7] has revolutionized the study of surfaces to an extent where it is now possible to probe surfaces on an atomic and sub-atomic level [8]. AFM micro-mechanical cantilevers are designed and used in a variety of microscopy applications probing electrostatic, magnetic, and electronic forces on surfaces. AFM micro-cantilevers have also found a place in many other sensing applications. Instead of utilizing the cantilever's tip as a probe, researchers have taken advantage of the entire cantilever body's compact geometry for a multitude of sensing applications. Several new techniques aimed at measuring nanoscale quantities of mass, heat, radiation, etc. have been developed as a result of the commercial availability of AFM cantilevers [9].

Chemical sensing of numerous target molecules is achieved using micro-mechanical cantilever-based sensors. It is possible to sensitize one surface of a cantilever differently than the opposing surface. When the target molecule of interest interacts with the sensitized surface, a surface stress is induced, and the cantilever bends due to the different surface stresses acting on both sides of the cantilever. Chemical sensing is achieved by monitoring the deflection of the sensitized cantilever. The sensor's specificity, that is to say the sensitivity of the sensor to a specific target molecule, is determined by the chemical functionalization of the sensitized surface of the cantilever. Immobilization of specific receptors on the cantilever surface can be achieved in a number of ways. Very specific surface functionalizations have been achieved using molecular self-assembled monolayers as sensing layers assembled on the cantilever's surface, as discussed in *Chapter 2*. Thiol-chemistry has been favored as a versatile method of sensitizing a surface. Alkanethiol molecules  $[\text{HS}(\text{CH}_2)_n\text{CH}_3]$  spontaneously form robust ordered monolayers on gold surfaces [10]. Chemical synthesis techniques have been developed to chemically modify these alkanethiol molecules by changing the end group from methyl to many other chemical groups. When these functionalized SAMs form on a gold surface, these modified end groups line-up at the SAM/air or SAM/liquid interface, and can act as chemical receptor



sites that interact with specific molecular targets. The functionalized SAM-modified cantilevers become versatile sensors tailored to sense very specific target molecules.

A cantilever-based chemical sensor was used to measure the surface stress induced during the formation of (non-functionalized) alkanethiol SAMs on gold-coated cantilevers in an effort to obtain a fundamental understanding of the sensor's response. The self-assembly of alkanethiol monolayers is seen as model system for many self-assembled systems due to the SAM's stability, its relatively simple chemical composition, and its versatility as a sensing layer when chemically functionalized. Berger *et al* [11] were the first to measure the surface stress associated with alkanethiol SAM formation. They experimentally determined that the induced surface stress increased with alkanethiol chain length. The present work was initiated to characterize this chain length dependence in an effort to understand and optimize the response of cantilever-based sensors. An understanding of the fundamental origins of the induced surface stress in this model system is essential in the design and optimization of cantilever-based sensors. The response of the cantilever-based sensor is characterized in terms of various environmental parameters, including substrate morphology (Au grain size), alkanethiol chain length, surface cleanliness, and analyte introduction conditions and concentration. Experimental techniques complementary to surface stress sensing, such as scanning tunneling microscopy (STM) and ellipsometry, were used to gain an appreciation of the mechanisms that drive alkanethiol self-assembly and the induced surface stress, which will translate into a better understanding of molecular systems involved in other sensing applications.

This work begins with a review of the different types of cantilever-based sensors developed and found in the literature. An overview of the definition of surface stress and its relation to the adsorption of atoms or molecules on a surface are also included in Chapter 2. Chapter 3 described the experimental methods used in this study. The design and development of a differential cantilever-based sensor and

of a combined cantilever-based sensor and ellipsometer are described. A description of scanning tunneling microscopy imaging and sample preparation procedures are included as well. The following chapter describes the calibration procedures used to convert the measured cantilever sensor signal into an actual deflection, and the subsequent conversion of this deflection into an accurate measure of surface stress. Chapter 5 introduces and reviews the concept of molecular self-assembly with emphasis on the experimental measurement of the surface stress induced during the formation of alkanethiol self-assembled monolayers. The effects of gold surface morphology (grain size), analyte concentration, and substrate contamination on the self assembly process of these monolayers are investigated. Chapter 6 reveals the alkanethiol chain length and gold grain size dependences on the measured surface stress. Theoretical modeling used to infer the origins of this induced surface stress follows. Chapter 7 concludes this work and offers an outlook.

## 2 Cantilever-Based Sensing

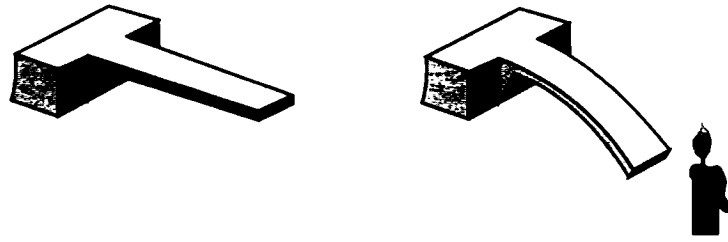
The field of chemical sensing generates a great deal of interest since it encompasses such a wide variety of applications, including medical and pharmaceutical screening, detection of the quality/freshness of food, chemical analysis, etc. The sensing community is constantly seeking ways to design new sensors with higher sensitivities, faster response times, improved chemical selectivity and low cost. Cantilever-based sensing is emerging as a capable sensing platform with the advantage of being relatively cheap to mass-produce. Micro-fabrication technologies have allowed for the design of micro-cantilevers optimized for various types of sensing applications, as well as for the manufacturing of large arrays of cantilevers, making it possible to use various sensors in parallel. These cantilever-based sensors are proving to be quite competitive with current sensing technologies with their high sensitivity and fast response time given their small size (~micrometers). A few companies, such as Concentris [12], Veeco [13], and Graviton [14], have begun commercial development of such cantilever-based sensing technologies.

The commercial availability of atomic force microscope (AFM) micro-cantilevers has fueled the development of various cantilever-based sensing applications. AFM cantilevers are commonly used with an integrated sharp tip at their apex. AFM imaging consists of scanning this integrated tip over a surface while monitoring the cantilever's deflection. These deflections arise due to tip-sample interactions typically resulting from attractive and repulsive electrostatic, van der Waals or magnetic forces. In *static* mode, the deflection of the cantilever is monitored as it bends in response to forces acting on the tip. In *dynamic* mode,

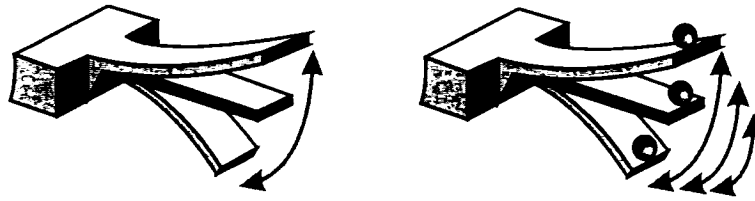
the cantilever's resonance frequency is monitored as it changes also due to tip-sample interactions. The resulting AFM image yields a three-dimensional profile of these tip-sample interactions. But in many sensing applications, the cantilever is used without the use of a tip (not scanned over a surface), by simply using its body or surface properties to probe nanoscale phenomena. Cantilever-based sensing involves the transduction of some particular chemical or physical interaction occurring on the cantilever surface into a mechanical deflection or resonant frequency shift of the cantilever. Commercially-available AFM cantilevers have proven to be quite versatile as evidenced by the recent outpouring of potential sensing applications, as discussed below. The cantilever-based sensors used in the present work were used in *static* mode.

This chapter lists some of the most common cantilever-based sensing applications, as depicted in Figure 2.1 [9], with emphasis placed on cantilever-based surface stress sensors. A general overview of surface stress concludes the chapter.

## Heat Sensing



## Mass Sensing



## Surface Stress Sensing

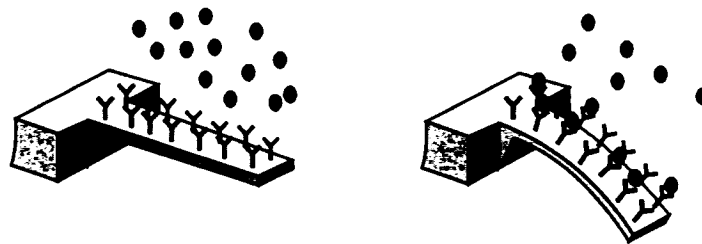
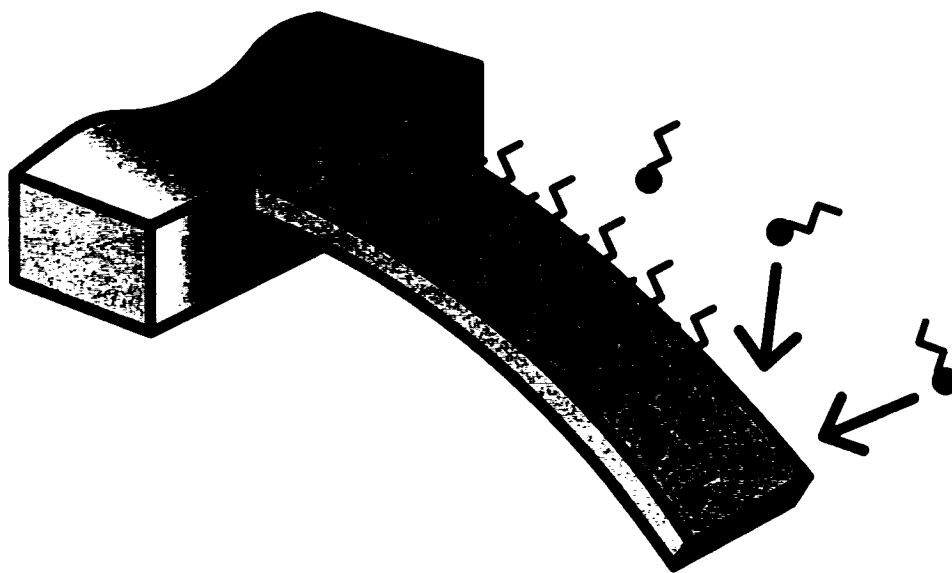


Figure 2.1: Cantilever-based sensors can be used in a variety of different modes. Heat sensing is achieved by using the bimetallic effect. Mass sensing is done by monitoring changes in the cantilever's resonant frequency upon mass loading. Surface stress sensing is achieved by monitoring the static deflection of the cantilever resulting from molecular adsorption-induced surface stresses.

## 2.1 Cantilever-Based Sensing Applications

### 2.1.1 Surface Stress Sensing

In most cantilever-based sensing applications, one surface of the cantilever beam is rendered sensitive to a specific target molecule of interest, while the opposing surface is chemically passivated. When these target molecules interact with the sensitized surface of the cantilever, a surface stress can be induced. The difference in surface stress induced on the sensitive relative to the passive surface of the cantilever results in a measurable mechanical deflection. Cantilever deflections are monitored as a direct measure of adsorption-induced surface stress. Figure 2.2 schematically shows molecularly induced surface stress bending a cantilever beam.



**Figure 2.2:** A cantilever beam acts as a chemical sensor by transducing the adsorption of a target molecule onto one of its surfaces into a measurable deflection.

The sensing layer applied to the cantilever surface is chosen to promote the adsorption of specific target molecules, which in turn can induce a surface stress.

Cantilever surface functionalization determines the specificity of the sensor. These sensing coatings can be whatever promotes molecule adsorption through specific binding, from simple metallic coatings to more complex chemically functionalized molecular monolayers. The present work focuses on sensing the self-assembly of alkanethiol monolayers on gold-coated cantilevers. In this case, the sensing layer is a thin gold film deposited on one surface of the cantilever, and the target molecules to be detected are alkanethiols. The opposing passive surface is bare silicon nitride (cantilever material), requiring no further passivation. Functionalized alkanethiol SAMs can also be used as the sensing layer when formed on the gold-coated cantilever surface, as depicted in Figure 2.3. Specificity of this sensing layer is determined by the chemical endgroups present at the monolayer/gas (/liquid) interface. The functionalized SAM used as the sensing layer on the cantilever surface is both receptive (sensitized to react with target molecules) and responsive (by allowing the transduction of the surface stress to the cantilever beam) [15,16,17,18]. In an alternative configuration, thiolated receptors capture the target analyte in solution. When these thiolated species bind to a gold-coated cantilever, the induced surface stress will vary as a function of the analyte concentration. In any case, an understanding of the origins of the surface stress in these thiolated systems will lead to better design and optimization of this class of sensors.

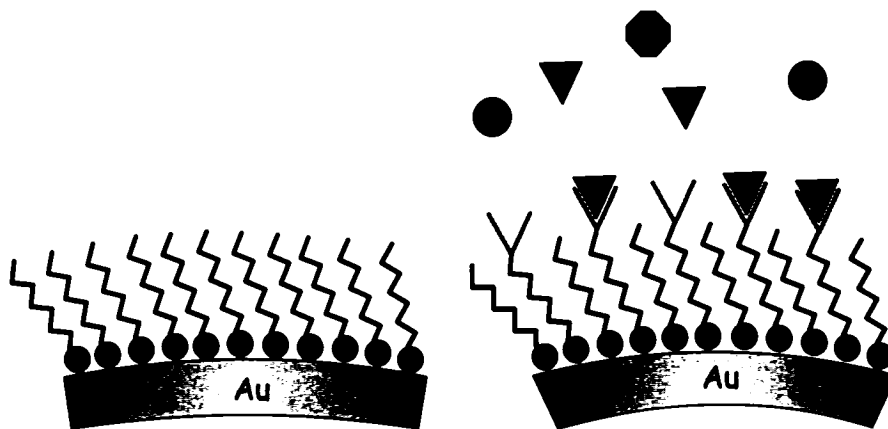


**Figure 2.3:** Depiction of an alkanethiol SAM and a functionalized SAM used as a sensing layer. Receptor groups can be immobilized on a gold surface using thiol chemistry. In this case, the receptors only interact with ‘green triangular’ molecules, and nothing else. This functionalized SAM can be formed on a gold-coated cantilever, turning it into a sensor sensitive to specific target molecules.

Other surface stress-based sensors involve the *absorption* of target molecules, as opposed to *adsorption*, into a film present on the cantilever surface. Absorption-based sensing involved the penetration of target molecules into the sensing layer which has been deposited on the cantilever surface. This interaction involves a swelling of the sensing layer inducing a surface stress which, as before, is measured as a deflection of the cantilever. Although the origins of the surface stress are different, the working principle of the sensor is similar. Several groups have used absorption-based sensing in developing cantilever-based sensors. The absorption of alcohol vapors into polymer-coated cantilevers has been investigated [19,41]. Alcohol vapor identification can be achieved since different alcohols have different diffusion rates into different polymers films. Baselt *et al* [20] achieved hydrogen sensing by coating a cantilever with a thin palladium film. The palladium film catalyzes the breakdown of molecular hydrogen into atomic hydrogen, which then absorbs readily into the film, causing it to swell.



### 2.1.1.1. Other Molecular Sensing Examples

Advances in synthesis chemistry have allowed for the design of SAMs functionalized to favor interactions with very specific molecules. Several groups [15,21,22,23] have used cantilever-based sensing for DNA sequencing applications. Oligonucleotides, or single-stranded DNA (ssDNA) are covalently immobilized on a gold-coated cantilever by means of thiol chemistry. When the complementary ssDNA are exposed to the functionalized cantilever, they hybridize (forms double-stranded DNA) with the ssDNA SAM inducing a surface stress which is measured as a deflection of the cantilever. These DNA sensors have been shown to be able to distinguish 12-mer ssDNA strands differing by only one base pair. The sensor can be reused by denaturing the newly-formed DNA molecule. One can easily imagine that an array of cantilevers could be micro-fabricated such that every cantilever could be sensitive to different ssDNA sequences. This technology would provide a label-free alternative to current DNA chips [24].

A similar methodology has been used in other applications including the sensing of proteins and other biological species. Immobilization of the proper antibodies to the cantilever surface has allowed for the detection of cardiac biomarker proteins (creatin kinase and myoglobin) [25] in an effort to enhance cardiac disease screening. Other medically-relevant applications include the sensing of prostate-specific antigen [26] for prostate cancer diagnosis, glucose biosensing [27], sensing of the pesticide DDT (dichlorodiphenyltrichloroethane) [28], and pH sensing [16].

### 2.1.2 Heat Sensing

AFM cantilevers can be used as precise thermometers or calorimeters by exploiting the bimetallic effect. If the cantilever beam is coated by a material having a different coefficient of thermal expansion than that of the material

making up the cantilever itself, it will undergo a deflection as a result of temperature changes. The deflection of a rectangular cantilever,  $\Delta z$ , resulting from a change in temperature,  $\Delta T$ , is expressed as [29]:

$$\Delta z = \frac{3}{t_c^2 K} (\alpha_b - \alpha_c) (t_b + t_c) l^2 \Delta T \quad \text{Equation 2.1}$$

where  $l$  is the rectangular cantilever's length,  $\alpha_b$ ,  $\alpha_c$ ,  $t_b$  and  $t_c$  are the thermal expansion coefficients and the thicknesses of the cantilever beam and of the cantilever's coating, respectively, whereas  $K$  is expressed as:

$$K = 4 + 6 \left( \frac{t_b}{t_c} \right) + 4 \left( \frac{t_b}{t_c} \right)^2 + \frac{E_b}{E_c} \left( \frac{t_b}{t_c} \right)^3 + \frac{E_c}{E_b} \left( \frac{t_c}{t_b} \right) \quad \text{Equation 2.2}$$

where  $E_b$  and  $E_c$  are Young's modulus of the cantilever and of the coating, respectively. As an example, a gold-coated silicon rectangular cantilever, where  $l = 320 \mu\text{m}$ ,  $t_b = 0.6 \mu\text{m}$ ,  $t_c = 100 \text{ nm}$ ,  $\alpha_b = 3 \times 10^{-6} \text{ }^\circ\text{C}^{-1}$ ,  $\alpha_c = 14.2 \times 10^{-6} \text{ }^\circ\text{C}^{-1}$ ,  $E_b = 47 \text{ GPa}$  and  $E_c = 78 \text{ GPa}$ , a temperature change of  $1 \text{ }^\circ\text{C}$  results in a cantilever deflection of  $766 \text{ nm}$ . A temperature sensitivity of  $10^{-5} \text{ }^\circ\text{C}$  can be achieved by optimally tuning some of the above parameters and assuming a minimum deflection sensitivity of  $0.01 \text{ nm}$  [30]. Although such temperature sensitivity is great when the cantilever is used as a thermometer, one must be careful to minimize these thermal effects where the cantilever is used in other sensing modes.

The use of the bimetallic effect can be utilized to transform the cantilever into a sensitive calorimeter. The cantilever deflection resulting from the absorption of heat, either at a localized spot on the cantilever, or along its entire length, can be modeled [31]. The small size and heat capacity of micro-cantilevers makes them remarkable calorimeters with picojoule sensitivities and millisecond time resolution [32], as compared to conventional differential scanning calorimeters

which typically have 0.2 mJ sensitivities or to infrared detection techniques [33] having a 6 nJ sensitivity, both with time resolutions on the order of seconds.

Cantilever-based calorimetry has been used to measure enthalpy changes in picoliter volumes of solid samples during phase transitions of n-alkanes [34], and to investigate the thermal properties of metal clusters [35], for example. The layer coating the cantilever can also be catalytically active, such that heat generated directly on the surface of the cantilever due to some chemical reaction can be detected as a bimetallic deflection of the cantilever. One such example is the case of a platinum-coated cantilever, which facilitates the reaction of hydrogen and oxygen to form water [36]. A method known as photothermal spectroscopy provides a way to obtain chemical information on molecules adsorbed on the surface of a cantilever. The energy of photons impinging on the surface of the cantilever will partly be converted into heat (depending on the surface's chemical composition), which can be detected as a bimetallic bending. Barnes *et al* [37] have used this method with 100 pW power sensitivity. The bimetallic effect has also been applied to cantilever beams in the design of ultra-sensitive explosive detectors, with possible uses for land-mines detection and airport screening.

### 2.1.3 Mass Sensing

Mass sensing is made possible by monitoring the resonant frequency changes of a cantilever beam resulting from mass loading. When molecules bind to a cantilever beam, its resonant frequency decreases as a result of the increase in total mass. A change in mass,  $\Delta m$ , can be measured by monitoring the change in the resonant frequency of the cantilever [38,40,107]. Mass sensitivities on the order of femtograms can be achieved using standard AFM micro-cantilevers [107].

A remarkable example of this technique comes from the work of Illic *et al* [38] who measured the mass a single E. Coli bacterium. The authors designed and micro-fabricated cantilevers specifically optimized for mass sensing. By coating the cantilever surface with the anti-E. Coli antibody, detection of a single bacterium with a mass of 665 fg was measured as the 4.6 kHz resonant frequency shift of a  $15 \times 5 \mu\text{m}$  (length  $\times$  width) rectangular silicon nitride cantilever. Gupta *et al* [39] micro-fabricated even smaller ( $4 \times 1 \mu\text{m}$ ) cantilevers used for the detection of a single vaccinia virus (9.5 fg) which is part of the Poxviridae family that forms the basis of the smallpox vaccine. Recently, Illic *et al* [40] have micro-fabricated nanoscale mass sensors with sub-attogram sensitivity. In principle, mass detection and surface stress sensing can be monitored simultaneously by monitoring both the static deflection and the changes in the resonant frequency of the cantilever.

#### 2.1.4 Mixture Detection

Arguably the most promising feature of the cantilever-based chemical sensor is the ability to relatively cheaply micro-fabricate cantilevers in arrays, making it possible to perform parallel chemical sensing. Array-based sensing has already been undertaken as a prototypical artificial nose by H. P. Lang *et al* [41]. An eight-cantilever system combined with pattern recognition software was used to identify various alcohol vapors and mixtures. The response of all eight cantilevers was monitored during exposure to various vapors. The associated combination of deflections represents “fingerprints” associated with the presence of specific alcohol vapors. Proper calibration can lead to an array-based system capable of quantifying the composition of vapor mixtures. These array-based sensors have multiple applications in a wide range of industries. Many examples exist in the medical and pharmaceutical industries, including the detection of various diseases by monitoring a patient’s blood chemistry or exhaled breath. For

example, monitoring the concentration of acetone in exhaled breath can be used for identifying diabetes mellitus in patients. [42].

## 2.2 Surface Stress

Surface stress [43,44] is a macroscopic quantity that is governed by microscopic processes. Although being a macroscopic quantity, the measurement of the surface stress involved in a system can lead to insight into the microscopic mechanisms responsible for the generation of surface stress without detailed knowledge of the atomistic processes involved. Recent investigations of surface reconstruction, interfacial mixing, and self-organization at solid surfaces have renewed interest in the study of surface stress [11,45,46,47,48]. Cantilever-based sensors can use surface stress as a transduction mechanism in chemical sensing, but can also be used as a means to characterize processes that occur at the molecular and atomic level. This section will review the concept of surface stress as it relates to its microscopic origins.

At the most basic level, surface stress arises when surface atoms or thin films undergo some dynamic micro-structural process resulting in a change in density while being rigidly attached to its substrate. If bond strengths between surface atoms are stronger than they are between sub-surface atoms (in the bulk), a *tensile* surface stress results as the attractive forces between these surface atoms would tend to curve the surface towards the surface, resulting in a concave surface curvature. In contrast, if surface atoms tend to repel each other, a *compressive* surface stress is induced, resulting in a convex surface curvature. Similarly, a thin film rigidly attached to a surface would create a tensile or compressive surface stress as it contracts or expands, respectively. Figure 2.4 illustrates the difference between tensile and compressive surface stress. The origins of surface stress can be quite different, from atomistic interactions between surface atoms, to inter-

molecular interactions between species adsorbed on a surface, to the expansion of a deposited thin film arising from temperature changes or phase transitions.

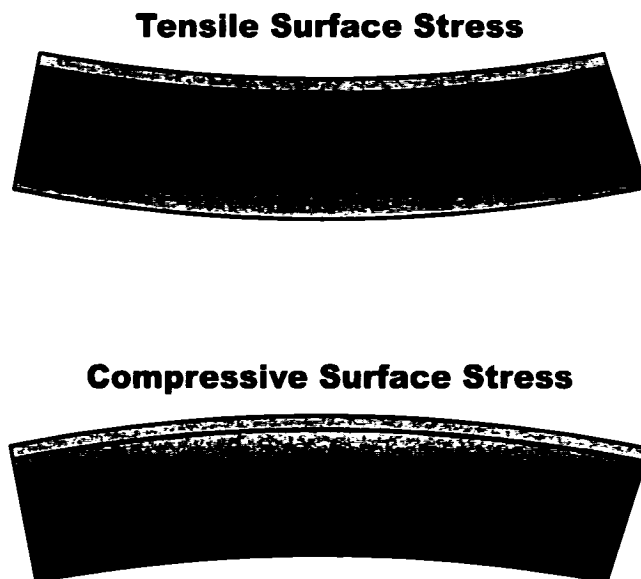


**Figure 2.4:** A tensile surface stress (positive surface stress) contracts the top surface of a thin plate inducing a concave curvature. A compressive surface stress (negative surface stress) expands the top surface of a thin plate inducing a convex curvature.

As a basic example, consider the native surface stress of clean metal surfaces. The surface atoms of a clean metal surface differ from atoms in the bulk of the metal by the fact that the surface atoms have less neighboring atoms to form bonds with. When a surface is created, electrons redistribute themselves in response to the absence of atoms above the surface; the charge distribution near the surface is different than what it is in the bulk of the material. If the charge density would be the same at the surface as it is in the bulk, no surface stress would develop. In the case of an Au surface, the inherent tensile surface stress is the result of a competition between the repulsive interactions between the filled d shells and an electron gas attraction from the mobile sp electrons [49]. At the Au surface, while the full d shells remain essentially unchanged, the resulting electron density corrugations (sp electrons) at the Au surface will effectively smooth off as a result of the inherent surface tension of the electron gas [50]. Consequently,

there is an increase in charge density between the surface atoms, resulting in a strengthening of the inter-atomic bonds between surface atoms causing an increase in tensile surface stress. This tensile surface stress can be large enough to initiate surface reconstruction [44]. In the case of Au(111), surface reconstruction occurs to compensate for this increase in surface charge density and to reduce the surface free energy. Specifically, the surface accommodates an additional Au atom in a  $(2\sqrt{3} \times \sqrt{3})$  reconstructed unit cell to compensate for the charge density increase and to relieve some of the native tensile surface stress. The adsorption of an adsorbate on a metal surface causes the electronic charge density to redistribute itself again away from the bulk of the substrate, and is typically associated with a compressive change in surface stress.

A similar interpretation has been used to explain the tensile surface stress occurring at Si(100) or Ge(100) surfaces [43,51]. The creation of a surface results in dangling bonds. The surface reconstructs forming Si or Ge dimers at the surface. The formation of dimers at the surface effectively reduces inter-atomic bond lengths, and results in a tensile surface stress. Molecular or atomic adsorption on surfaces can produce either compressive (Ge on Si(100) [52]) or tensile (As on Si(100) [53]) surface stresses depending on specific adsorbate/surface interactions. The mechanisms responsible for these surface stresses can be complex.

### 2.2.1 Definition

Surface stress is formally treated in tensor form via the surface stress tensor  $\sigma_{ij}$ . It is useful to consider the Shuttleworth equation [54] defining surface stress in term of surface energy,  $\gamma$ :

$$\sigma_{ij} = \gamma \delta_{ij} + \frac{\partial \gamma}{\partial \epsilon_{ij}}$$

Equation 2.3

where  $\delta_{ij}$  is the Kronecker delta and  $\varepsilon_{ij}$  is the elastic strain tensor. In order to understand the Shuttleworth equation (Equation 2.3), it is useful to consider two examples. For a liquid surface, surface stress and surface energy,  $\gamma$ , are equal since the second term of Equation 2.3 vanishes, as there is no resistance to plastic deformation at a liquid surface. When the surface is expanded, molecules flow from the interior of the liquid to the surface to compensate for the change in surface density. The result is that the local environment of surface molecules is the same before and after the expansion of the surface; the surface free energy does not change. For liquid interfaces, surface stress and surface free energy are equal, and are often called surface tension. For solid interfaces, the second term on the right-hand side of Equation 2.3 is not equal to zero. Qualitatively speaking, surface energy is related to changes in energy during plastic formation of a surface area, while surface stress is related to changes in energy during elastic stretching of a pre-existing surface.

The surface stress tensor assumes a rather simple form in most cases of interest. Since surface atoms in real surfaces are free to relax in the direction perpendicular to the surface, no stress can build up in this direction. Consequently,  $\sigma_{zz}$  vanishes. The off-diagonal (face shear) components of the surface stress tensor also vanish for symmetry reasons when the coordinate system is chosen to coincide with the crystallographic axes. Additionally,  $\sigma_{xx}$  and  $\sigma_{yy}$  are equal for the frequently considered cases of (111) or (100) surface, since the surface stress is isotropic. In these cases, the surface stress tensor,  $\sigma_{ij}$ , takes on a simple form, and is usually characterized by a single number,  $\sigma$ : the surface stress. By convention, the surface stress is *positive* when it is *tensile*, while it is *negative* when it is *compressive*.



### 2.2.2 Measurement of Surface Stress

The bending plate method is typically used to measure surface stress. This method yields a measure of the relative surface stress difference between two sides of a thin plate. A measure of the plate's curvature is related to this relative surface stress. It is important to note that the bending plate method yields relative changes in surface stress acting on a surface. The plate's surface could be stressed or unstressed prior to a change in surface stress (resulting from molecular adsorption, for example). Since the absolute surface stress acting on a substrate's surface prior to a change in surface stress is usually not known, the bending plate method typically only yields a relative change in surface stress resulting from some process. The cantilever-based sensor used in this work to measure the surface associated with alkanethiol SAM formation on gold-coated cantilever is an example of a tool that uses the bending plate method, and is described in detail in *Chapter 3: Experimental Methods*.

Measurement of the absolute surface stress is much more complicated, but can be evaluated in some cases [44]. Absolute surface stress can also be measured using the bending plate method if the absolute surface stress is known for one surface of the plate. Electron diffraction studies [55,56] of nanoparticles have led to the measure of the absolute surface stress as it is related to the measured lattice expansion of the particle.

### 3 Experimental Methods

The instruments described herein have been used to gain some insight into the origins of the surface stress induced during alkanethiol SAMs formation, and to establish a versatile and reliable cantilever-based sensing platform. Characterization of this model self-assembled system will ultimately lead to an understanding and optimization of the response of cantilever-based sensors. In particular, these instruments were developed and/or used in order to address issues that limit the reliability, reproducibility, and accuracy of results obtained through cantilever-based sensing.

A differential cantilever-based chemical sensor was designed and built [57] to investigate the reproducibility, reliability, and sensitivity of such sensors. A separate system combining a cantilever-based sensor and an ellipsometer was also built to perform simultaneous, *in situ*, surface stress and monolayer thickness measurements. In addition, a scanning tunneling microscope (STM) was used *ex situ* to characterize the resulting self-assembled monolayers adsorbed onto the cantilever surface. Lastly, this chapter will discuss the methods used for sample preparation.

#### 3.1 Differential Cantilever-Based Sensor

A differential cantilever-based surface stress sensor was designed and built. Figure 3.1 is a photograph of the differential cantilever-based sensor setup. The system uses two commercially-available AFM micro-cantilevers, one used as the *active* sensor, and the second used as a *reference*. The active cantilever is

sensitized to react to specific target molecules. The reference cantilever is rendered inert to the presence of the target molecule under investigation, while remaining sensitive to other environmental factors that can also result in a deflection of the active cantilever, such as temperature variations (bimetallic effect), turbulent flow around the cantilever, vibrational (including acoustic) noise, non-specific binding, etc. The differential signal obtained by subtracting the reference signal from the active cantilever's response is solely due to the interaction of the target molecules with the active cantilever. This approach results in very sensitive surface stress measurements associated with specific molecular interactions on the active cantilever's surface.

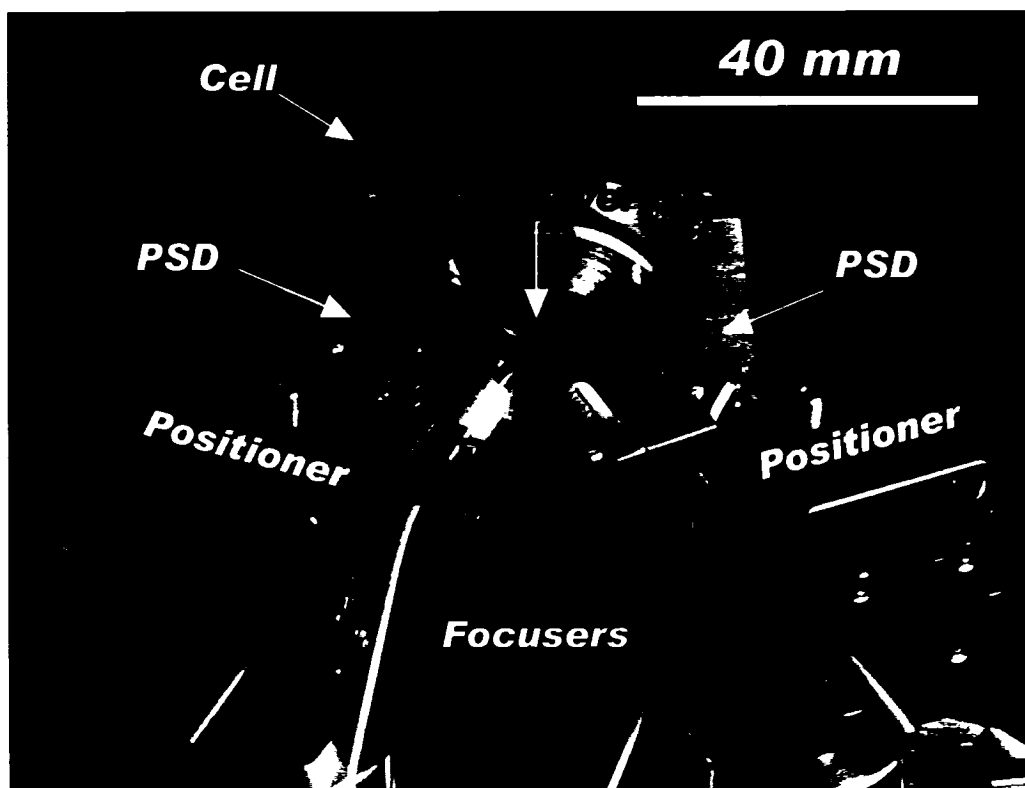


**Figure 3.1:** Photograph of the differential cantilever-based chemical sensor. Featured in the image are the laser focusers, the aluminum cell holding the active and reference cantilevers, the position-sensing (photo)detectors (PSDs), as well as the positioners used to focus the laser light onto the cantilever apex.

### 3.1.1 Cantilevers

The differential system uses two commercially-available cantilevers. Ideally, the active and reference cantilevers should be as close to each other as possible in order to ensure that both cantilevers are exposed to identical environmental conditions, essential in obtaining an effective differential signal. Although it is possible to micro-fabricate sets of cantilevers in close proximity (a few micrometers) on a single chip, the use of two cantilevers mounted on separate chips makes it much easier to functionalize the active and reference cantilevers independently without resorting to using micro-fluidic technologies [9]. Our system is designed to accommodate standard, commercially-available silicon or silicon nitride AFM micro-cantilevers.

The choice of cantilever to be used as a sensor must take into account the following requirements:

- The spring constant of the cantilever must be low in order to maximize its response during chemical sensing.
- The cantilever's material properties (density, Young modulus, Poisson's ratio, spring constant, etc.) must be well-defined (or measurable) to allow for an accurate quantitative conversion of the cantilever deflection into a measure of surface stress.
- The cantilever's geometry must be simple enough to facilitate the conversion of the cantilever deflection into a measure of surface stress (see Chapter 4).

A good choice would be a rectangular-shaped, single-crystal silicon cantilever. Despite being more rigid than commonly-used silicon-nitride cantilevers, silicon cantilevers can be micro-fabricated with sufficiently low spring constants [58] for special chemical sensing applications. Nevertheless, commercially-available triangular-shaped silicon-nitride cantilevers were used due to their lower spring

constant, low-cost and availability. Although slightly more difficult to calibrate (see *Chapter 4: Calibration*), these triangular silicon nitride cantilevers have a lower spring constant ( $k \approx 0.01\text{N/m}$ ) compared to most other commercially available single-crystal silicon ones, making them more sensitive. In addition, the triangular shape makes it easier to reproducibly align the laser used for deflection sensing (see *Section 3.1.2: Deflection Sensing*).

The cantilevers used in this study are mounted on a *chip*. Six different (geometries, spring constants) cantilevers are fabricated on a single chip. Furthermore, each chip is one of a few hundred that make up a *wafer*. Most experiments described in the present work featured the use of the V-shaped cantilevers purchased from Veeco [59].

Figure 3.2 depicts the cantilevers used in our studies. Cantilever ‘C’ has the lowest spring constant ( $\sim 0.01\text{ N/m}$ ), making it most sensitive as a chemical sensor. The typical dimensions and properties (as supplied by the manufacturer) of cantilevers labeled B, C, and E are summarized in Table 1. Actual dimensions were measured by field-emission scanning electron microscopy (FE-SEM) imaging. These dimensions were found to be uniform (within FE-SEM measurement errors) for similar cantilevers from different chips originating from the same wafer, as discussed in *Chapter 4: Calibration*. Dimensions were re-measured when new wafers were purchased.

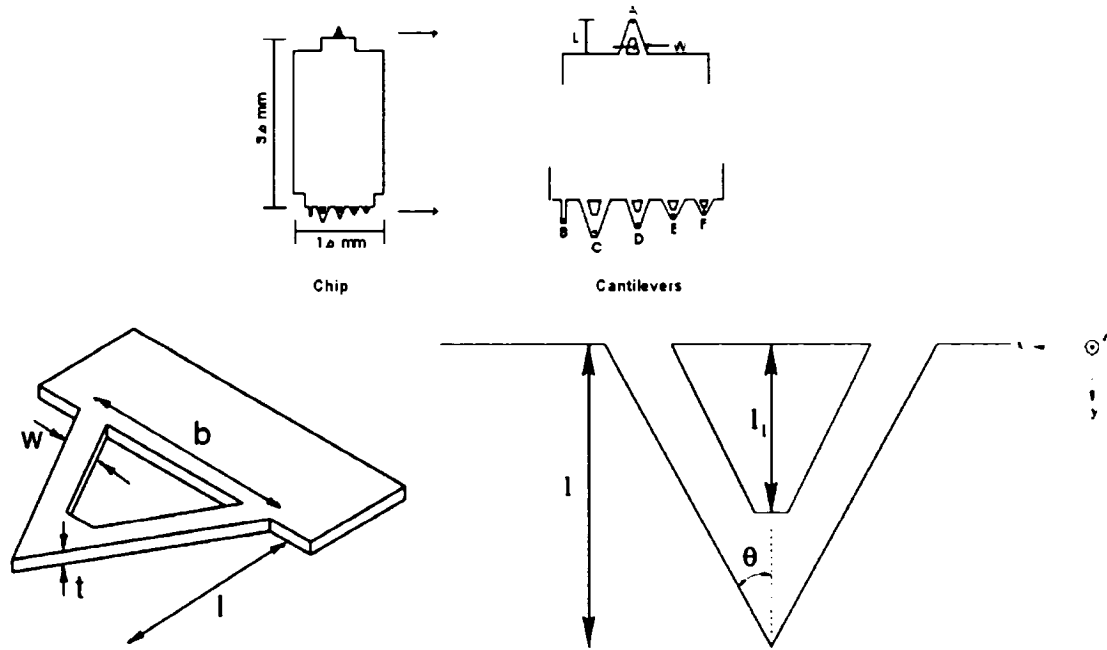


**Figure 3.2:** Multiple cantilevers are available on a single chip, each having different dimensions and spring constants. FE-SEM was used to assess these dimensions. These dimensions are required in order to convert the measured cantilever deflection into a surface stress, as discussed in Chapter 4.

<i>Variable Name</i>	<i>Variable</i>	<i>B</i>	<i>C</i>	<i>E</i>
Length	$l$	200 $\mu\text{m}$	320 $\mu\text{m}$	140 $\mu\text{m}$
Leg Width	$w$	20 $\mu\text{m}$	22 $\mu\text{m}$	18 $\mu\text{m}$
Thickness	$t$	0.6 $\mu\text{m}$	0.6 $\mu\text{m}$	0.6 $\mu\text{m}$
Base Width	$b$	-	221 $\mu\text{m}$	141 $\mu\text{m}$
Intermediate Length	$l_1$	-	230 $\mu\text{m}$	85 $\mu\text{m}$
Sharpness Angle	$\theta$	-	19.1°	26.8°
Spring Constant	$k$	0.02 N/m	0.01 N/m	0.1 N/m
Resonant Frequency	$f_{res}$	15 kHz	7 kHz	38 kHz

**Table 1:** Typical dimensions of the cantilevers used in this study.

Figure 3.3 shows a FE-SEM image of a set of cantilevers mounted on a single chip.

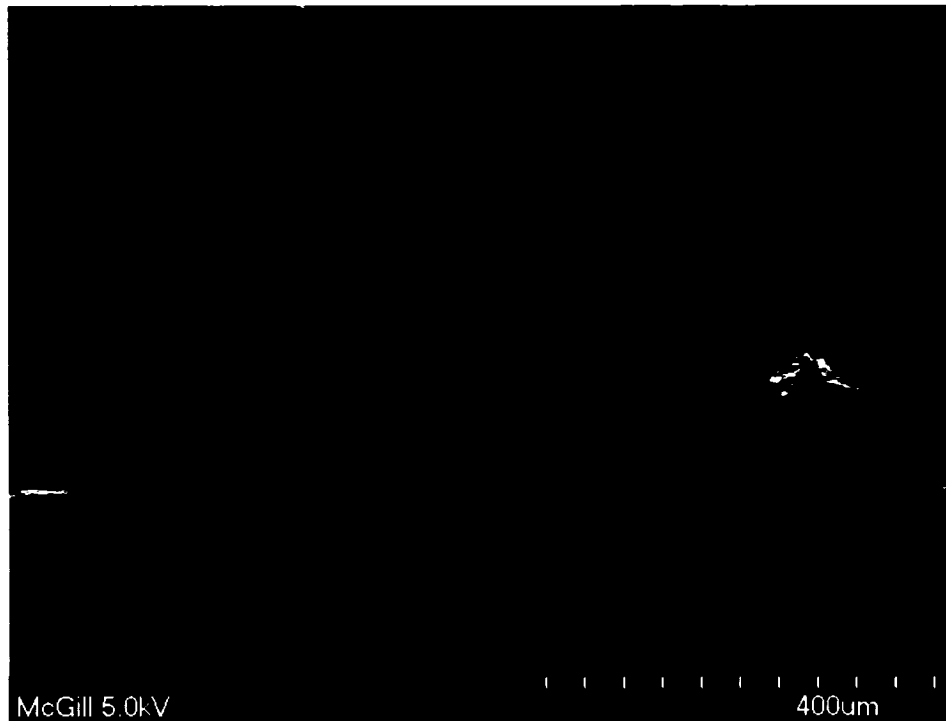


**Figure 3.3:** SEM image of commercially-available [59] silicon nitride micro-cantilevers. Five different cantilevers (one rectangular, four V-shaped) are visible here, all mounted on a single chip. Only part of the chip (approximately  $1.6 \times 3.6$  mm) is visible in this image (bottom). The adhesive tape used to mount the chip on the sample holder is visible in the background (looks like Swiss cheese).

### 3.1.2 Deflection Sensing

Several deflection sensing schemes exist to monitor the deflection of AFM cantilevers. The laser beam deflection technique was used in our system, but other techniques have been developed.

For example, some groups have used special piezoresistive or capacitive cantilevers [20,21] yielding an electrical signal that is proportional to the

deflection of the cantilever. Although these cantilevers require relatively simple electronics and no extra optical components, they were not used in the present study since their spring constants are typically larger than that of silicon or silicon nitride cantilevers, thus reducing their sensitivity [60]. In addition, these electronics-based cantilevers have the disadvantage of requiring that the deflection sensing electronics be isolated from the chemical environment surrounding the cantilevers. In the case of capacitive deflection sensing, use in electrolyte solutions is impossible due to the Faradic currents between the capacitor plates.

Another common deflection-sensing scheme uses fiber interferometry [61]. In this case, a cleaved fiber is brought in close proximity ( $\sim 10\text{ }\mu\text{m}$ ) to the cantilever surface. The laser light that emerges the cleaved fiber reflects off the cantilever surface and re-enters the fiber. This light interferes with the small fraction of light that never exited the fiber but was internally reflected off the cleaved surface of the fiber. This resulting interference is a function of the distance between the cleaved end of the fiber and the cantilever surface. This distance will change when the cantilever deflects. Monitoring the intensity of the interference signal yields a cantilever deflection measurement. Although fiber interferometry results in very sensitive cantilever deflection measurements, the fiber's fragility and the difficulty associated with cleaning the fragile fiber between each experiment make it unsuitable for use in a cantilever-based chemical sensor. Also, fiber interferometry runs into limitations when the cantilever suffers large deflections ( $> 3\text{ }\mu\text{m}$ ), thus reducing the dynamic range of the cantilever-based system. However, in this work, fiber interferometry was used to calibrate the cantilever deflection signal, as discussed in greater detail in *Section 4.1: Cantilever Deflection Measurement*. Figure 3.4 shows a fiber interferometer used to monitor cantilever deflections.



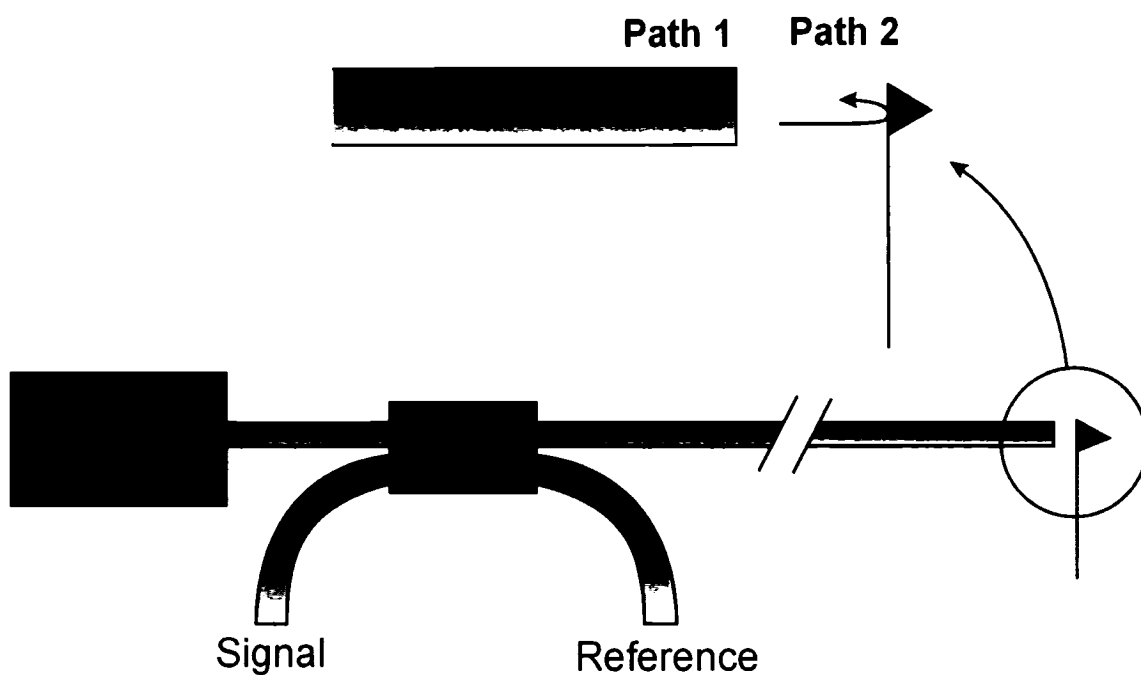


**Figure 3.4: Homemade fiber interferometer is used to monitor the deflection of the cantilever. This interferometer is used for calibration purposes, but not as the primary deflection-sensing method. Interference occurs between the light from paths 1 and 2 due to their relative path difference (twice the distance from the fiber end to the cantilever surface). The “reference” signal can be used to monitor the laser diode intensity.**

The optical beam deflection technique commonly-used in commercial AFMs is used in our cantilever-based chemical sensors [57], as shown is Figure 3.5. In addition to being very sensitive to cantilever deflections, one of the main advantages of using this method is that all the deflection-sensing components can be kept outside of the enclosed cell environment.

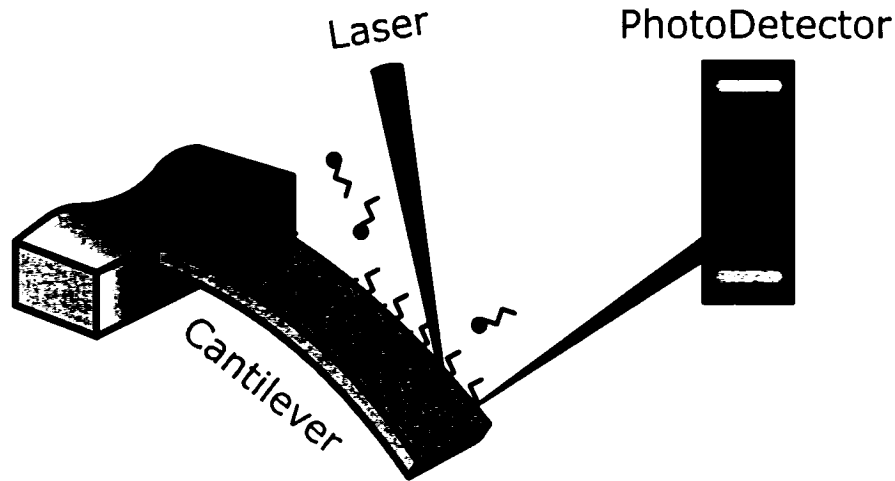


**Figure 3.5:** The optical beam deflection technique is used to monitor the deflection of the cantilever. A laser is focused onto the end of the cantilever. The displacement of the reflected laser beam is monitored using a position sensing (photo)detector (PSD).

The light from a laser diode [62] was coupled to a FC-connectorized single-mode optical fiber. The laser diode had a measured threshold driving current of 35.5 mA, and was typically operated at 41 mA. A wavelength of 635 nm was chosen to minimize the amount of power absorbed by the gold-coated cantilever [63], while remaining in the visible range to facilitate alignment. The light is then split into two fibers using a 50/50 coupler [64]. The two fibers emerging from the coupler were then fitted with GRIN (graded index) lenses [65] which focused the beam onto the cantilevers at a working distance of approximately 9 mm with a spot size of about 16  $\mu\text{m}$ . Approximate 650  $\mu\text{W}$  of power emerged from each focuser for a laser driving current of 41 mA. The use of a single common light source makes it possible to eliminate the effects of laser intensity noise on the differential measurement since both the active and the reference cantilevers experience the same noise. The two focused laser beams are aligned onto the apex of the two cantilevers using a 5-axis micro-positioner [66]. The displacement of the reflected laser beams are monitored using two independent position sensitive (photo)detector (PSD). This measured displacement signal (PSD signal) is effectively directly proportional to the deflection of the cantilever. Linear PSDs were chosen instead of four-quadrant photodetectors commonly-

used in AFMs. The main advantage of using PSDs is that there is no need to align the reflected laser beam with the center of the detector, since linearity is maintained over most of their active surface ( $> 90\%$ ). Although four-quadrant detectors typically have a larger bandwidth, PSDs are used since static (DC) deflections measurements were performed throughout this study as opposed to dynamic (AC) frequency measurements, and adequate sensitivity is achieved. Figure 3.6 shows a top view of the deflection sensing components. The cantilevers were angled away from each other by  $14^\circ$ . This angle is necessary due to geometrical constraints imposed by the focusers and the PSDs. In addition, this angle prevents stray laser light reflecting from the glass (sealing the cell) from hitting the PSDs, thus influencing the deflection measurement.

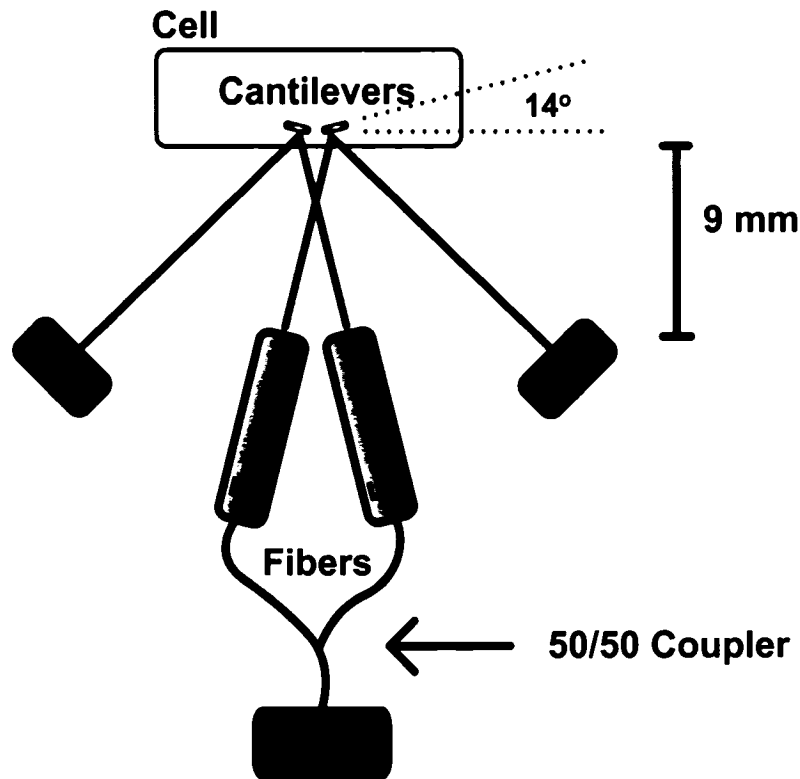


**Figure 3.6: Top view of the deflection sensing components. The cantilevers are angled away from each other by  $14^\circ$  in order to accommodate all the components.**

Light impinging on the PSD surface produces a photocurrent which is collected at two electrodes located 10 mm apart at either end of the photoresistive surface.

These two photocurrents are converted to a voltage and amplified ( $Y_1$  and  $Y_2$ ) using low-noise transimpedance amplifiers [67]. The gains of the amplifiers ( $1.0 \times 10^5$ ,  $2.2 \times 10^5$ ,  $4.7 \times 10^5$ , and  $1.0 \times 10^6$ ) are selectable by choosing feedback resistors with values of 100, 220, 470 and 1000 k $\Omega$ , respectively. Furthermore, the values of each pair of resistances were matched to ensure linearity.  $Y_1$  is additionally inverted using an amplifier [68] with a gain of -1. The amplified voltages,  $Y_1$  and  $Y_2$ , are then fed into an analog dividing chip [69] which converts the signals into a voltage,  $S$ , which is directly proportional to the position of the reflected spot (centroid of all light hitting the PSD) on the PSD surface:

$$S = \frac{Y_2 - Y_1}{Y_1 + Y_2} \quad \text{Equation 3.1}$$

The deflection of the cantilever can be inferred from the measurement of the displacement of the reflected laser spot on the PSD surface. The electronics used to process the PSD currents is depicted in Figure 3.7. The PSD signals are acquired using an analog-to-digital converter (ADC) [70], interfaced to a computer via acquisition software written in Visual C++.

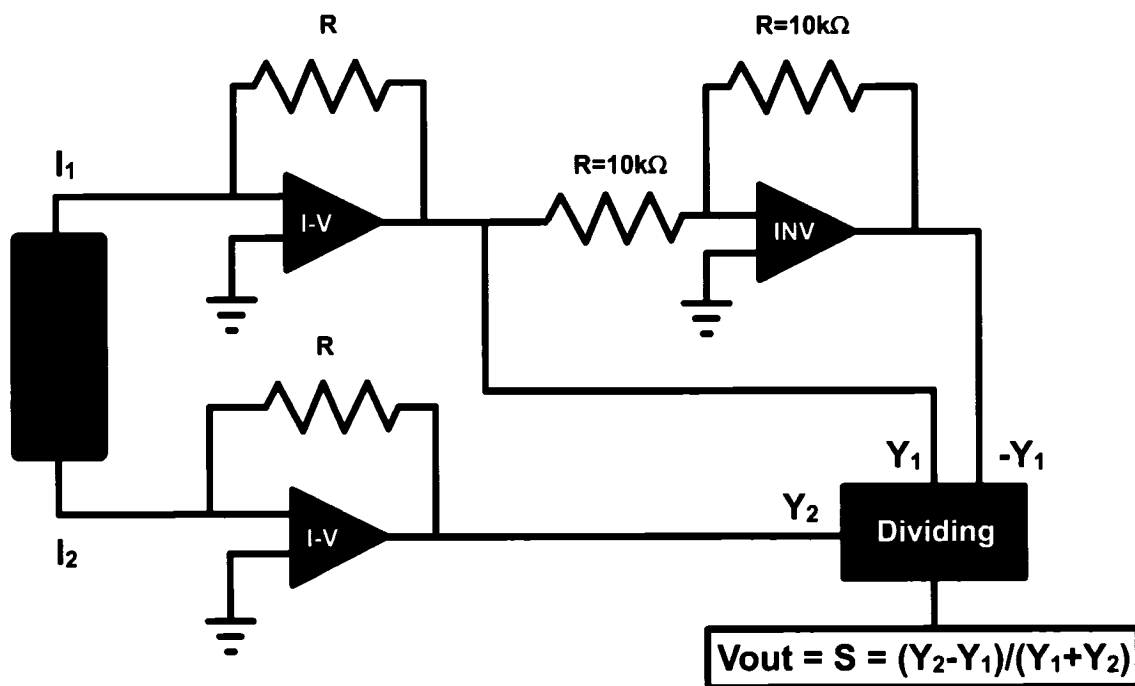


**Figure 3.7:** Electronics used to process the PSD photocurrents. The photocurrents are amplified using I-V converters with a gain defined by  $R$  (selectable at 100, 220, 470, and 1000 k $\Omega$ ).  $Y_1$  is inverted. A dividing chip outputs the desired PSD signal,  $S$ , which is directly proportional to the position of the reflected spot on the PSD.

### 3.1.3 Cell

There are several requirements that constrain the sensor's cell's design. The main requirements are that the active and reference cantilevers must be as close to each other as possible, the cell material must not interfere with the sensing experiment and must easily be washed between experiments to prevent contamination, and the back of the cantilevers must be accessible for calibration, as discussed in the next chapter. Cells were machined out of aluminum, PEEK [71], and Kel-F [72]. However, aluminum cells were used for the alkanethiol experiments for their ease of cleaning. Cleaning the aluminum cell between subsequent experiments involved soaking it in a boiling ethanol/chloroform (50/50) solution [73] for 5 min followed by 30 min of ultrasonication in the same solution. Additionally, this procedure is repeated once. The front of the cell was sealed with a glass slide

pressed against a Teflon O-ring. This glass allowed the deflection sensing laser beam to enter the cell towards the cantilevers. A separation distance of  $\sim 2$  mm between the two cantilevers was constrained by the physical width of the cantilever chips, which are clamped side-by-side inside the cell.

### 3.1.4 Analyte Introduction

The analyte can either be flowed into the cell or injected into a sealed, closed-cell. When using the flow method, the analyte is flowed into the cell through an inlet hole and exit via an outlet hole. This method allows for the introduction of different analytes introduced in sequence, and makes it possible to “flush” the cell, removing a particular analyte from the cell environment. On the other hand, the flow method often introduces noise (turbulent flow, variations in temperature, etc.) that can influence the deflection of the cantilever, making a differential measurement necessary in most cases. In the closed-cell configuration, the cell is sealed, and analytes are injected using a glass syringe through a Teflon-lined septum from the back of the cell. The surface stress measurements associated with the formation of alkanethiol SAMs were performed using the closed-cell method by injecting a pure liquid alkanethiol droplet at a specific location inside the cell. The droplet was then left to evaporate under ambient pressure at a fixed cell temperature. Approximately 5-150  $\mu\text{l}$  of liquid alkanethiol was typically injected. For these experiments, it was found that the volume of injected alkanethiols did not affect the surface stress measurement, as long as enough was injected such that some liquid was left when the alkanethiol vapor concentration reached saturation.

### 3.1.5 Cell Volume and Alkanethiol Vapor Diffusion

The separation distance,  $d$ , between the analyte droplet and the cantilevers is adjustable using a set of cylindrical extensions. Figure 3.8 shows a side-view of the cell used alone and with an extension.

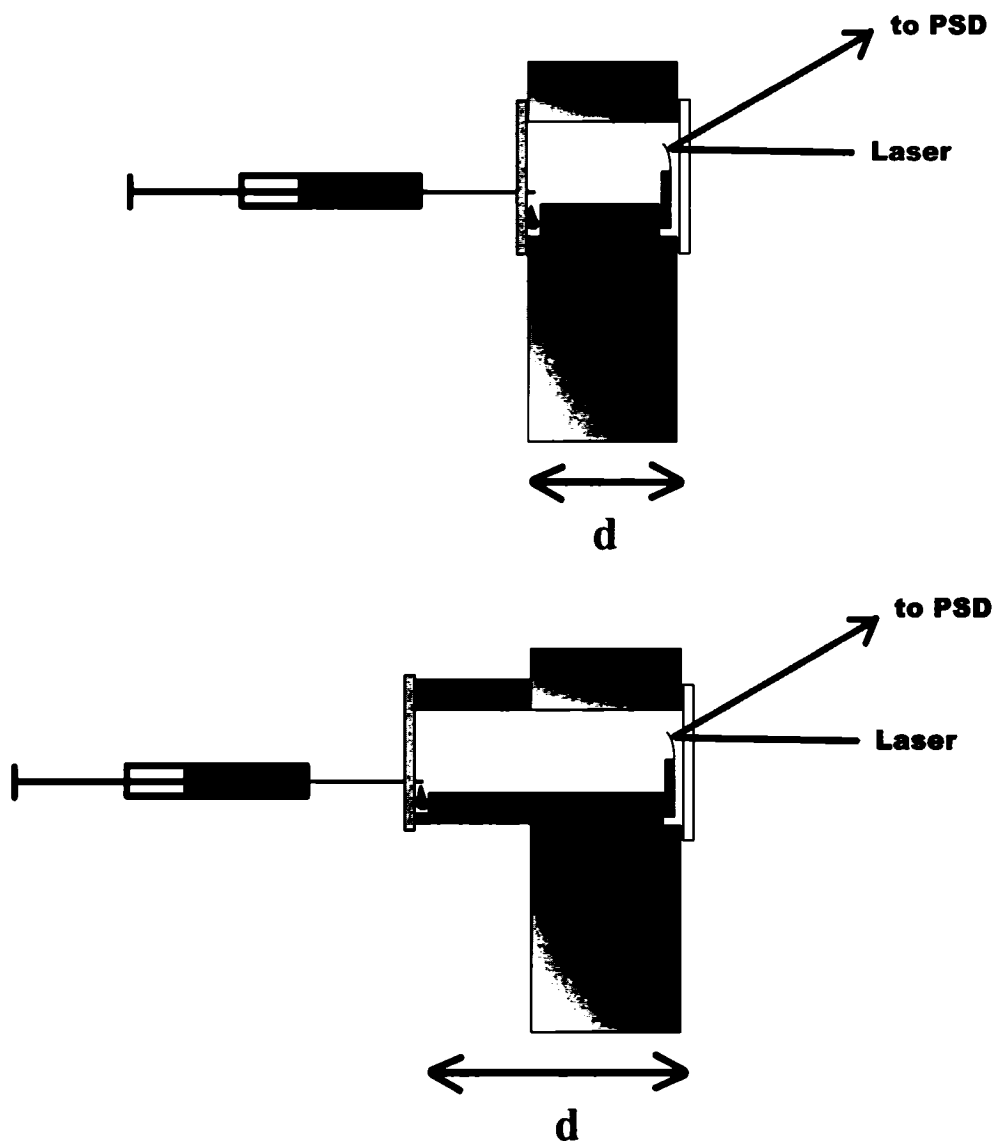


**Figure 3.8:** The separation distance,  $d$ , between the injected analyte droplet and the cantilevers is adjustable using a series of cylindrical extensions attached to the back of the cell (left). The liquid analyte is injected through a Teflon-lined septum at the back of the cell. The deflection sensing components are located at the front of the cell (right).

Increasing the alkanethiol droplet-to-cantilever distance effectively increases the time needed for the alkanethiol vapor concentration to achieve saturation at the location of the cantilevers in a closed-cell. The time constants associated with the increase in concentration of the alkanethiol vapor for various distances can be estimated by solving a 1-D diffusion equation of the form [74]:

$$\frac{\partial(n(x,t))}{\partial t} = D \left[ \frac{\partial^2 n(x,t)}{\partial x^2} \right] \quad \text{Equation 3.2}$$

where  $n(x,t)$  is the vapor concentration at position  $x$  and time  $t$ , and  $D$  is the diffusion constant associated with the analyte of interest (alkanethiol) [74]:

$$D \approx \frac{1}{3} \bar{v} \mu \quad \text{Equation 3.3}$$

where  $\bar{v}$  is the mean velocity of the gaseous analyte, and  $\mu$  is this molecule's mean free path. The mean velocity can be estimated by equating a molecule's kinetic energy to its thermal energy (using the equipartition theorem):

$$\frac{3}{2} kT = \frac{1}{2} m (\bar{v})^2 \quad \text{Equation 3.4}$$

where Boltzmann's constant  $k = 1.3807 \times 10^{-23}$  J/K [75]. For a decanethiol molecule, the mass  $m = 174.33$  u =  $2.8937 \times 10^{-25}$  kg, and the mean velocity  $\bar{v} \approx 205$  m/s at 293 K. Given the average mass of air of 0.02894 kg/mol (78.08% N<sub>2</sub>, 20.95% O<sub>2</sub> and 0.93% Ar [76]), the density of air of 1.293 kg/m<sup>3</sup>, and the fact that a mole of air occupies about 22.4 l (0.0224 m<sup>3</sup>), the mean free path in air can be calculated to be approximately  $3.34 \times 10^{-9}$  m. The diffusion constant can now be evaluated using Equation 3.3 to be  $D \approx 6.847 \times 10^{-7}$  m<sup>2</sup>/s.



In order to estimate the time constants for the increase in alkanethiol vapor concentration in the vicinity of the cantilever as the alkanethiol droplet evaporates in the closed cell, we use a simplified model where Equation 3.2 is solved for the case of diffusion into a semi-infinite region with constant concentration at the boundary, as schematically drawn in Figure 3.9.

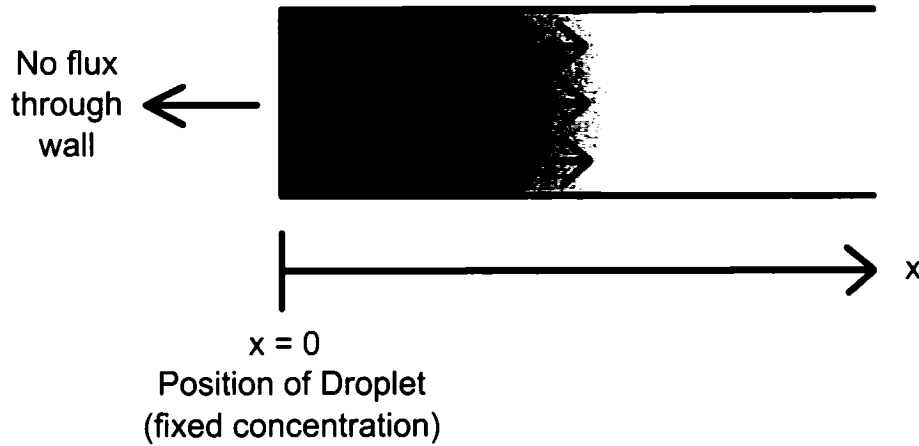


**Figure 3.9:** Evaporation and 1-D diffusion of an alkanethiol droplet positioned at  $x = 0$  in a semi-infinite plane, with a fixed concentration (reservoir) at the position of the droplet.

The solution to Equation 3.2 for this case is:

$$n(x, t) = n(0, 0) \operatorname{erfc} \left( \frac{x}{\sqrt{4Dt}} \right) \quad \text{Equation 3.5}$$

where *erfc* is the complementary error function [77] ( $\operatorname{erfc}(-\infty) = 2$ ,  $\operatorname{erfc}(0) = 1$  and  $\operatorname{erfc}(\infty) = 0$ ). Figure 3.10A is a plot of Equation 3.5 for decanethiol droplet-to-cantilever distances of 3, 30, and 100 mm. Figure 3.10B shows a graph of the time required to reach 50% saturation concentration as a function of the droplet-to-cantilever distance, again from Equation 3.5. The time constant associated with the increase up to saturation of the analyte (decanethiol) vapor concentration at the cantilever is proportional to the square of the droplet-to-cantilever distance.

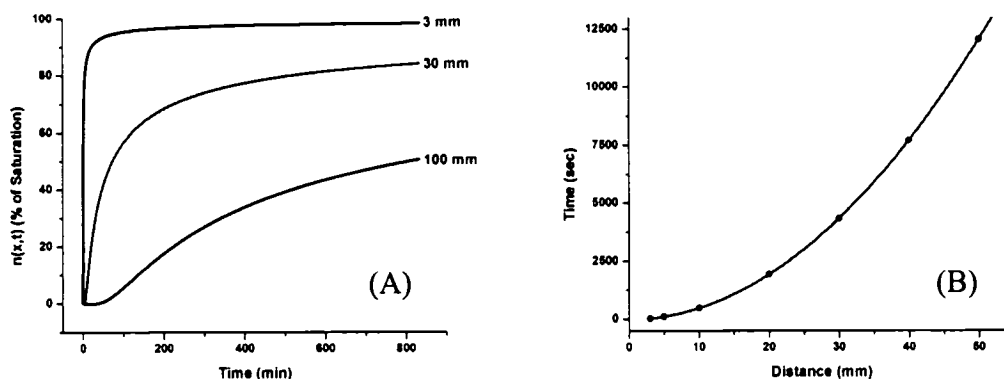


**Figure 3.10:** Graph of the theoretical percent concentration as a function of time (A) for decanethiol droplet-to-cantilever distances of 3, 30, and 100 mm. On the right is a graph (B) of the time required to reach 50 % of the saturation concentration as a function of the droplet-to-cantilever distance. The data points were calculated from Equation 3.5, while the red curve is a fit showing that this time is a function of the square of the distance.

As an example, it takes 43 seconds to reach 50% of the saturation concentration for a decanethiol droplet-to-cantilever distance of 3 mm, while it takes 4300 seconds to reach the same concentration for a distance of 30 mm. Although this model does not consider the 3-D case, or the closed-nature of the cell, it gives a good appreciation for the diffusion time constants for various droplet-to-cantilever distances. For decanethiol, given a quoted vapor pressure of 3 Pa at 298K, the saturation vapor concentration (100%) in air is about 30 ppm or 0.003%. [78,79] Taking into account the fact that the cell is closed, and moving from the 1-D to the 3-D diffusion equation, decreases these time constants, but the trend is similar.

### 3.1.6 Alkanethiol Purity

Pure liquid alkanethiol were purchased [80] and used as-is without further purification. The purity was assessed by gas chromatography (GC) using a flame ionization detector (FID) in methylene chloride as a solvent. Impurities typically found in alkanethiol are other alkanethiols of similar but different lengths. Disulfides are also commonly found, as they result from spontaneous binding of

two alkanethiol molecules at the thiol headgroup (two alkanethiol molecules joined together through an S-S bond). While GC will detect other alkanethiol impurities, it is insensitive to the presence of disulfides, as they are split back into two alkanethiol molecule upon heating. Nevertheless, the relatively high purities of the alkanethiols used in this study, as assessed by GC, gives confidence that further purification (by distillation or HPLC) was not necessary. These results are summarized in Table 2.

<i>Alkanethiol</i>	<i>Purity (%)</i>
C6	100.0
C8	100.0
C10	97.8
C12	99.7

**Table 2: Purity of alkanethiols used, assessed by gas chromatography using a flame ionization detector. The purities of C6 and C8 are quoted as 100.0 as no other impurity peaks were detected within the resolution limit (0.5 %) of the instrument. All quoted purities have an uncertainty of  $\pm 0.5$  %.**

Great care was taken to keep the alkanethiols used in this study free from contamination. Pure liquid alkanethiol were handled with glass pipettes previously cleaned with a method similar to the one used to clean the Al cell (see *Section 3.1.3: Cell*). Moreover, exposure to air and light was kept to a minimum during manipulation and storing, while samples were taken with a syringe through a Teflon-lined septum. Nevertheless, aging of the alkanethiols was observed in some experiments despite not measuring any contamination by GC. New batches of alkanethiols were purchased at approximately 6 month intervals to avoid such effects.

### 3.1.7 Reference Cantilever Preparation

An effective reference cantilever must be rendered inert to the chemical signal of interest, while remaining sensitive to all the other environmental factors that can induce a cantilever deflection. Consequently, the preparation of the reference cantilever has to be adapted depending on the target molecule of interest. In the experiments described in this work, the target molecules are alkanethiols, and the active sensor is a gold-coated cantilever. In this case, the reference cantilever is also gold-coated with the same amount of gold as the active cantilever, but an alkanethiol SAM was pre-formed on its surface. This SAM-covered gold-coated cantilever is thus rendered inert to further adsorption of alkanethiol molecules while remaining sensitive to temperature variations, environmental noise, etc. This protective SAM was formed by incubating a gold-coated cantilever in a 1 mMol dodecanethiol/ethanol solution for 12 hours. The reference cantilever is then removed from the dodecanethiol solution and rinsed in anhydrous ethanol. This method of preparing alkanethiol SAMs is widely used and described in the literature [81,82].

The effectiveness of this reference cantilever was tested by exposing it to dodecanethiol vapor and monitoring its deflection. Figure 3.11 shows that the reference cantilever does not deflect as the result of dodecanethiol vapor exposure, as compared to the deflection of an active gold-coated cantilever. Both the active and the reference cantilevers show a slight upwards trend at the end of the experiment, perhaps due to a slow increase in temperature or to the physisorption of alkanethiol molecules on top of the SAM. The use of a dodecanethiol SAM as a passivating layer formed on the reference cantilever surface is effective as long as the target alkanethiol molecule is not longer than the reference SAM alkanethiol, since replacement of short alkanethiol molecules forming a SAM by longer ones has been shown to occur [83].

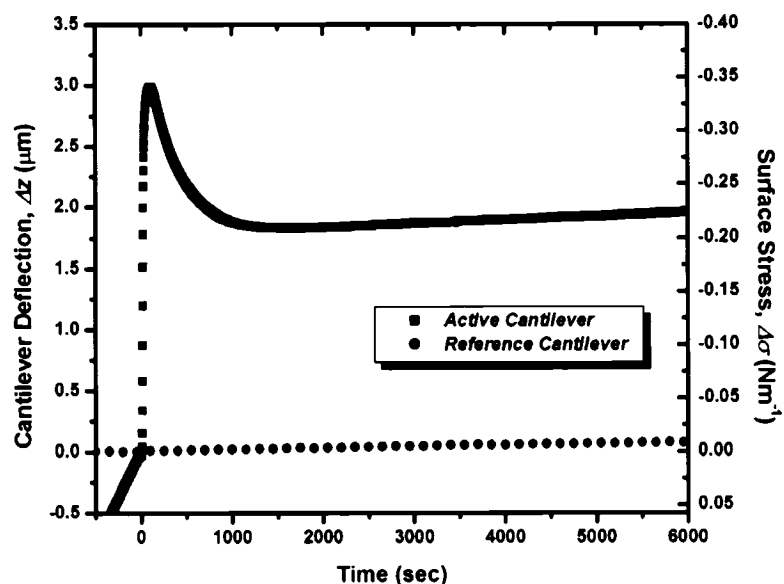


Figure 3.11: The SAM-covered reference cantilever does not deflect upon exposure to dodecanethiol vapor at  $t = 0$  sec, whereas the active gold-coated cantilever deflects due to the induced surface stress brought upon by dodecanethiol adsorption on its surface.

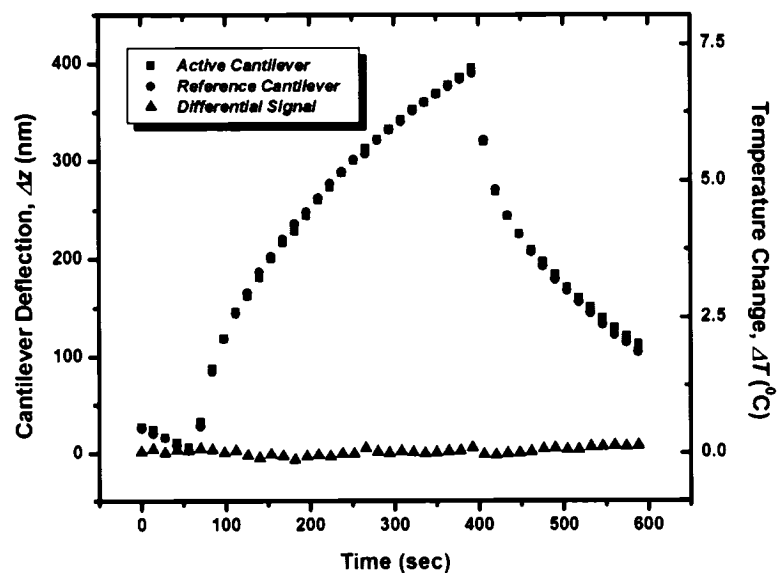
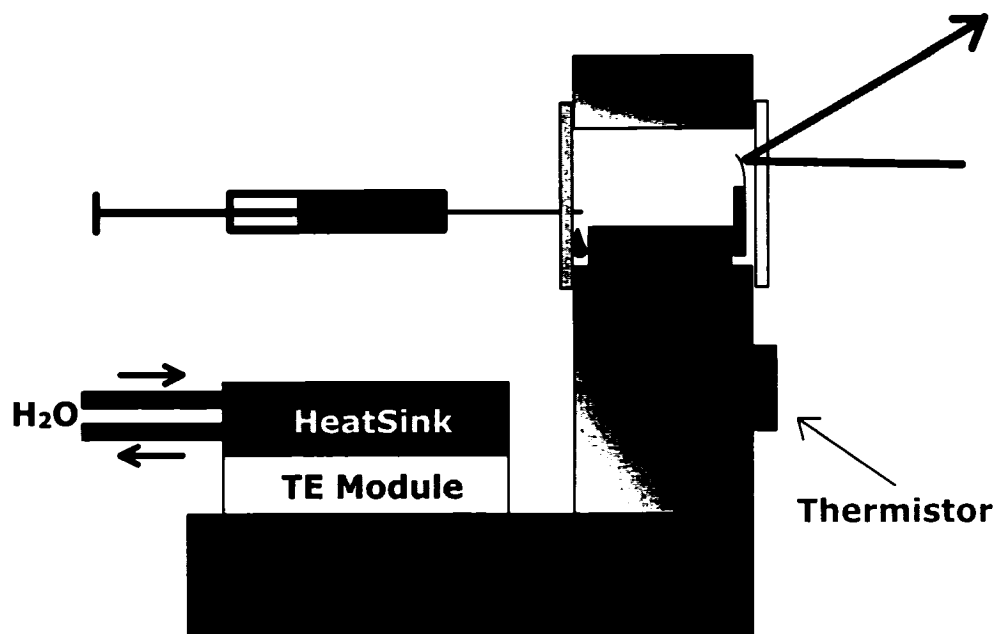


Figure 3.12: Both the active (red squares) and the reference (green circles) cantilevers similarly deflect in response to variations in temperature. The differential signal (active signal – reference signal) remains insensitive to these variations in temperature.

Figure 3.12 shows the response of both an active and a reference cantilever due to variations in temperature. Both cantilevers deflect due to the bimetallic effect. Subtracting the reference signal from the active signal yields a differential signal that is independent of temperature.

### **3.1.8 Temperature Control**

Thermoelectric modules [84] are used to control the cell temperature. An analog temperature controller [85] controls the output of a 12 V switching power supply using pulse width modulation (PWM) for effective PID (proportional-integral-derivative) control. The cell temperature is monitored using a calibrated thermistor [86]. Figure 3.13 depicts a side view of the thermoelectric module mounted on the aluminum base (cell holder). The cell holder is thermally isolated from the rest of the system. Good thermal contact is achieved by using thermally conductive silicone between the module and the cell holder, and between the holder and the cell. A water cooled copper heatsink (coolsink) is used on the backside of the module to provide proper energy dissipation. Water cooling (heating) is necessary to achieve proper temperature control. The thermoelectric modules draw 9 A at 12 V.



**Figure 3.13: Side view of the temperature control system. A thermoelectric (TE) module controls the temperature of the cell by being in good thermal contact with an aluminum base. A water-cooled copper heatsink dissipates the heat (cold) generated on the opposite side of the TE module. A thermistor monitors the cell's temperature. These components are thermally isolated from the rest of the system.**

The temperature resolution of the temperature controller is limited to 0.01 °C. Most stable control was achieved using PI feedback. Using a proportional band of 15 °C and an integral time constant at 0.33 repeats/minute produced stable control with temperature feedback oscillations of approximately 0.02 °C. The gold-coated cantilevers deflect by a few nanometers as a result of these temperature fluctuations due to the bimetallic effect. Nevertheless, these oscillations were much smaller than typical deflection measurements associated with the formation of alkanethiol SAMs. Therefore, it was possible to use temperature control without affecting these surface stress measurements.

## 3.2 Combined Ellipsometry and Cantilever-Based Sensing

There is still a great deal of debate in the literature over the mechanisms driving the self-assembly of alkanethiol SAMs [87]. Different experimental techniques used to analyze the formation of SAMs often highlight different aspects of the formation process, as discussed in more detail in *Chapter 5: Alkanethiol Self-Assembled Monolayers*. Contradicting arguments are sometimes found in the literature since researchers often limit themselves to too few techniques when studying SAM formation. The use of complementary experimental techniques is therefore quite important in understanding the mechanisms driving self-assembly.

A combined micromechanical cantilever-based sensor and ellipsometer was designed and built in order to gain complementary information about the formation process of alkanethiol SAMs. A cantilever-based sensor similar to the differential sensor described above was combined with a commercial ellipsometer. This system thus provides simultaneous *in situ* surface stress and thickness measurements associated with molecular adsorption. The combined system was used to investigate the growth kinetics of dodecanethiol SAMs on gold from the vapor phase in real-time.

### 3.2.1 Setup

A custom-made cantilever-based sensor was integrated with a commercial ellipsometer [88]. The sensor part of the combined system was designed to fit onto the ellipsometer's sample stage. A photograph of the system is shown in Figure 3.14.





**Figure 3.14: Photograph of the combined cantilever-based sensor and ellipsometer. The sensor was designed to fit on the stage of a commercial ellipsometer.**

The cell was machined out of aluminum and is designed to accommodate both the sensor's optical beam deflection sensing laser and the ellipsometer's laser. Because of geometrical constraints, the deflection sensor's laser enters and exits the cell defining a plane that is perpendicular to the ellipsometer laser's plane. This is shown in the schematic of Figure 3.15, which illustrates a side-cut view of the cell. The laser beam used for the sensor's deflection sensing enters the cell through a glass slide at the top of the cell. The ellipsometer laser enters and exits through angled quartz windows. Quartz was chosen because of its optical homogeneity. These two quartz windows are angled at  $70^\circ$  with respect to the sample surface in order to ensure that the ellipsometer laser beam passes through the quartz with a normal angle of incidence [89]. This minimizes some systematic errors that arise from undesired changes in polarization. All windows are sealed using brown Viton O-rings. The ellipsometer uses a HeNe laser operating at 632.6 nm.

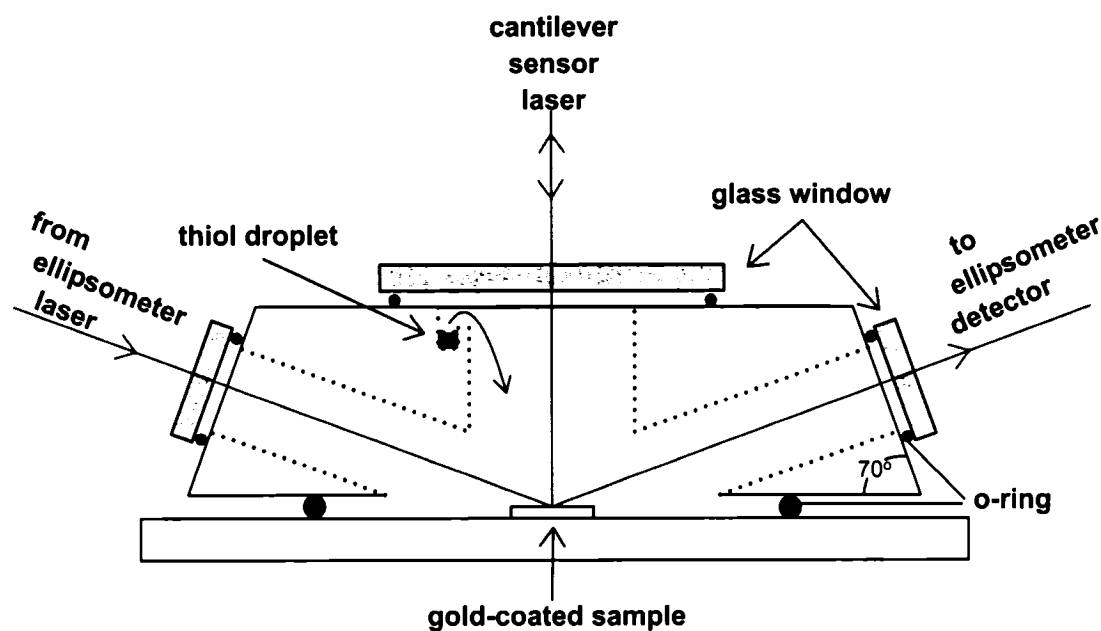


**Figure 3.15:** Side-view of the cell used in the combined cantilever-based sensor and ellipsometer setup. The cantilever deflection is monitored using a laser beam entering the cell from the top in a plane perpendicular to the plane defined by the ellipsometer laser path. The distance between the analyte (alkanethiol) droplet and the samples is approximately 15 mm.

The cell is designed for both closed-volume and flow experiments. For closed-volume experiments, chemicals are introduced into the cell by injection through a Teflon-lined septum. In flow experiments, liquid or vapor analytes are flowed into the cell via an inlet hole and exits through an outlet hole. The inlet and outlet are tapped in order to accommodate PEEK tubing fittings designed to hermetically attach PTFE tubing to the cell. The alkanethiol SAM formation experiments were performed in the closed-cell configuration. Here, a small amount of liquid alkanethiol is injected into the cell and left to evaporate into the vapor phase before reaching the gold samples.

Unlike the differential cantilever-based sensor described above, this combined system utilizes a single cantilever as a sensor. For this reason, care must be taken to minimize the environmental effects that caused unwanted deflections of the

cantilever. Therefore, the entire system was covered in a light-tight box equipped with fans to help maintain the air temperature surrounding the setup constant. It was possible to run closed-volume experiments since the surface stress due to the adsorption of the alkanethiol molecules of interest overwhelmed any cantilever deflections resulting from variations in temperature and/or mechanical or acoustic noise. However, these undesired deflections made experiments performed under flow conditions impossible to recover without the use of a second cantilever used as a reference; turbulence and variations in temperature resulting from the flowing analyte induce parasitic cantilever deflections.

The deflection of the cantilever in the combined system was monitored using the optical beam technique. A laser diode operating at a wavelength of 635 nm was coupled to a singlemode fiber terminated with a FC-type connector. A FC connectorized focusing lens was used to focus the beam with a measured spot size of approximately 20 microns at a working distance of approximately 5 cm. A PSD was used to monitor the displacement of the reflected beam in a manner similar to the ones used in the differential system.

The size of the sample surface used for ellipsometric measurements is limited by the ellipsometer laser's spot size of approximately 1 mm in diameter. Consequently, it was impossible to perform thickness measurements of the SAM formed on the micro-cantilever itself. Ellipsometric measurements were performed either on the cantilever chip, which has a size of approximately  $1.6 \times 3.6$  mm, or on a separate gold-coated substrate. If two separate samples are used, the distance separating the two was minimized, and was typically less than 1 mm. This helps to ensure identical adsorption conditions. Gold-coated Si, SiN<sub>x</sub> and Mica were used for the ellipsometric measurements.

Ellipsometry yields thickness information by monitoring changes in polarization of laser light as it is reflected off a surface (gold) covered with a thin film (SAM). Changes in the phase angle between parallel and perpendicular components of the

incident light upon reflection are monitored, and yield a measure of film thickness [89]. Given a known index of refraction of the thin film, its thickness can be calculated from the measured change in polarization. The index of refraction of a dodecanethiol SAM ( $n = 1.459$ ) was assumed to be constant during formation, and was taken to be the same as that of bulk dodecanethiol [76].

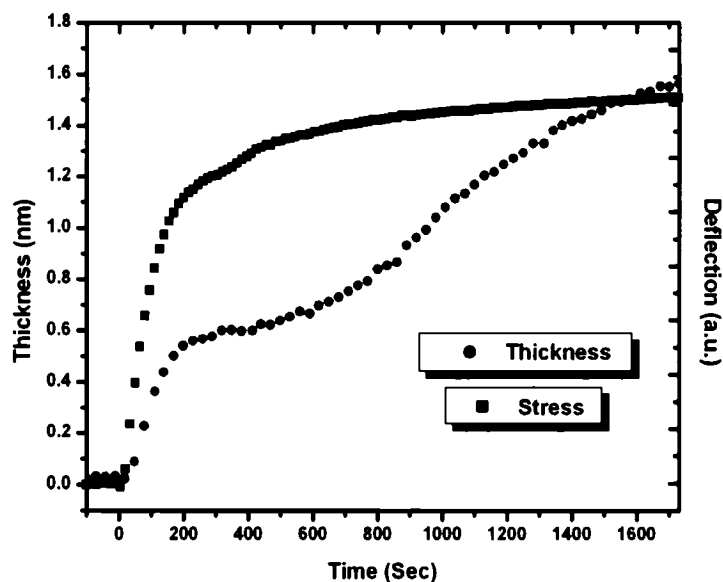


**Figure 3.16:** Evolution of the surface stress and the thickness of a dodecanethiol SAM on gold as it is being formed. Dodecanethiol was introduced at time  $t = 0$  sec. Evidence of at least two processes with different time constants is apparent in both profiles.

The combined cantilever-based sensor and ellipsometer system yields simultaneous *in situ* surface stress and thickness measurements associated with SAM formation. The complementary use of ellipsometry makes it possible to associate surface stress with different structural phases that occur during alkanethiol SAM formation. Figure 3.16 shows an example graph of the time evolution of the surface stress and thickness as a dodecanethiol SAM is formed on gold. Both the surface stress and thickness profiles show evidence of at least two processes having different time constants. This combined system yields

complementary information about the formation process that is necessary in order to correlate the surface stress with different conformations of the SAM. The phase transitions associated with alkanethiol SAM formation will be discussed further in *Chapter 5: Alkanethiol Self-Assembled Monolayers*.

### 3.3 Scanning Tunneling Microscopy

Scanning tunneling microscopy (STM) was performed *ex situ* to characterize the alkanethiol SAMs formed under various adsorption conditions. Molecular resolution imaging was achieved in ambient air using a commercial stand-alone STM head [90] in constant-current mode. Due to difficulties in imaging SAMs formed on the cantilevers themselves, imaging was performed on the chip region about 100  $\mu\text{m}$  from the edge where the cantilever is mounted. Imaging by FE-SEM confirmed that the gold surface morphology was similar on this region and on the cantilever itself. This made it reasonable to assume that the monolayers imaged on the chip would be similar to the ones formed on the nearby gold-coated cantilever. In addition, SAMs formed on gold-coated mica substrates were also imaged.

STM tips were made by cutting  $\text{Pt}_{80}\text{Ir}_{20}$  wire [91] of 0.25 mm diameter by hand using stainless-steel cutters. Sufficiently sharp tips were formed by cutting the wire at a sharp angle while gently pulling in the direction of the tip. This tip fabrication technique resulted in an approximately 40% yield.  $\text{Pt}_{80}\text{Ir}_{20}$  was chosen for imaging in air since this alloy does not oxidize as much as other materials typically used as STM tips. Moreover, Pt makes the alloy malleable making it easy to cut by hand.

In order to successfully image alkanethiol SAMs with molecular resolution, it is important not to perturb or destroy the SAM with the tip. This is achieved by keeping the tip-sample distance (tunneling impedance) as large as possible, by

using a high tip-sample bias voltage and/or a low current setpoint. Imaging was most successful when using a tip-sample bias of 600 mV and a current setpoint of 25 pA, corresponding to a large tunneling impedance of 24 G $\Omega$ .

Calibration of the x-y STM piezo-scanner was performed by imaging highly-oriented pyrolytic graphite (HOPG) with atomic resolution. Given the known atomic surface lattice spacing of HOPG of 0.246 nm [92], we were able to calibrate the STM's piezoelectric sample scanner in the x-y direction. Height (z) was not precisely calibrated, although single atomic Au steps were imaged with an expected height of 0.24 nm [93].

### **3.4 Sample Preparation**

The formation of alkanethiol SAMs on gold from the vapor phase was the main focus of the present study. In this case, the analytes (target molecules) are alkanethiol molecules, and the receptive (sensitized) surface is gold. All gold surfaces were prepared by thermal evaporation.

Two main types of gold surfaces were prepared: surfaces with a relatively small average grain size, and surfaces with a large average grain size. Small-grained gold surfaces were prepared by thermally evaporating 10 nm of titanium [94] at a rate of 0.04 nm/sec followed by 100 nm of gold [95] at a rate of 0.14 nm/sec. In this case, the substrates were not pre-heated prior to the start of the evaporation, but radiative heating from the evaporation boats increased the sample temperature to  $130 \pm 20$  °C. The gold surfaces exhibiting a larger average grain size were prepared by initially heating the substrates to  $200 \pm 1$  °C for 30 minutes. A 100 nm gold film was then deposited at a rate of 0.14 nm/sec. The homemade heater was turned off during the evaporation, but the substrate temperature increased to  $260 \pm 10$  °C by the end of the evaporation. All evaporations were conducted with a base pressure better than  $1.0 \times 10^{-5}$  Torr ( $1.3 \times 10^{-3}$  Pa). Although Ti was

originally used as an adhesion layer between  $\text{SiN}_x$  and Au, it was found that adequate adhesion was possible without it. Sample temperatures for all evaporations were kept under 300 °C to prevent excessive permanent bending of the cantilevers. All alkanethiol experiments were performed using freshly evaporated gold in order to minimize the effects of gold surface contamination on the self-assembly process.

Figure 3.17 shows STM images of the small-grained and large-grained gold surfaces. Figure 3.17A shows gold with small grains, whereas the image in Figure 3.17B is of gold having larger grains, as described above. Grain sizes of  $90 \pm 50$  nm and  $600 \pm 400$  nm were measured for the small- and large-grained gold surfaces, respectively. The RMS roughness of the gold in Figure 3.17A and Figure 3.17B was measured to be  $0.9 \pm 0.2$  nm and  $0.3 \pm 0.1$  nm, respectively, on a 200 nm length scale. X-ray diffraction additionally revealed that both types of gold were Au(111). Gold surfaces with intermediate grain sizes were also prepared using a procedure similar to the one used to produce large-grained gold, except that the substrates were pre-heated to temperatures lower than 200°C. Unfortunately, producing larger grains by increasing the cantilever temperature during or after evaporation (annealing) to more than 350 °C resulted in a permanent bend in the cantilevers (due to the inherent tensile surface stress of the gold film) that made them unusable in the sensor setup. Additionally, annealing of the gold-coated  $\text{SiN}_x$  cantilever to such high temperatures produced gold surfaces of low quality because of large “cracks” formed in the film.

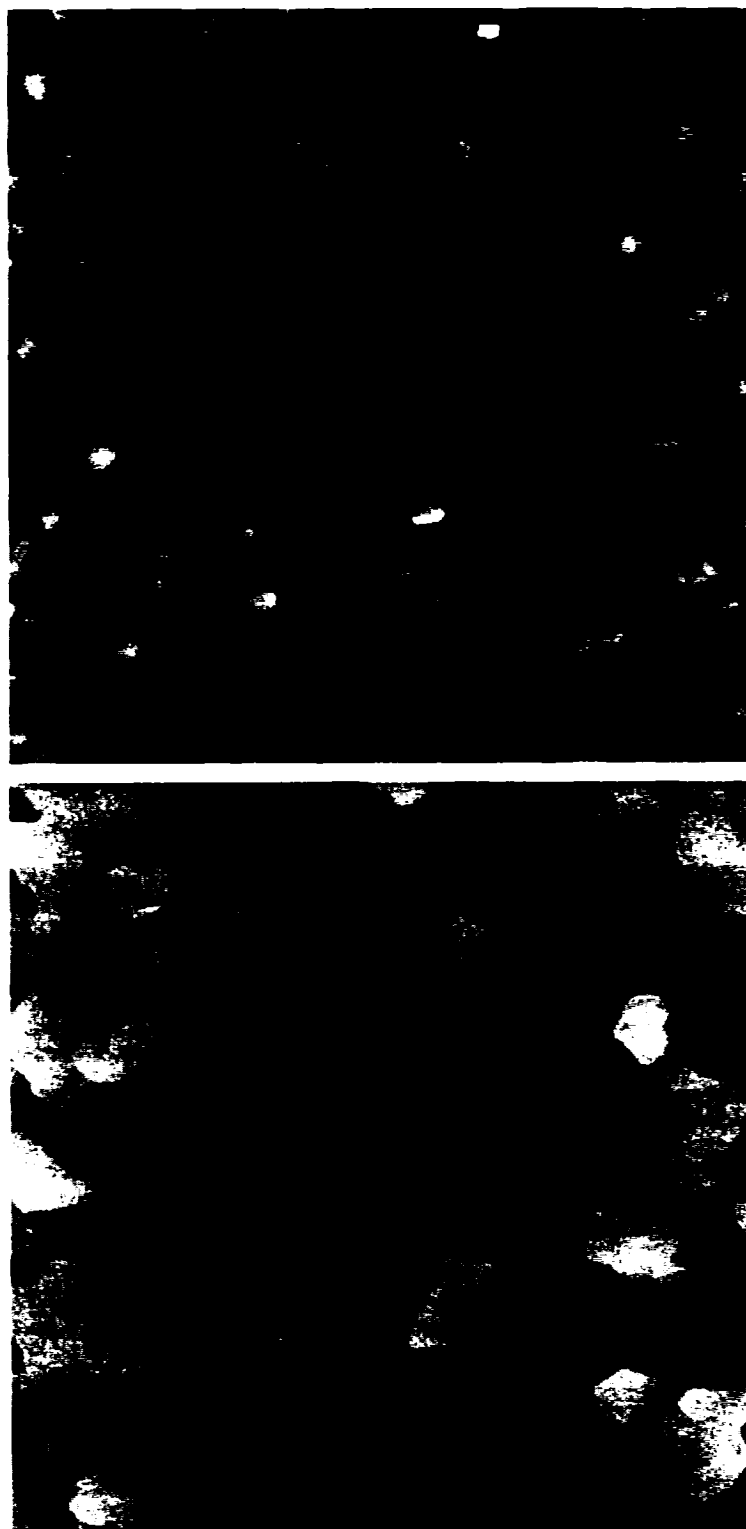


**Figure 3.17:** STM images ( $3\ \mu\text{m} \times 3\ \mu\text{m}$ ) of small-grained (A) and large-grained (B) gold. Tip bias of 600 mV and a tunneling current setpoint of 35 pA were used to acquire both images. Height contrast scale = 14 nm.



In the case where the thickness and surface stress measurements are simultaneously performed on two separate samples, it is important to assess both gold surface morphologies to make sure that they are sufficiently similar to warrant a correlation between the two measurements. Here, gold was simultaneously evaporated onto both the SiN<sub>x</sub> cantilever and freshly cleaved Mica [96]. STM was used to confirm that the morphology of the gold surfaces formed on both substrates was similar in terms of grain size and roughness.

Imaging the resultant alkanethiol SAM after exposure required some sample manipulation. SAM covered samples were rinsed with anhydrous ethanol and blown dry with ultra-high purity (UHP) nitrogen prior to imaging, ridding the surface from residual alkanethiols (physisorbed) or contaminants present at the SAM-air interface. This procedure yielded the best STM images with molecular resolution.

## 4 Calibration

Cantilever-based chemical sensors work by allowing the transduction of a chemical signal into a mechanical deflection of the cantilever beam. The surface stress induced by the adsorption of target analytes onto the cantilever surface is monitored as a deflection of the cantilever. In order to quantify this surface stress, the sensor must be calibrated, which involves converting the photo-detector signal into an actual cantilever deflection, which in turn is converted into a surface stress.

It is often difficult to interpret cantilever-based sensor results found in the literature because authors often fail to accurately quantify their results in terms of surface stress. In fact, it is not uncommon to find surface stress results quoted in terms of cantilever deflections, as a voltage proportional to the deflection, or even in arbitrary units [15,20,22,27,41]. Even in the cases where the authors quote values of surface stress, their numbers are often based on crudely calibrated systems, without error estimates, making reliability an issue. This can make it difficult to interpret the results, and even impossible to compare them to other studies found in the literature. In fact, converting the measured signal into a surface stress is non-trivial. Consequently, a methodology used to convert the measured cantilever deflection signal into an accurate measure of surface stress was developed [97], and is the subject of the present chapter.

## 4.1 Cantilever Deflection Measurement

### 4.1.1 Deflection Calibration: Simple Method

The deflection of the cantilever is monitored using the optical beam deflection technique, as outlined in Section 3.1.2. Calibration of the optical beam involves correlating the displacement of the reflected laser beam on the PSD,  $\Delta S$ , with the actual cantilever deflection,  $\Delta z$ . Figure 4.1 allows us to state the following:

$$\tan \varphi = \frac{\Delta z}{l} \qquad \tan(2\varphi) = \frac{\Delta S}{L} \qquad \text{Equation 4.1}$$

where  $l$  is the length of the cantilever,  $\varphi$  is the deflection angle of the cantilever, and  $L$  is the distance between the apex of the cantilever and the PSD. Equation 4.1 ignores the curvature of the cantilever, an assumption which is valid for small deflections ( $\Delta z \ll l$ ). From Equation 4.1, the deflection of the cantilever,  $\Delta z$ , can be written as a function of the measured displacement of the reflected beam on the PSD,  $\Delta S$ :

$$\Delta z = \left( \frac{l}{2L} \right) \Delta S \qquad \text{Equation 4.2}$$

by letting  $\tan \varphi \approx \varphi$ , valid for small  $\varphi$ .

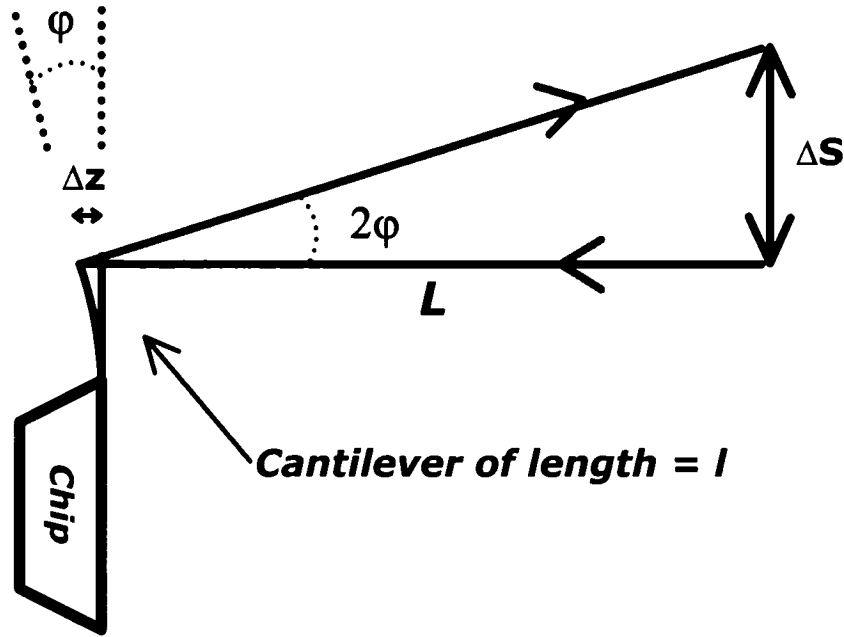


**Figure 4.1:** The laser beam deflection technique is used to infer the deflection of the cantilever,  $\Delta z$ , from the measured displacement of the reflected beam,  $\Delta S$ , on the PSD.  $\Delta S$  increases as the cantilever deflects. The cantilever of length,  $l$ , positioned a distance,  $L$ , from the PSD deflects by an angle,  $\phi$ . The red lines indicate the incoming and reflected laser beams.

The relationship expressed in Equation 4.2 makes it easy to infer the cantilever deflection from the measured PSD signal. Unfortunately, accurately measuring the distance between the cantilever and the PSD,  $L$ , is difficult. This distance can be measured with a maximum precision of approximately 1 mm when measured with a ruler. This translates into an uncertainty in the cantilever deflection of 10% or more for typical setup configurations. A more stringent calibration is necessary in order to reduce the uncertainty in the surface stress measurement.

#### 4.1.2 Deflection Calibration: Fiber Interferometer

A home-built fiber interferometer is used to accurately calibrate the cantilever deflection measurement. During calibration, the deflection of the cantilever is

simultaneously monitored using the optical beam technique and the fiber interferometer. The fiber interferometer monitors the cantilever deflection from the backside, while the optical beam technique is used on the front side, as depicted in Figure 4.2.

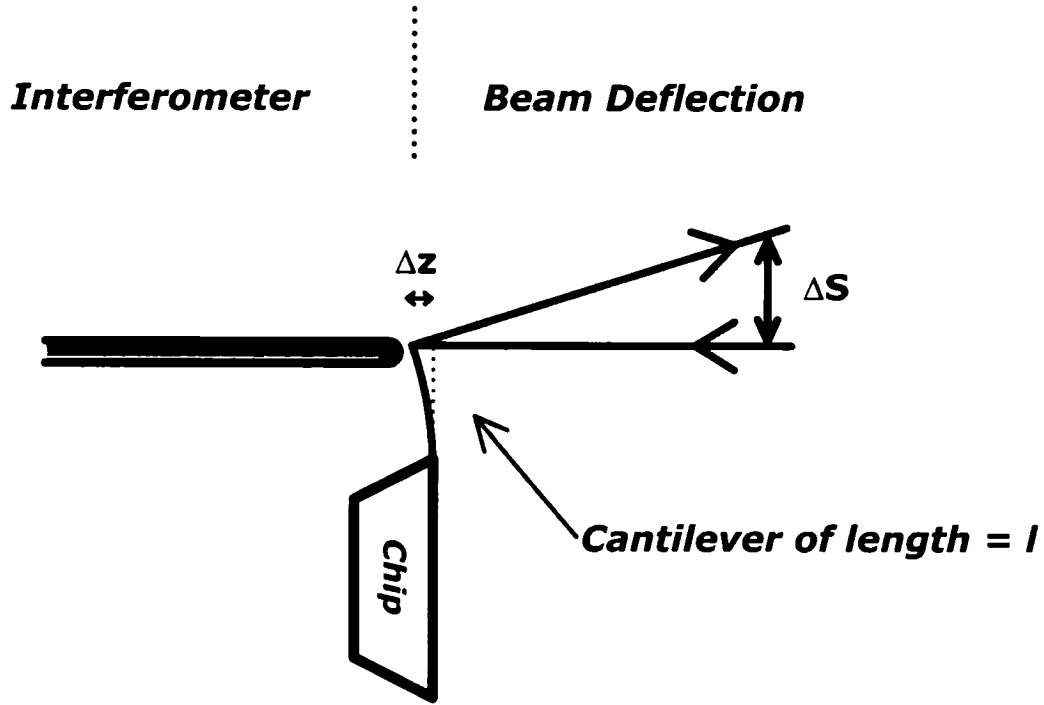


**Figure 4.2:** During calibration, the deflection of the cantilever is simultaneously monitored using the beam deflection technique and a fiber interferometer. The deflection of the cantilever is monitored using both methods from opposite sides.

It is possible to calibrate the PSD signal in terms of the actual cantilever deflection measured using the fiber interferometer, which yields a direct deflection measurement. This procedure yields a calibration constant,  $C_{cal}$ , which is used to convert the measured PSD signal,  $\Delta S$ , into a cantilever deflection,  $\Delta z$ ,

$$\Delta z = C_{cal} \Delta S$$

**Equation 4.3**

The interferometer output is given by

$$V_{\text{int}} = A \sin\left(\frac{2\pi}{\lambda} 2\Delta z + \xi\right) + B \quad \text{Equation 4.4}$$

where **A** and **B** are constants,  $\xi$  is a phase angle, and  $\lambda$  is the interferometer wavelength. By substituting Equation 4.3 into Equation 4.4, we can write the interferometer signal in terms of the PSD signal:

$$V_{\text{int}} = A \sin\left(\frac{4\pi}{\lambda} C_{\text{cal}} \Delta S + \varphi\right) + B \quad \text{Equation 4.5}$$

A plot of the interferometer signal,  $V_{\text{int}}$ , as a function of the PSD signal,  $\Delta S$ , gives a sinusoidal wave, with frequency,  $K_{\text{int}}$ , which makes it possible to evaluate the calibration constant,  $C_{\text{cal}}$ , as follows:

$$C_{\text{cal}} = \frac{K_{\text{int}} \lambda}{4\pi} \quad \text{Equation 4.6}$$

During calibration, the deflection of the cantilever is induced by heating a gold-coated cantilever by applying approximately 10 volts to a 1.5 k $\Omega$  surface-mount resistor. This resistor is glued to the chip onto which the cantilever is mounted using thermally conductive, but electrically isolating glue. The cantilever bends when it is heated due to the bimetallic effect. The deflection measurements are performed during cooling, when the heater is turned off after about 5 seconds of heating.

The position of the fiber interferometer relative to the cantilever apex is of particular importance for the calibration procedure. The cleaved end of the fiber interferometer is positioned at the cantilever apex by sweeping the fiber across (perpendicular to the length of the cantilever) the apex of the V-shaped cantilever

while monitoring the interferometer output. The positions at which the interferometer output vanishes are noted, and the fiber is repositioned half way in between these two positions. Then, the fiber is moved up the apex (along the length of the cantilever) until the signal just vanishes. Repeating this positioning procedure ensures that the fiber is reproducibly positioned as close to the end of the cantilever apex as possible. The actual position of the fiber is estimated given the fiber's numerical aperture (sine of half the angle of divergence) and the distance between the end of the fiber and the cantilever surface. This distance is approximately half of the fiber's diameter of 80  $\mu\text{m}$ , and the numerical aperture is quoted to be 0.16 by the fiber's manufacturer. Given that the fiber's core diameter is 4  $\mu\text{m}$ , we infer that the size of the laser spot at that distance is then approximately 17  $\mu\text{m}$ . Given that about half of the laser light re-enters the fiber, we deduce that the fiber is positioned a distance,  $\Delta l$ , of 8.5  $\mu\text{m}$  from the end of the apex. Essentially,  $\Delta l$  gives the actual position at which the cantilever deflection is measured. Therefore, the cantilever deflection measured this way must be corrected by a factor of  $l^2/(l-\Delta l)^2$  in order to obtain the real deflection of the end of the cantilever. This correction factor is derived from Equation 4.14 below.

### 4.1.3 Implementation

Figure 4.3 shows a typical dataset acquired during a single calibration run. A plot of the interferometer signal versus the PSD signal is shown in Figure 4.4 (left). The power spectral density of this data is also shown in Figure 4.4 (right) with a Lorentzian fit. From these data, we find the spectral peak position to be centered at  $337 \pm 1 \text{ V}^{-1}$ . Then,  $C_{cal}$  is calculated to be  $(1.703 \pm 0.005) \times 10^{-5} \text{ m/V}$  based on Equation 4.6. This deflection calibration constant is valid as long as the cantilever-PSD distance remains unchanged. This is true as long as the PSD aren't moved between experiments.

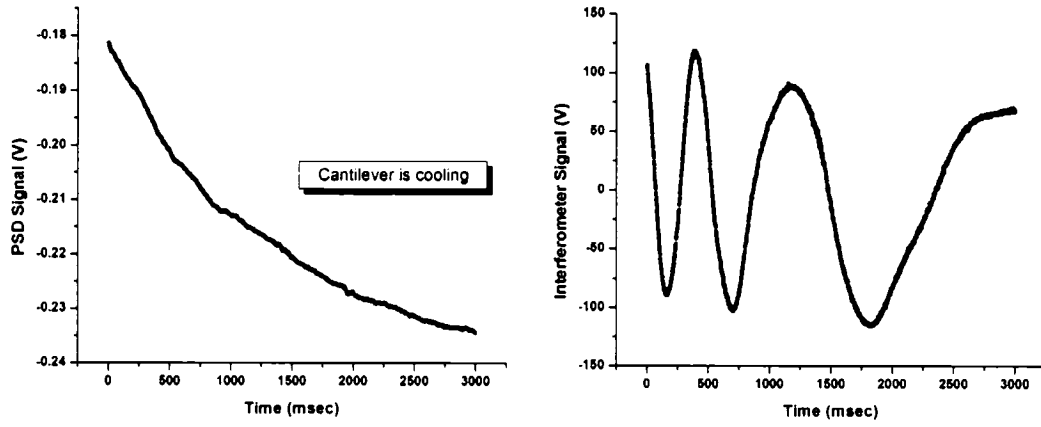


**Figure 4.3:** PSD (left) and fiber interferometer (right) signals as a function of time during cooling for a typical calibration run. The PSD signal decreases monotonically as the cantilever is cooled, whereas the interferometer signal oscillates as it goes through constructive and destructive interference.

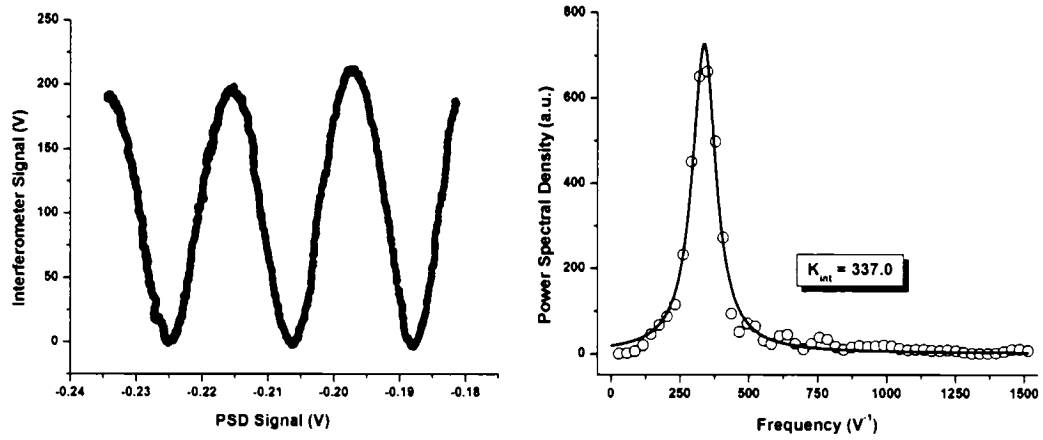


**Figure 4.4:** Interferometer signal versus PSD signal (left) during cooling for a typical calibration run. The slight increase in amplitude is due to an increase in reflection intensity of the interferometer signal as the cantilever bends. This does not affect the result of interest, which is the oscillation frequency. The power spectral density (circular data points) of the graph on the left is plotted on the right. A Lorentzian fit (red curve) is applied to determine the peak position, corresponding to  $K_{int}$ .



The reliability of this calibration procedure was tested by conducting a number of calibration runs verifying the effect of repositioning the cantilever, and of realigning the focused laser beam, both of which are routinely done between experiments. Even though the cantilever chip is placed in a designated groove in the cell, its position varies slightly when repositioned. Furthermore, the laser beam is reproducibly focused onto the cantilever apex by maximizing the intensity signal measured by the PSD, which ensures minimal intensity loss due to misalignment.

Table 3 summarizes the variability encountered in subsequent experiments due to repositioning the cantilever and refocusing the laser beam used for the optical beam deflection technique. In order to estimate the variability in the calibration constant involved in refocusing the laser on a specific spot on the apex of the cantilever from experiment to experiment, several calibration runs (6 runs) were performed, between which the laser was purposely misaligned and then refocused. The variability in repositioning the cantilever chip at the start of every experiment was measured by removing the chip, and repositioning it (5 runs) in the cell between calibration measurements.

<i>Variability of...</i>	<i>Percent Deviation</i>
Measurement of $K_{\text{int}}$	0.8%
Chip Repositioning	1.1 %
Laser Refocusing	1.6%

**Table 3: Factors affecting the uncertainty in the measurement of the cantilever deflection. The percent deviations are the ratios of the standard deviation to the corresponding values of  $K_{\text{int}}$ . The calibration procedure itself has a small uncertainty (0.8%). Both chip repositioning and laser refocusing yield deviations under 2%.**

The cantilever deflection is measured with an uncertainty of less than 1% (uncertainty in the calibration procedure itself). In our setup, repositioning the cantilever and refocusing the laser beam onto the cantilever apex between experiment results in an increased uncertainty in the deflection measurement. Nevertheless, the deflection measurements uncertainty is kept under 2%. This uncertainty is adequate, but could be reduced by machining more precise alignment grooves to ensure that the cantilever is repositioned more reproducibly from experiment to experiment. More sensitive positioners used to focus the laser beam onto the cantilever apex could potentially further reduce this uncertainty.

## 4.2 Quantifying Surface Stress

### 4.2.1 Methodology

The surface stress associated with the bending of a substrate can be calculated using Stoney's formula [98]. Stoney derived this formula in 1909 to calculate the surface stress observed during the deposition of thin nickel films onto thin steel sheets. The surface stress is deduced from a measurement of the substrate's radius of curvature, as formulated here:

$$\sigma_s^+ - \sigma_s^- = \frac{Et^2}{6R(1-\nu)} \quad \text{Equation 4.7}$$

where  $\sigma_s^+$  and  $\sigma_s^-$  are the surface stresses applied to the upper and lower surfaces of the substrate, respectively,  $E$  is the substrate's Young's modulus,  $t$  is its thickness,  $R$  is the substrate's radius of curvature, and  $\nu$  is its Poisson's ratio.

Many have discussed the validity of Stoney's formula as it applies to cantilever beams. This formula is derived for unclamped substrates. Since cantilever beams are clamped at one end, the induced curvature strays away from being perfectly

circular, and the formula's validity becomes questionable. But for most AFM cantilever geometries, Stoney's formula can still be used to calculate the surface stress with minimal error [99,100,101].

A bigger concern is the fact that the cantilever's elastic properties, Young's modulus and Poisson's ratio, must be known in order to apply Stoney's formula (Equation 4.7). A problem arises in the case of commonly-used silicon nitride AFM cantilevers. Since these  $\text{SiN}_x$  cantilevers are typically made from a chemical vapor deposition process, the exact atomic ratio between Si and N is often not well defined [102]. The result is that the uncertainty in Young's modulus is very high ( $E \approx 130 - 385$  GPa) [102,103], making the surface stress calculation less reliable. The addition of metallic coatings compounds the problem as it can significantly modify the cantilever's elastic properties.

Consequently, an alternate formula relating the cantilever's deflection to an applied surface stress is derived here [97]. This new approach eliminates the need to know the cantilever's Young's modulus in calculating the surface stress. The formula is derived by assessing the energy stored in the stressed cantilever, and by measuring the cantilever's spring constant.

The energy stored in a bent cantilever can be calculated using two approaches. The first approach uses Hooke's law to calculate the energy given the cantilever's measured spring constant,  $k$ , and deflection,  $\Delta z$ .

However, Hooke's law must be modified to account for the fact that the measured spring constant is typically associated with the AFM experiment, where the cantilever's deflection is the result of a concentrated load applied at the apex (tip) of the cantilever. In the sensor's case, the deflection results from an isotropic surface stress, which acts over the entire surface of the cantilever.

Thus, the energy stored in a stress cantilever,  $E_k$ , is expressed using a modified Hooke's law stated as:

$$E_k = \left( \frac{4}{3(1-\nu)} \right) \frac{1}{2} k \Delta z^2 \quad \text{Equation 4.8}$$

In Equation 4.8,  $k$  refers to the spring constant associated with the typical AFM experiment, where a concentrated force is applied at the apex of the cantilever. However,  $k$  is replaced by  $k/(1-\nu)$ , where  $\nu$  is the cantilever's Poisson's ratio, since the surface stress acting on the cantilever is isotropic. The cantilever is effectively stiffer in the longitudinal direction because the cantilever also experiences a slight transverse curvature. Additionally, a factor of 4/3 is included in Equation 4.8 to account for the different curvatures resulting from a uniform surface stress, as opposed to a concentrated load applied at the tip [see *Appendix*].

The energy stored in a stressed cantilever can also be calculated using [104,105]:

$$E_{elastic} = \int_0^l \frac{M^2}{2E^* I} dy \quad \text{Equation 4.9}$$

where  $M$  is the cantilever beam's bending moment,  $E^*$  is its biaxial modulus [102,100], which is related to Young's modulus  $E$  as  $E^* = E/(1-\nu)$ ;  $I$  is the area moment of inertia, and the integration is carried over the length of the cantilever,  $l$ .

Equation 4.9 can be altered by incorporating the differential equation for an elastic beam [106], written as:

$$\frac{d^2 z}{dy^2} \cong \frac{1}{R} = \frac{M}{E^* I} \quad \text{Equation 4.10}$$

This substitution removes  $E^*$  and  $I$  from Equation 4.9 and introduces the radius of curvature of the cantilever,  $R$ :

$$E_{elastic} = \int_0^l \frac{M}{2R} dy \quad \text{Equation 4.11}$$

The bending moment  $M$ , denoted by  $M_{rect}$  and  $M_{\Delta}$  for rectangular and triangular (V-shaped) cantilevers, respectively, is written in terms of geometrical quantities [107]:

$$M_{rect} = \frac{Wt\Delta\sigma}{2} \quad \text{Equation 4.12}$$

$$M_{\Delta} = \begin{cases} Wt\Delta\sigma & \text{for } 0 \leq y \leq l_1 \\ \frac{tb(l-y)\Delta\sigma}{2l} & \text{for } l_1 < y \leq l \end{cases} \quad \text{Equation 4.13}$$

where  $W$ ,  $t$ ,  $l$ ,  $l_1$ , and  $b$  are depicted in Figure 3.2, and  $\Delta\sigma$  is the difference in surface stress between the top and bottom surfaces of the cantilever.

In addition, the radius of curvature,  $R$ , can be written in terms of the measured cantilever deflection,  $\Delta z$ :

$$R = \sqrt{y^2 + z^2} = \frac{l^2}{2\Delta z} + \frac{\Delta z}{2} \approx \frac{l^2}{2\Delta z} \quad \text{Equation 4.14}$$

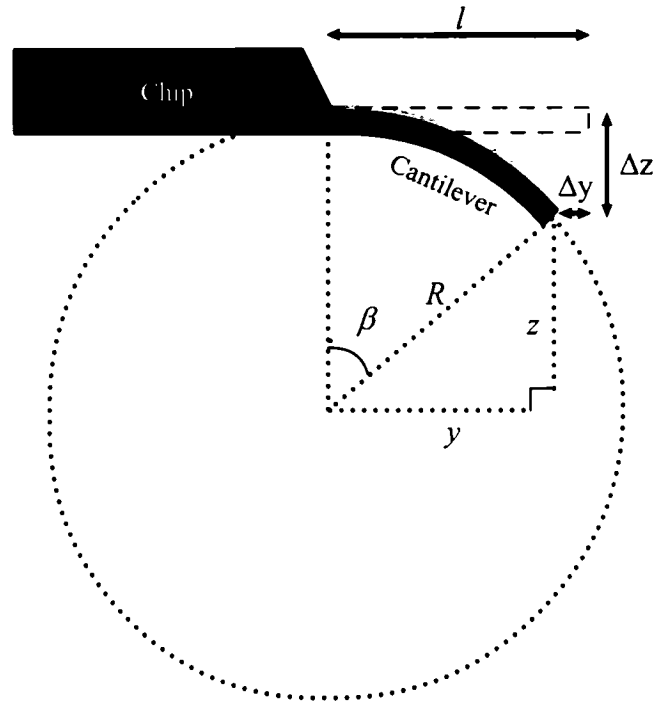


**Figure 4.5:** The deflection of the cantilever can be defined in terms of a radius of curvature. The curvature of the cantilever beam under surface stress is approximately circular.

From Figure 4.5, we can see that  $z = R - \Delta z$  and  $y = l - \Delta y \approx l$  since  $l \gg \Delta y, \Delta z$ . Although the cantilever does not bend circularly when subjected to an isotropic surface stress, the radius of curvature is taken to be constant over the length of the cantilever. This approximation was found to be valid as long as the deflection,  $\Delta z$ , is much smaller than the overall length of the cantilever,  $l$ .

Finally, by equating Equation 4.8 and Equation 4.11, the surface stress can now be written as a function of the measured deflection and spring constant. The requirement that the cantilever's Young modulus be known, imposed by Stoney's equation, has been eliminated and replaced by the cantilever's spring constant, a quantity that is readily measurable.

The results are summarized in Equation 4.15 and Equation 4.16 for rectangular and triangular cantilevers respectively.

$$\Delta\sigma = \frac{4}{3(1-\nu)} \frac{l}{Wt} k_{rect} \Delta z \quad \text{Equation 4.15}$$

$$\Delta\sigma = \frac{2}{3(1-\nu)} \left[ \frac{l^2}{Wtl_1 + \frac{tb}{4l}(l-l_1)^2} \right] k_{\Delta} \Delta z \quad \text{Equation 4.16}$$

where  $k_{rect}$  and  $k_{\Delta}$  are the spring constants for rectangular and triangular cantilevers, respectively [97].

#### 4.2.2 Implementation

The variables in Equation 4.15 and Equation 4.16 are all readily measurable with the exception of Poisson's ratio.  $W$ ,  $l$ ,  $l_1$ , and  $b$  can be measured with a calibrated optical microscope or with a scanning electron microscope (SEM). The cantilever thickness,  $t$ , is measurable with a calibrated AFM, a precise SEM, or deduced from a measurement of the rectangular cantilever's spring constant [108]. This latter method can be used to deduce a triangular cantilever's thickness if a rectangular cantilever is found on the same chip, since it can be assumed that the thickness of all the cantilevers on the same chip is the same. Nonetheless, a field-emission SEM was used to measure the thickness of the cantilever, and yielded an uncertainty of 1.4%. The uncertainty in all other geometrical parameters is negligible compared to the uncertainty in the thickness measurement.

There are four main methods available for evaluating the spring constant of an AFM cantilever. The simplest is based on the knowledge of the cantilever Young's modulus and geometry.

The spring constant of a rectangular cantilever can be evaluated using [108]:

$$k_{rect} = \frac{Et^3w}{4l^3} \quad \text{Equation 4.17}$$

This approach does not work well for our experiments, since we used SiN<sub>x</sub> cantilevers for which Young's modulus is unknown, or at least contains a large uncertainty. Moreover, an uncertainty in the measurement of the thickness,  $t$ , results in a large uncertainty in the calculated spring constant,  $k_{rect}$ .

*Sader's method* [108] involves measuring the rectangular cantilever's resonant frequency and quality factor,  $Q$ , in air. In our case, the thermal resonance peak was acquired using a spectrum analyzer with the PSD signal as an input. Alternatively, the power spectrum can be acquired using a data acquisition card (ADC). In the case where a triangular cantilever is mounted on the same chip as a rectangular, Sader also developed a methodology [108,109] to infer the triangular cantilever's spring constant from a measurement of this rectangular cantilever's spring constant. If a rectangular cantilever is not found on the same chip as the triangular cantilever of interest, its spring constant can be evaluated using the *thermal method*. The *thermal method* involves a measurement of the cantilever's thermal resonance peak, with the added constraint that the amplitude of the power spectrum be calibrated in term of cantilever deflections. The fourth, less frequently used method is the *added-mass method* developed by Cleveland *et al* [110]. This method involves monitoring the cantilever's resonant frequency for various added masses glued to the apex of the cantilever. This last method is seldom used as it requires some delicate manipulation, and is often destructive. Sader's method for measuring the cantilever's spring constant has been favored in this study.

Commercially available AFM cantilevers are usually shipped as part of a wafer of a few hundred cantilevers. A survey of the spring constants of several cantilevers



originating from different areas of the wafer was conducted to assess the uniformity of the cantilevers' elastic properties across the wafer. The variability of the measured spring constants of cantilevers taken randomly from a wafer was found to be less than 2%. From this result, we found it reasonable to assume that the spring constant was uniform over a wafer, and eliminated the need to measure the spring constant of every cantilever used in every experiment.

The largest source of uncertainty in the surface stress measurement comes from Poisson's ratio. We took Poisson's ratio to be equal to 0.25 since both silicon nitride, and the Au(111) coating are isotropic materials [111]. Poisson's ratio for SiN<sub>x</sub> has been quoted in the literature in the range of 0.2-0.3 [102]. This uncertainty in Poisson's ratio increases the total uncertainty in the calculated surface stress to 7% as calculated using Equation 4.15. However, most values quoted in the literature are in the range of  $0.25 \pm 0.02$  [102,103,109,112,113]. This reduces the typical total uncertainty in the surface stress calculation to 4%.

### **4.3 Instrument Sensitivity and Resolution**

A methodology used to obtain a quantitative surface stress measurement from the measurement of the cantilever deflection was developed and is presented here. Given an instrumental deflection sensitivity of approximately 0.2 nm, this instrument yields a surface stress resolution of  $5 \times 10^{-5}$  N/m (given the use of cantilever 'C' in Figure 3.2, with  $k = 0.01$  N/m).

The total uncertainty in the calculated surface stress is a function of the uncertainties in all the variables stated in Equation 4.15 or Equation 4.16. The overall uncertainty mainly arises, in decreasing order of importance, from the uncertainties in Poisson's ratio, the spring constant, the deflection measurement, and the measured cantilever thickness, which were determined to be approximately 8%, 2%, 2% and 2%, respectively. This translates into a total

uncertainty in the measured surface stress of approximately 4%. Thus, if one seeks to reduce the overall uncertainty in the calculated surface stress, the uncertainties in these four parameters should be reduced. Improvement in the determination of Poisson's ratio could be made by using a cantilever material with better-known elastic properties (e.g. single crystal silicon cantilevers). Improvements in the measurements of the cantilever's spring constant and thickness and in the deflection measurement would be difficult, but could in principle be improved. Nevertheless, the low uncertainty attained using the current system and methodology is already exceptional, and sufficient for the measurements described in the present work. The ability to accurately quantify the surface stress with precision and with high resolution is essential when using these cantilever-based sensors to study molecular processes. A confidence in the surface stress measurement empowers us to apply a more theoretical understanding of the mechanisms that drive the self-assembly process in the case of alkanethiol SAM formation, and of the origins of the surface stresses central to these sensors' response.

## **5 Alkanethiol Self-Assembled Monolayers**

The measurement of the surface stress induced during the formation of alkanethiol SAMs on gold-coated cantilever was performed in order to obtain a fundamental understanding of the sensor's response. An appreciation of the mechanisms that drive alkanethiol self-assembly and the induced surface stress will also translate into a better understanding of molecular systems involved in other sensing applications. The experiments described in this chapter aim to identify the main factors that most influence the self-assembly process. Identification and control of these factors are essential in obtaining reproducible and reliable results. On the basis of optimizing this sensor platform, controlling the factors that affect reproducibility and reliability of the measured signal is crucial if cantilever-based sensors are to be used as a viable technology. Moreover, the results shown here will also elucidate some of the discrepancies found in the literature surrounding the interpretation of alkanethiol SAM-related results.

This chapter begins by reviewing chemical self-assembly as it relates to alkanethiol SAM formation before exploring some factors that strongly influence the alkanethiol self-assembly process.

### ***5.1 Chemical Self-Assembly***

Chemical self-assembly refers to the spontaneous organization of matter at the molecular scale. Given certain environmental conditions, some self-organized systems can become quite complex, as is the case in many biological systems.

Scientists have long tried to seek ways to harness the advantages of chemical self-assembly to make useful structures for a multitude of applications. The chemical functionalization of thiolated SAMs is increasingly being used for highly specific chemical and biological sensing applications. An understanding of the driving forces at the core of molecular self-assembly is essential in developing and optimizing this new class of micro-mechanical sensors.

Alkanethiol  $[\text{HS}(\text{CH}_2)_n\text{CH}_3]$  self-assembled monolayers are one of the most widely studied self-assembled systems because of their versatility and stability [87,114,115]. Alkanethiol SAMs have long been viewed as a simple model system whose properties can be applied to more complex self-assembled systems. Alkanethiol SAMs provide stable and ordered structures on surfaces, which are envisaged to be useful in a broad range of applications, including protective coatings, wetting control, friction and adhesion control, and electronics [5,6, 114].

However, recent studies have revealed that the self-assembly process of alkanethiol SAMs is much more complex than previously expected. Several experimental techniques have revealed that the kinetics of alkanethiol SAM formation is characterized by more than one process with different time constants. Techniques, such as STM and FTIR (Fourier Transform Infrared Spectroscopy), have been used to identify structural phase transitions that occur within the monolayer as part of the assembly process. Diffraction studies have provided some detail concerning the interaction between the SAM and the underlying substrate. Nevertheless, questions remain concerning the many mechanisms involved during the self-assembly process, with respect to structure, kinetics, and the extent of the interaction with, and modification of the underlying gold substrate. [87,116]

The self-assembly of alkanethiol SAMs onto gold surfaces is driven by the molecule's thiol head group's high affinity for gold. This sulfur atom forms a strong covalent bond [ $\sim 185$  kJ/mol] with gold surface atoms [117], following

dissociation of the S-H bond. The exact binding site of alkanethiol molecules on a gold surface is still the subject of debate in the literature. Y. Yourdshahyan *et al* [118] have used first principles methods in calculating the preferred adsorption site, and compared their results with other published calculations. They have found that the minimum energy adsorption site is the so-called bri-fcc site (shifted from the bridge site towards the fcc site), in agreement with an experimental high-resolution electron energy loss spectroscopy (HREELS) study [119]. They also present calculations done by others that find the preferred adsorption site to be the fcc site, or even the bri-hcp site. Nevertheless, this issue remains to be resolved as different calculations performed by different groups do not always agree. In addition, the alkyl chains of adjacent alkanethiol molecules in a SAM interact, and lineup, yielding a SAM where these alkyl chains organize themselves almost perpendicularly to the gold surface. The underlying van der Waals interactions between adjacent chains result in different degrees of molecular tilt, depending on the strength of these interactions, typically a function of molecular chain length or varying endgroups. Figure 5.1 is a schematic showing a side-view of an alkanethiol SAMs at equilibrium. In the case of dodecanethiol (C12), this molecular tilt is approximately 30° [120].

STM studies of alkanethiol SAMs have revealed that SAM formation strongly influences the underlying gold substrate. Charge transfer between the adsorbates and the Au surface atoms results in changes in local charge density, which have been previously observed by STM as changes in the reconstruction of an Au(111) surface (deconstruction) [121,122]. Further evidence of this strong interaction is revealed by the formation of etch pits on the Au surface due to the formation of alkanethiol SAMs. Gold atoms are ejected from the surface, creating vacancies that coalesce into vacancy islands (or etch pits) having a depth of a single Au layer. The mechanisms guiding the formation of these vacancy islands are still being investigated in the literature. G. E. Poirier [121] has used STM to link the presence of etch pits on an alkanethiol SAM-covered gold surface to the relaxation of the compressed herringbone structure of reconstructed Au(111), as

opposed to standard chemical etching [122]. Alkanethiol adsorption is thought to promote the ejection of the extra gold atom characteristic of a reconstructed Au(111) surface, although the driving force for the ejection of extra Au atoms remains an unresolved issue.

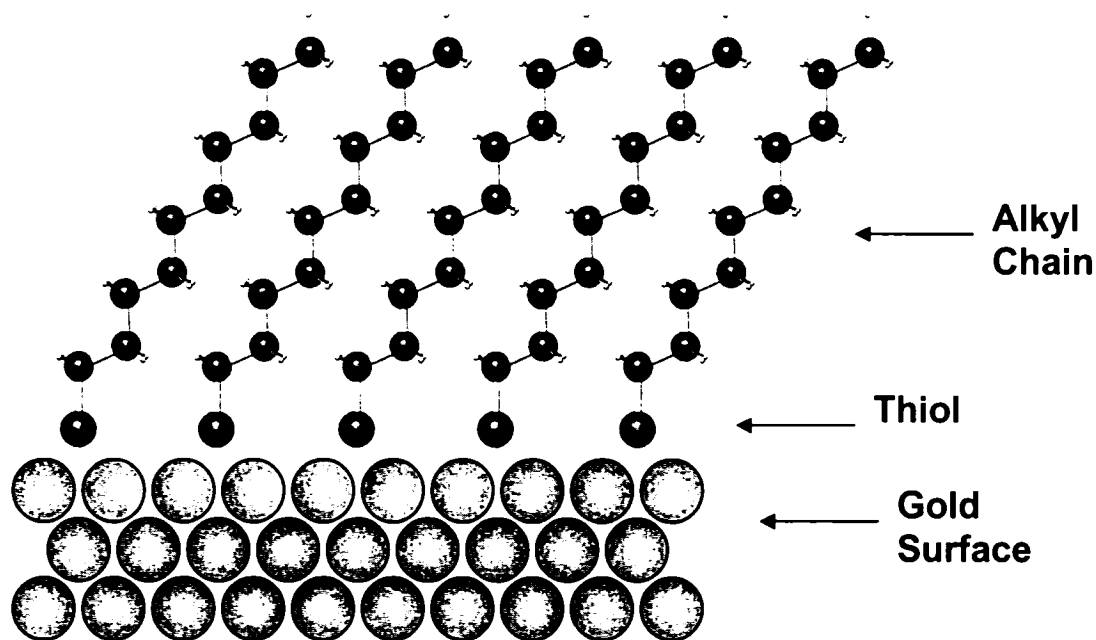


**Figure 5.1:** Side view of an alkanethiol SAM on gold. The alkanethiol molecule is comprised of a thiol (sulfur) head group (bound to the gold surface) and an alkyl chain. In this example, the molecule is a decanethiol (C10 - 10 carbons).

## 5.2 Kinetics of Alkanethiol SAM Formation

Several experimental techniques have been used to investigate the formation process of alkanethiol SAMs. Certain experimental techniques have shown that the formation of alkanethiol SAMs occurs in two distinct processes. In fact, many groups have observed that SAM formation is mediated by two or more processes with different time constants. For example, Schreiber *et al* [123] used XPS (x-ray photoelectron spectroscopy), LEAD (low energy atom diffraction) and GIXD (grazing incidence x-ray diffraction) to observe a rapid first process associated with the

formation of so-called *lying-down* phases (lower density phase where the molecule lie parallel to the gold surface), followed by a second, much slower process attributed to the transition into the *standing-up* phase (fully-formed SAM). Others [124,125,126,127,128,129] have suggested that the typically much slower second process (the transition into the standing-up phase) can be accompanied or followed by a reorganization (recrystallization) of the alkyl chains, where gauche defects, or kinks, in the longer alkyl chains are eliminated, and the SAM assumes an all-trans state. Recently, STM imaging has yielded a much greater insight into the formation process of alkanethiol SAMs by identifying several structural phase transitions leading to a fully-formed SAM [82,130].

Figure 5.2 schematically depicts three of several structural phases that occur during SAM formation. Initially, alkanethiol molecules physisorb, and form a 2-D lattice-gas on the gold surface, where the molecules remain highly mobile. Chemisorption occurs at a slightly higher coverage initiating the nucleation of islands of alkanethiol molecules having their alkyl chains parallel to the gold surface in a series *lying-down* phases. Several STM studies have revealed that these low-coverage *lying-down* phases organize themselves such that the sulfur atoms line-up, and are imaged as stripes by STM [82]. Consequently, these *lying-down* phases are often referred to as *striped* phases. STM analysis has also shown that these various *lying-down* phases are identified by different unit cells, corresponding to different alkanethiol densities on the surface. The alkyl chains of the molecules in the lying-down phases can be *unstacked* or *stacked*, as schematically shown in Figure 5.2. The *unstacked lying-down* phase is the lower density phase, where the alkyl chains lie flat on the gold surface. The higher coverage *stacked lying-down* phase is characterized by the alkyl chains assuming an interdigitated bilayer on the gold surface [82]. Other intermediate *lying-down* phases exist, but are not depicted in Figure 5.2. The formation of the *lying-down* phases is the result of chemisorption.

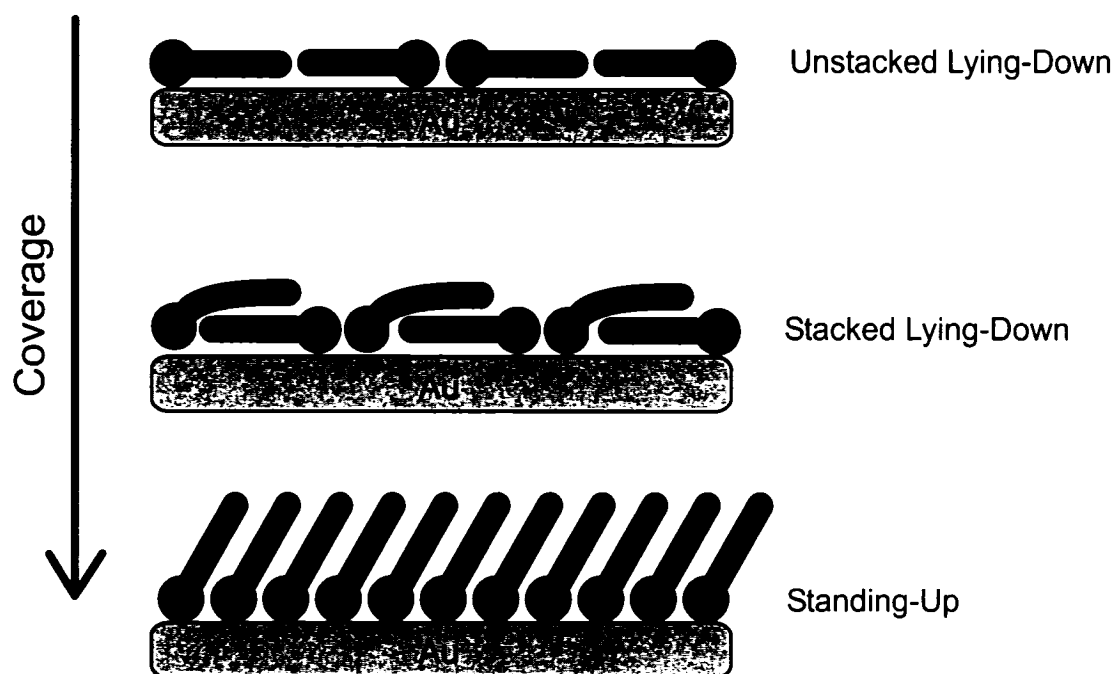


**Figure 5.2:** SAM formation is characterized by a series of structural phase transitions as coverage increases. Depicted are the *unstacked lying-down*, *stacked lying-down*, and *standing-up* phases. Other intermediate phases exist but are not depicted.

The SAM subsequently undergoes another phase transition, where the alkyl chains of the alkanethiol molecules orient themselves nearly vertically on the gold surface forming the *standing-up* phase. The alkyl chains are typically tilted with respect to the surface normal by approximately  $30^\circ$ . STM studies have shown that the transition into the *standing-up* phase is triggered by the nucleation of a disordered precursor state, usually at the domain boundaries of the *lying-down* domains [82]. The resultant SAM reaches the *standing-up* phase, and assumes a  $(\sqrt{3} \times \sqrt{3})R30^\circ$  structure relative to the gold surface. A  $c(4 \times 2)$  superstructure [131] (also referred to as the  $p(3 \times 2\sqrt{3})$  superstructure) of the  $(\sqrt{3} \times \sqrt{3})R30^\circ$  lattice is also observed by STM. The existence of this superstructure has been attributed to different orientations of the terminal methyl groups at the SAM interface, and is associated with a high-quality, defect-free SAM. This is widely accepted as being the final, stable structure of the alkanethiol SAM on gold. The formation of the *standing-up* phase can be accompanied or followed by reorganization



(recrystallization) of the alkyl chains of the alkanethiol molecules forming the SAM. This reorganization of the SAM has been attributed to the filling of molecular vacancy sites, and to the straightening the alkyl chain, eliminating gauche defects [128]. These gauche defects, or kink, present in the alkyl chain are usually found in relatively long alkanethiol SAMs ( $>C_{12}$ ). Although not depicted in Figure 5.2, different phases can coexist in adjacent domains.

Figure 5.3 shows how these various phases evolve for hexanethiol SAM formation as a function of exposure (1 Langmuir =  $10^{-6}$  Torr·sec =  $1.33 \times 10^{-4}$  Pa·sec), as discussed by Kondoh *et al* [132]. Nevertheless, some [118,133,134] report that a SAM can become kinetically trapped, where the monolayer remains in a metastable intermediate phase (lying-down phase, for example). The concept of kinetics trapping contradicts the assertion by Kondoh (i.e. Figure 5.3) that says that the SAM will eventually reach the standing-up phase given enough time.

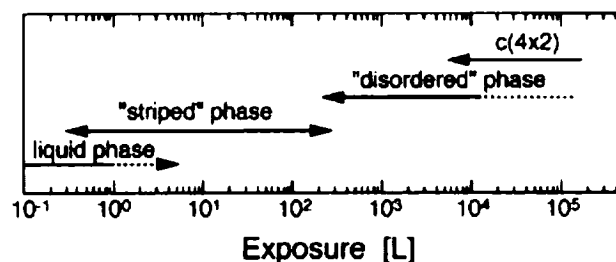


Figure 5.3: Overview [132] of the growth process of hexanethiol SAMs on Au(111) as a function of exposure.

In a recent review paper, Schwartz [87] lists several factors that influence the growth kinetics of alkanethiol SAMs. Gold substrate morphology and cleanliness, analyte concentration and purity, and temperature are but a few of the many factors that need to be controlled if experimental reproducibility is to be achieved. Schwartz highlights the large level of variability observed between experiments, especially for those performed in different laboratories. For example, he compiled the time constants associated with the formation of alkanethiol SAMs as a function of concentration acquired by various authors

using various experimental techniques. He observed a discrepancy of up to two orders of magnitudes in these reported time constants at any given concentration. It is becoming clear that different experimental techniques used to analyze the formation of alkanethiol SAMs yield different information that can be difficult to interpret and to correlate with existing studies. It is problematic to establish which part of the growth process (formation of the lying-down phase, transition into the standing-up phase, or a combination of the two) is being observed in traditional studies involving surface plasmon resonance (SPR), quartz crystal microbalance (QCM), or spectroscopic measurements [135,136,137]. These issues highlight the need to use complementary experimental tools in monitoring the formation process of these SAMs. Furthermore, the combination of two or more experimental tools used simultaneously and *in situ* is essential in accurately investigating the mechanisms involved during self-assembly. Although it is clear that the kinetics of alkanethiol SAM formation will be slightly different whether it is formed from solution or from the vapor phase, this work will focus on formation from the vapor phase.

### **5.3 Surface Stress of Alkanethiol Self-Assembled Monolayers**

A compressive change in surface stress is induced during the formation of alkanethiol SAMs on gold. This surface stress can be quantitatively measured as a cantilever deflection when the SAM is formed on a gold-coated cantilever beam. The experiments described below are used to identify the factors that influence alkanethiol SAM formation and the induced surface stress [138]. Furthermore, the issues that influence the sensor's reproducibility are evaluated.

### 5.3.1 Effect of Gold Surface Morphology

The combined cantilever-based surface stress sensor and ellipsometer setup was used to monitor the growth kinetics of dodecanethiol SAMs. Simultaneous *in situ* surface stress and thickness measurements were carried out in real-time for SAMs grown on both large- ( $600 \pm 400$  nm) and small- ( $90 \pm 50$  nm) grained gold, as described in *Section 3.4: Sample Preparation*. Figure 5.4 shows the real-time average thickness profiles of the dodecanethiol SAMs grown on the two types of gold. Both thickness profiles are similar, showing that a final average SAM thickness measurement of  $1.5 \pm 0.1$  nm is attained within approximately 120 minutes. Ellipsometry therefore does not suggest that there are any significant differences in SAM growth on the two types of gold surfaces in terms of adsorption kinetics or final monolayer structure. In addition, these ellipsometric results do not show clear evidence of a multistep SAM formation process due to the existence of different structural phase transitions.

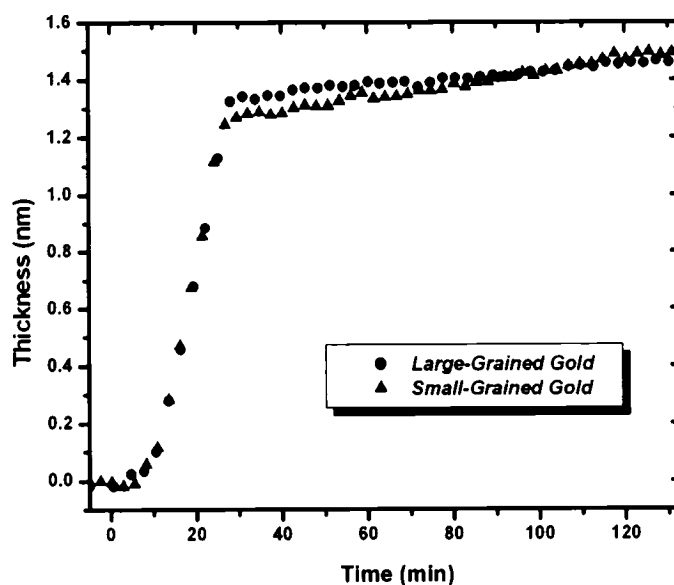


**Figure 5.4:** Real-time ellipsometric thickness profiles of the dodecanethiol SAMs grown small- ( $90 \pm 50$  nm) and large- ( $600 \pm 400$  nm) grained gold. Dodecanethiol was introduced at time  $t = 0$  min.

However, simultaneous surface stress measurements reveal that the SAMs grown on these two gold surfaces are in fact very different, as shown in Figure 5.5A. The deflection signals of the reference cantilevers (not shown) show negligible deflection when exposed to dodecanethiol vapor, as compared to the measured deflections of the active cantilevers. The surface stress curves shown here are thus due only to the surface stress induced by SAM formation. In Figure 5.5, SAM growth on both the small- and large-grained gold exhibits an initial rapid increase in surface stress, reaching a value of approximately  $-0.5$  N/m after 2.5 minutes (Figure 5.5B). This initial increase in surface stress is more rapid for the large-grained gold, and a slightly larger surface stress is measured at this time. The long-term evolution of the surface stress is markedly different for the two systems shown in Figure 5.5A. The surface stress on the large-grained gold continues to increase for approximately 10 hours, reaching a final value of approximately  $-16$  N/m, while the small-grained gold exhibits only a slight increase in surface stress, reaching a final value of approximately  $-0.5$  N/m in minutes. *Ex situ* STM was used to image the resulting SAMs formed on both the small- and large-grained gold surfaces to probe the origins of this puzzling difference between the ellipsometric and surface stress time profiles.

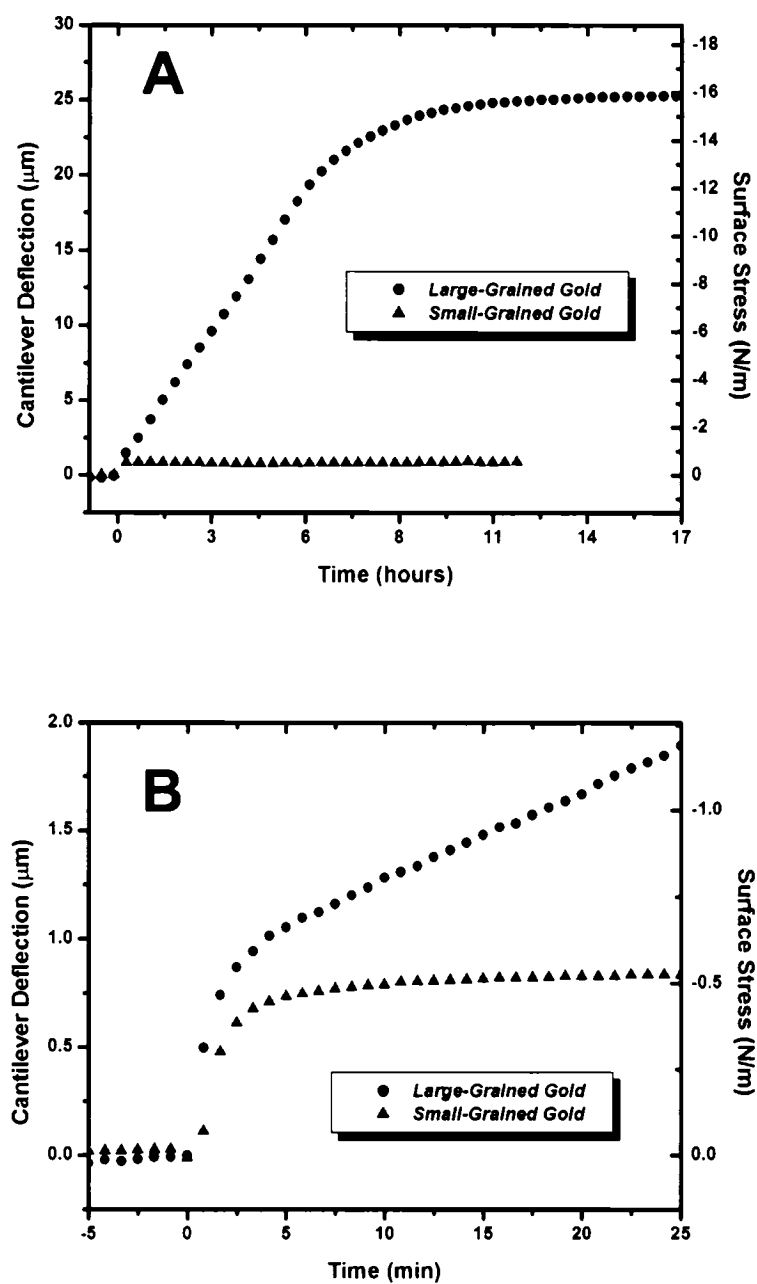


**Figure 5.5:** The surface stress induced during the formation of a dodecanethiol SAM on gold-coated cantilevers. (A) The SAM grown on large-grained gold results in a long-term increase in surface stress, which is not observed for SAM growth on small-grained gold. Dodecanethiol was introduced at time  $t = 0$  hours. The first 25 minutes of SAM formation are shown in (B).

*Ex situ* STM imaging was performed in air on the SAMs that were formed in the sensor's cell during the surface stress experiments. Although a survey of the entire gold surface was not possible, it was found that the SAM resulting from adsorption onto the large-grained gold is fully in a standing-up phase, as revealed in the  $44.7 \times 44.7$  nm STM image of Figure 5.6A. The  $(\sqrt{3} \times \sqrt{3}) R30^\circ$  structure and its  $c(4 \times 2)$  superlattice are observed in several adjacent domains, typical of high-quality SAM in the standing-up phase. The periodicities of these lattices were confirmed by taking a FFT (not shown) of the different SAM domains found in the image. The dark features found (Figure 5.6) are etch pits, which commonly result from alkanethiol adsorption on gold [121]. Figure 5.6B is a magnified view of the boxed region of Figure 5.6A, clearly showing the  $c(4 \times 2)$  superlattice of the  $(\sqrt{3} \times \sqrt{3}) R30^\circ$  lattice. The equivalent primitive unit cell of the superlattice,  $p(3 \times 2\sqrt{3})$ , is also outlined.

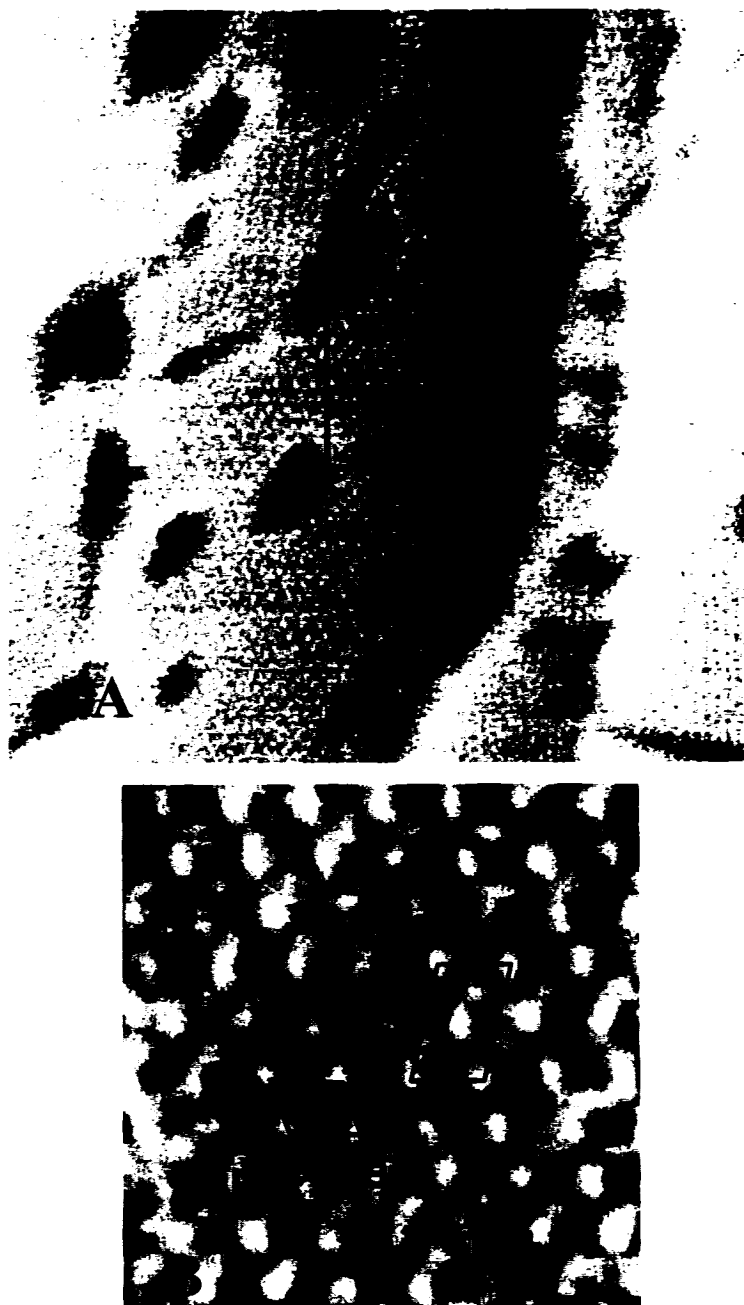


**Figure 5.6:** STM image ( $44.7 \text{ nm} \times 44.7 \text{ nm}$ ) of a dodecanethiol SAM formed on large-grained gold (A). All alkanethiol domains present in (A) are in the standing-up phase. The middle domains clearly exhibit the  $c(4 \times 2)$  superlattice of the  $(\sqrt{3} \times \sqrt{3})R30^\circ$  lattice. The domains in the upper left and on the right of the image show the  $(\sqrt{3} \times \sqrt{3})R30^\circ$  configuration. A zoom ( $7.9 \text{ nm} \times 7.9 \text{ nm}$ ) of part of the middle domain (boxed region) is shown in (B) revealing the  $c(4 \times 2)$  superlattice. The equivalent  $p(3 \times 2\sqrt{3})$  primitive unit cell ( $0.85 \text{ nm} \times 1.01 \text{ nm}$ ) is also shown. The STM tip bias was 600 mV, and the current was kept constant at 25 pA. The image was acquired in ambient air.

The SAM formed on the small-grained gold surface does not have the same high-quality characteristics as the SAM grown on large-grained gold. Figure 5.7 is a STM image of the SAM formed on small-grained gold. In this case, alkanethiol domains of the lying-down striped phase co-exist with domains of the standing-up phase. Although the standing-up phase is observed in a few domains, a broad survey of the SAM-covered surface reveals that the lying-down phase is predominant. The spacing between the lying-down stripes is approximately 1.5 nm, consistent with a lying-down phase where the alkyl chains of the molecules in adjacent stripes (rows) form an interdigitated bilayer on the gold surface [82]. The result is a stacked lying-down phase. The average ellipsometric thickness for this situation is measured to be  $1.5 \pm 0.1$  nm, as shown in Figure 5.4. It is interesting to note that although STM shows that this SAM is composed of a mixture of domains in both the stacked lying-down and standing-up phase, a thickness of 1.5 nm also corresponds to the expected [139] and measured thickness of the fully standing-up dodecanethiol SAM. STM reveals the differences in the resulting SAM structure for formation on small- and large-grained gold, whereas the ellipsometric profiles of Figure 5.4 alone are insufficient for distinguishing the two cases.



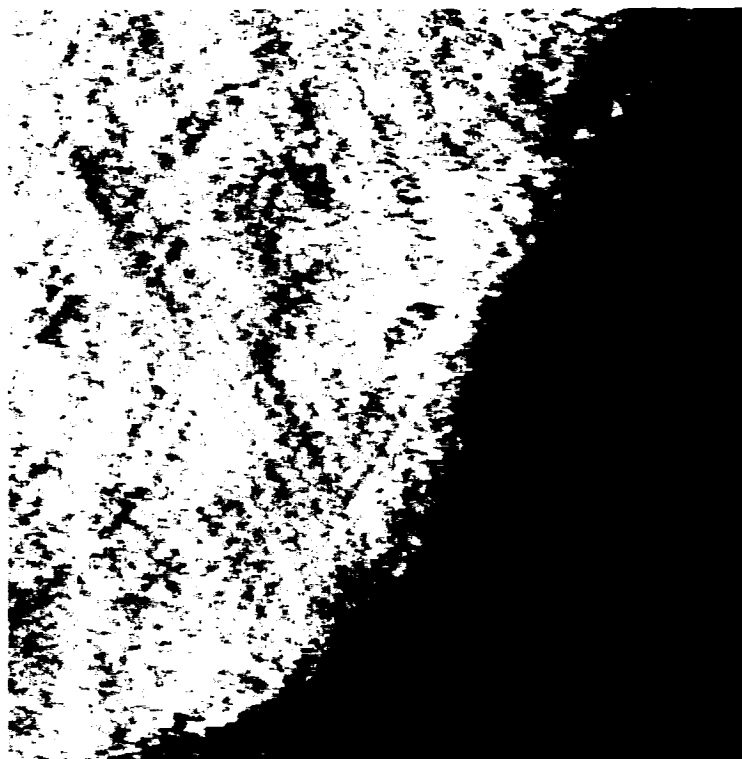


**Figure 5.7:** STM image ( $24.5 \text{ nm} \times 24.5 \text{ nm}$ ) of mixed phases of a dodecanethiol SAM grown on small-grained gold. The domain on the left side of the image exhibits a periodicity of  $0.5 \text{ nm}$ , indicating that the SAM is in the  $(\sqrt{3} \times \sqrt{3})R30^\circ$  standing-up phase. The larger stripes on the lower right side of the image are spaced by  $1.5 \text{ nm}$ , typical of a stacked lying-down phase. The STM tip bias was  $600 \text{ mV}$ , and the current was kept constant at  $25 \text{ pA}$ . The image was acquired in ambient air.

These STM data thus help to resolve the origin of what appears to be very different time courses of ellipsometric thickness and surface stress data. Ellipsometry fails to differentiate SAM growth on the two types of gold morphologies, whereas the evolution of the induced surface stress shows very different behaviors for the two systems. Single wavelength ellipsometry of course has limitations in making definitive assignment of thickness. Firstly, variations in the film's index of refraction from the bulk value during the self-assembly process can lead to a systematic error in thickness values, especially at low coverage. The different molecular orientations of the low-coverage lying-down phases, and the high-coverage standing-up phase can lead to non-negligible variations in film index of refraction leading to errors in thickness readings. Secondly, the

measured thickness value is a weighted average of the thickness of the different phases (domains) present. This has implications in monolayer thickness determination for growth on small-grained gold because the SAM, being predominantly in the lying-down phase, clearly co-exists with a measurable standing-up component. Any absolute differences between the thicknesses of the lying-down and the standing-up states are therefore averaged in the ellipsometric experiment. These factors make the analysis of ellipsometric measurements highly non-trivial. STM, on the other hand, establishes that there are indeed important differences in the SAM formed on the two types of gold surfaces, and that there is both greater alkanethiol coverage and order on large-grained gold compared to small-grained gold substrates. While ellipsometry can reveal evidence of phase transitions during SAM formation, STM must be used for phase identification. These findings support the assertion that the use of complementary techniques is essential in understanding these self-assembled systems. While some studies report findings based on single-wavelength ellipsometry alone [140], we caution that this tool can lead to misleading results when not corroborated by complementary experimental techniques.

The final surface stress values for the experiments of Figure 5.5 were  $-0.51 \pm 0.02$  N/m and  $-15.9 \pm 0.6$  N/m for SAM formation on small- and large-grained gold, respectively. The uncertainties quoted here arise from the instrumental uncertainty (4%), as discussed in *Section 4.2: Quantifying Surface Stress*. The corresponding STM results strongly suggest that the large surface stress values measured on large-grained gold are due to the formation of highly-ordered dodecanethiol SAMs adopting the  $c(4 \times 2)$  structure. Previous reports of surface stress [11,141] for dodecanethiol SAM formation from the vapor phase are consistent with the results obtained in this study for formation on small-grained gold. The STM images suggest that the SAMs formed on the small-grained gold do not achieve the highly ordered  $c(4 \times 2)$  structure because progression to the requisite full coverage state is inhibited.

### 5.3.2 Features in the Kinetics of SAM Formation

Figure 5.8 show the initial stages of the surface stress profiles for an experiment similar to the one presented in Figure 5.5. The only difference is that SAM growth was slightly slowed down by increasing the separation distance between the injected liquid dodecanethiol droplet and the gold-coated cantilevers, which slows the approach of alkanethiols towards the cantilevers. Consequently, three distinct processes are now clearly resolvable in the surface stress/time profile, which are associated with different stages of SAM formation. These features are also present in the data shown in Figure 5.5, but are less pronounced because of the faster kinetics. These three regions are labeled **A**, **B**, and **C** on Figure 5.8. Region **A** is associated with a initial disordered phase present in the early stages of alkanethiol adsorption. Based on STM imaging, we infer that the process occurring in region **B** is associated with the transitions into the lying-down striped phases. In region **C**, the surface stress imparted on the large-grained gold continues to increase over a long timeframe. This long-term increase in surface stress is related to the transition into the standing-up phase, and its subsequent ordering. In the case of adsorption onto small-grained gold, the surface stress ceases to increase since the SAM remains in a relatively low-coverage state, where the stacked lying-down phase is predominant, but co-exists with a few domains exhibiting the standing-up phase. The time constants associated with these processes are a function of various factors, including gold surface cleanliness and morphology, alkanethiol length, cell geometry, temperature, and alkanethiol vapor concentration. In fact, the time needed for a complete dodecanethiol (C12) SAM to form on large-grained gold surfaces has shown some variability, with completion times ranging from 6 hours to over 48 hours. Nevertheless, the final process (region **C**) seems to have a time constant that is consistently at least two orders of magnitude larger than the first two processes. The features and transitions that appear in the surface stress data are not readily identifiable in the ellipsometric profiles of Figure 5.4. Nevertheless, although the average ellipsometric thickness measurements (e.g. Figure 5.4) did not always

reveal features in a multistep process, they also did not follow simple Langmuir kinetics [142], as found in other ellipsometric, SPR or QCM studies involving alkanethiol SAM formation [135,136,143], suggesting more complex growth kinetics. In fact, the rather complex kinetics (i.e. physisorption, chemisorption, and phase transitions) involved in SAM formation should not conform to Langmuir-type models, simply defined by having the probability of a molecule sticking to the surface being proportional to the available uncovered surface area. Based on simultaneous surface stress measurements, and *ex situ* STM imaging, we infer that the rapid increase (~30 min.) in ellipsometric thickness in the profiles of Figure 5.4 is associated with the formation of the unstacked and stacked lying-down phase. After 30 minutes, ellipsometry fails to identify the differences in SAM structure for formation on the two types of gold.

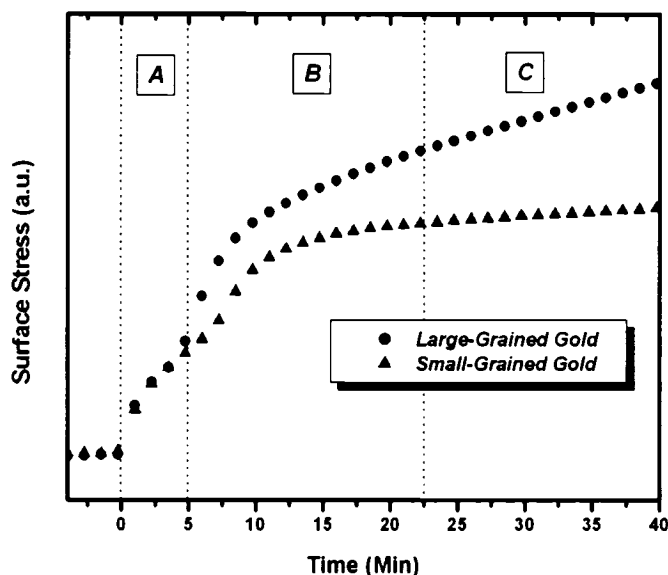


**Figure 5.8:** Initial stages of the surface stress profiles for dodecanethiol adsorption on large- and small-grained gold. The region labeled (A) corresponds to the initial stages of alkanethiol adsorption. Region (B) is associated with the transition into the lying-down phases. In region (C), the transition into the standing-up phase begins for adsorption onto large-grained gold, whereas the SAM remains in a stacked lying-down phase for growth on small-grained gold.

The full conversion into the standing-up phase from the lying-down phase does not occur for SAM growth on small-grained gold as opposed to growth onto gold with larger grains. On small-grained gold, alkanethiol domains of the lying-down phase form, but their growth is inhibited in some fashion, so that a full conversion into the standing-up phase does not occur. We note that the average size of atomically flat areas available for formation of ordered domains (composing the full SAM) on the small-grained gold is of the same order of magnitude as typical domain sizes ( $\sim 10$  nm) that are observed for well-ordered SAMs [115,144]. Some STM studies suggest that it is energetically favorable for nucleation of the standing-up phase to occur at domain boundaries of the lying-down phase, through the so-called disordered phase. We speculate that a certain number of adjacent domains (domain boundaries) of the lying-down phase are required to trigger nucleation of the standing-up phase. On small-grained gold, such nucleation sites are scarce, and the SAM remains in a kinetic trap, unable to promote the formation of the standing-up phase. We stress here that the mechanisms detailing the interplay between gold grain size and phase transitions are complex, and remain to be fully understood.

### 5.3.3 Diffusion Effect on SAM Formation

The alkanethiol vapor concentration in the early stages of SAM formation also has a strong influence on SAM growth. Alkanethiol SAM formation from the vapor phase was carried out similarly to the experiments described above, by injecting dodecanethiol in pure liquid form at a specific location in a sealed cell containing the cantilevers. This liquid droplet gradually evaporates, and the vapor concentration gradually increases in the vicinity of the gold-coated cantilevers, and eventually reaches saturation. The difference here is that the volume and the distance between the liquid alkanethiol droplet and the gold-coated cantilevers were varied using cylindrical volumetric extensions, as described in *Section 3.1.5*:

*Cell Volume and Alkanethiol Vapor Diffusion.* In the following set of experiments, 150  $\mu\text{l}$  of pure liquid dodecanethiol was injected into the closed cell. It should be noted that varying the volume of liquid alkanethiol injected into the cell did not affect the observed surface stress curves, as long as sufficient liquid was injected such that some remained in the cell when the vapor reached saturation concentration. The time constant associated with this increase in concentration up to saturation is proportional to the square of the separation distance between the alkanethiol droplet and the cantilevers, also shown in *Section 3.1.5*. As the SAM forms on the gold-coated cantilevers, the induced surface stress is measured as a function of time for different droplet/cantilever distances and cell volumes. This set of experiments was conducted using small-grained gold.

Figure 5.9 is a graph showing the induced surface stress profiles for alkanethiol droplet-to-cantilever distances of 3 mm, 23 mm, 96 mm, and 246 mm, corresponding to cell volumes of 3 ml, 3 ml, 12 ml, and 32 ml, respectively. It should be noted that the shape of the surface stress profiles is quite different for distances of 3 mm and 23 mm, although the volumes are the same. These experiments were performed in the same cell, but the dodecanethiol droplet was injected at different locations in the cell. These results clearly indicate that SAM formation is strongly influenced by the vapor concentration in the early stages of exposure, both qualitatively and quantitatively. We observe that the surface stress curves exhibit a stress release (i.e. the surface stress signal decreases) for large droplet-to-cantilever distances. Although these curves (with surface stress release) initially reach a maximum in surface stress that is larger than the equilibrium surface stress reached in the case of the short droplet-to-cantilever distance (3 mm), the surface stress decreases and ends up being smaller. The time at which the surface stress just starts to increase was found to be proportional to the square of the alkanethiol droplet-to-cantilever distance. This is expected since the diffusion time constant of the alkanethiol vapor in the cell also increases as the square of this distance; the onset of SAM formation is necessarily vapor

diffusion-limited. The times at which the maxima in the surface stress curves occur (for droplet-to-cantilever distance of 23, 96, and 246 mm) were also plotted as a function of this distance (graph not shown). In this case, the relationship is no longer to the second power, but approximately linear (power of 1.1). At this stage of formation, self-assembly is not only vapor diffusion-limited, but the complex mechanisms driving self-assembly (varying sticking coefficient, ordering of monolayer, etc.) also come into play. Alkanethiol SAM formation does proceed at low vapor concentrations, albeit at a slower rate than in the presence of a higher concentration.

The structure of the resulting SAMs formed in the cases where a surface stress release was observed could not be assessed by STM due to difficulties in achieving molecular resolution. In these cases, ellipsometry reveals that the resultant SAM attains only partial monolayer coverage. Figure 5.10 shows that the final average thickness reaches  $0.7 \pm 0.1$  nm, instead of the  $1.5 \pm 0.1$  nm previously associated with either that expected for a fully standing-up, or a stacked lying-down SAM. Since this smaller thickness does not correspond to what was measured for neither the standing-up or the stacked lying-down phases, we infer that a measured thickness of  $0.7 \pm 0.1$  nm is consistent with dodecanethiol adsorption leading to a lying-down phase whose alkyl chains are not stacked. [82,145] The thickness of an unstacked lying-down domain previously measured by AFM ( $0.50 \pm 0.05$  nm) [145] is in the same range (although smaller) as the  $0.7 \pm 0.1$  nm average thickness measured here using ellipsometry. Notwithstanding the caveats surrounding the ellipsometric thickness values (i.e. *Section 5.3.1*), the requisite compressive load of the tip in the AFM experiment introduces another type of uncertainty, perhaps underestimating the thickness.

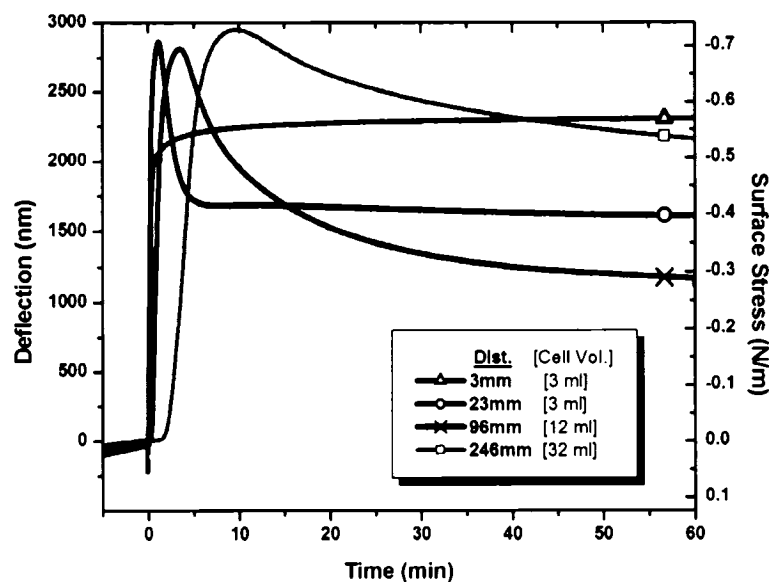


Figure 5.9: Surface stress profiles for various dodecanethiol droplet-to-cantilever distances. For distances of 23 mm or greater, a stress release is observed, and the final average SAM thickness reaches  $0.7 \pm 0.1$  nm.

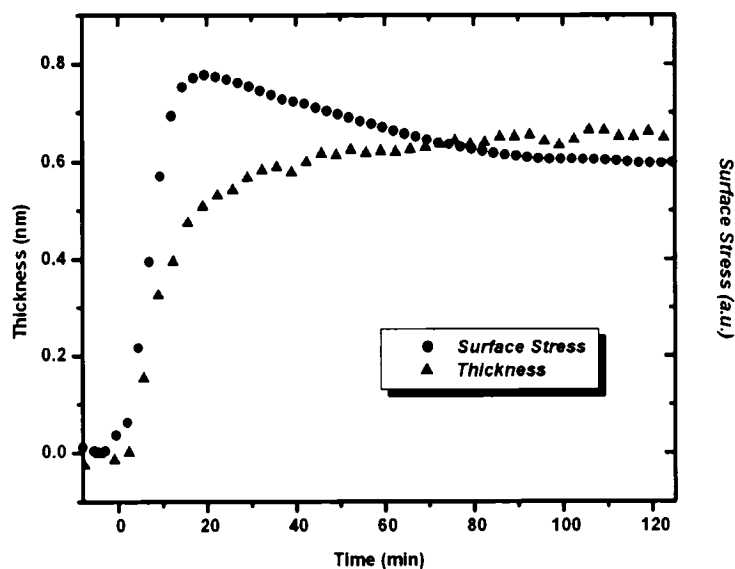


Figure 5.10: Simultaneous surface stress and ellipsometric thickness measurements of a dodecanethiol SAM grown with an initially low vapor concentration. The surface stress curve exhibits a stress release, while the ellipsometric thickness monotonically increases, attaining an eventual value of  $0.7 \pm 0.1$  nm.



The resultant structure of a SAM grown on small-grained gold is not only a function of the gold's morphology, but also depends on the growth rate. For rapid growth rates on small-grained gold, STM imaging indicates that the predominant final phase is a stacked lying-down phase. For slow growth rates, ellipsometry suggests that the SAM remains in an unstacked lying-down phase. The surface stress results are consistent with this interpretation, as the final surface stress value measured under conditions of slow growth (unstacked lying-down phase; surface stress release) is typically smaller than the final surface stress value measured in the rapid growth regime (stacked lying-down phase; no surface stress release). In fact, one would indeed expect that the induced surface stress would be larger for systems whose molecular density is higher, although the induced surface stress is not necessarily directly proportional to the number of alkanethiol molecules on the gold surface forming the SAM. In fact, the molecular density of the standing-up phase is three times larger than that of the stacked lying-down phase. Nevertheless, the measured surface stress of the standing-up phase is much more than three times that of the stacked lying-down phase, as shown in Figure 5.5.

The above findings are consistent with the hypothesis that molecular adsorption can slow to the point that the unstacked lying-down domains achieve an energetically metastable state. Schreiber [114] postulates that such a kinetically trapped state is more prevalent for SAM formation from the vapor phase than from solution. For rapid growth, this intermediate state is not as stable, and the transition of this metastable state into a denser, stacked lying-down phase is possible. This suggests that the intermediate phases occurring during growth attain different levels of stability (and quality) depending on growth rate, and that some intermediate states might be skipped altogether for very rapid growth.

### 5.3.4 Aging of Gold Substrate

A certain level of gold surface contamination is inevitable when conducting experiments under ambient air conditions. In our case, the gold-coated cantilevers are exposed to ambient laboratory air while they are transferred from the thermal evaporator's vacuum to the closed cell. This exposure to air contaminates the gold surface, which affects the self-assembly of alkanethiols onto the gold-coated cantilevers. It is believed that the alkanethiols' relatively high affinity for gold is enough to successfully displace weakly bound contaminants from the gold surface as the SAM is formed [143]. Figure 5.11 is a graph of various surface stress profiles for dodecanethiol adsorption onto small-grained gold-coated cantilevers that have been exposed to ambient laboratory air for various amounts of time, as indicated on the various curves. The experiments here were conducted in a cell with a volume of 3 ml and a dodecanethiol droplet-to-cantilever distance of 23 mm (see Figure 5.9). In this example, the goal is not to extract information about the processes guiding the displacement of these contaminants, but to point out that surface contamination indeed has an effect on the measured surface stress induced during SAM formation. The profiles of Figure 5.11 are qualitatively similar, but the surface stresses observed at both the peak, and at the end of the experiment are consistently lower with increasing exposure to air prior to being exposed to dodecanethiol. In the case of the curve labeled '*7 days*', the gold surface was exposed to ambient air for 7 days prior to exposure to dodecanethiol. In this case, a smaller surface stress is induced, and the curve does not exhibit any release in surface stress, perhaps an indication that the SAM does not even attain the unstacked lying-down phase. From Figure 5.11, we find that the contaminants become more difficult to displace by incoming alkanethiols with increased exposure to air, as indicated by the reduction of the final surface stress values achieved.

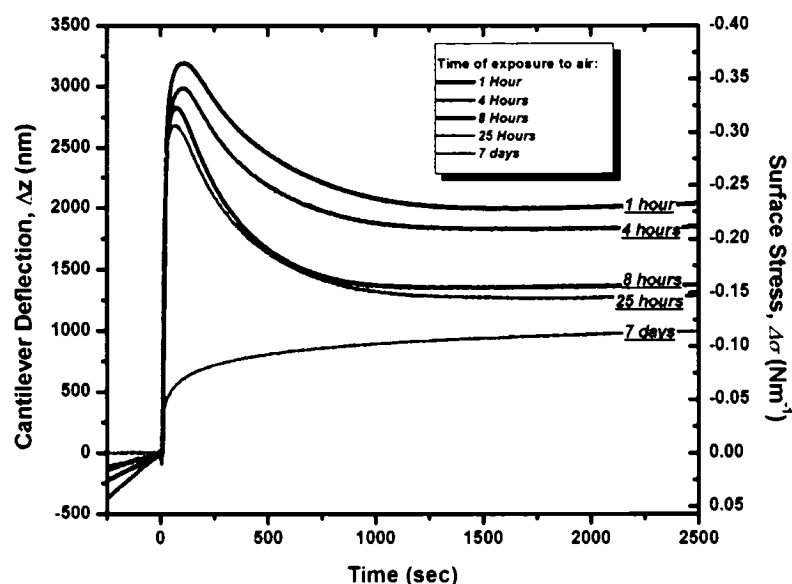


**Figure 5.11: Surface stress profiles for dodecanethiol SAM formation on gold contaminated by exposure to ambient air. The various surface stress profiles were acquired under identical experimental conditions, except for the fact that the gold-coated cantilevers were exposed to ambient air for various lengths of time prior to dodecanethiol exposure. Dodecanethiol was injected at time  $t = 0$  sec.**

X-ray Photoelectron Spectroscopy (XPS) performed on the gold surfaces having been exposed to ambient laboratory air for 3 hours up to 7 days revealed the presence of contamination species of carbon and oxygen. Cleaning the gold surface by sputtering eliminated these contamination peaks, revealing clean gold. This indicated that the detected contamination was limited to the surface, rather than contamination present in the whole gold layer, again consistent with the results of Figure 5.11.

### 5.3.5 Sensor Drift

Cantilever-based sensors are not immune to signal drift. The cantilever deflection signal can drift for several hours or days in the case of a sensor with a freshly

deposited gold film. Possible contributors to this drifting are an induced surface stress due to the adsorption of surface contaminants onto the gold-coated cantilever surface, relaxation of the gold layer itself following deposition, electronic drift, and heating of the cantilever by the deflection sensing laser.

The graph shown in Figure 5.11 shows the presence of this sensor drift prior to dodecanethiol injection at time  $t = 0$  sec. In fact, this signal drift can be large, on the order of  $10^{-4} \text{ Nm}^{-1}\text{s}^{-1}$ . Laser heating of the cantilever can be ruled out here as the major source of signal drift, since the older gold-coated cantilever (labeled '7 days') does not exhibit any drift prior to injection. If thermal bending due to the bimetallic effect were uniquely responsible for drift, this older cantilever would also experience drift. Even when using the temperature controller to maintain the cantilever temperature constant to within  $0.02^\circ\text{C}$ , signal drift is still present for cantilevers having a freshly-evaporated gold receptive layer. Drift resulting from gold film relaxation following deposition was also ruled out by allowing the gold films to relax in the evaporator's vacuum for different amounts of time. Although the drift was greater for freshly evaporated gold films (left in vacuum for less than 2 hours after evaporation), film relaxation was ruled out as the major source of drift. In fact, we found that the drift was consistent as long as the gold film was left to relax for at least 6 hours post-evaporation. This was done for all the experiments described herein. Electronic drift was also ruled out by leaving all electronics (deflection sensing, laser, acquisition card) powered for hours, and thus thermally equilibrated, prior to the start of an experiment. We find sensor drift to be caused by the surface stress induced during gold surface contamination based on the above. In addition, the surface stress profiles of Figure 5.11 show that despite significant differences in drift prior to dodecanethiol injection, all profiles find equilibrium after at 2000 seconds, showing that the surface-contamination-driven drift becomes negligible after exposure to alkanethiols. The presence of even a partial alkanethiol SAM acts as a barrier, protecting the gold surface from non-specific contamination. In order to minimize the effects of

surface contamination on the signal of interest, all experiments were performed on gold-coated cantilevers within an hour of being taken out of the evaporator.

#### **5.4 Summary and Implications on Cantilever-Based Sensors**

The experiments described in this chapter were aimed at identifying some factors that influence the formation of alkanethiol SAMs. It was found that the morphology of the gold substrate has a significant impact on SAM formation, affecting the structure of the resulting monolayer. This information is important not only in understanding the mechanisms that drive the self-assembly process of alkanethiol monolayers, but also for the design of future sensors that utilize these SAMs as the main receptive layer. These experiments also revealed that the use of complementary experimental techniques is essential in understanding these systems. Particularly, it was shown that single-wavelength ellipsometry can lead to very misleading results if not used in conjunction with other techniques. We have also shown that analyte diffusion and concentration can have a dramatic effect on sensor response. The influence of gold surface cleanliness on SAM formation was also investigated, and shown to have an equally substantial effect.

Chemically active, functionalized SAMs on gold-coated cantilevers are a promising architecture for cantilever-based sensors. The results shown in this chapter have lead to findings important to the cantilever-based sensing community. We have shown that SAM quality, and thus sensor sensitivity can greatly increase as a function of the underlying substrate morphology. Controlling the quality of the SAMs used as receptive layer is crucial in designing effective sensors. Therefore, it will be very important to develop methods to form atomically flat Au(111) on silicon or silicon nitride cantilevers. Also, we have shown that environmental conditions (such as analyte concentration and diffusion,

substrate cleanliness...) will have to be controlled in order to achieve reliable and reproducible results.

## 6 Origins of Surface Stress

### 6.1 Motivation

The origin of the measured surface stress induced during the formation of alkanethiol SAMs on gold-coated cantilevers remains a key question in the literature [11,43,44]. An understanding of the mechanisms responsible for this surface stress has implications not only in the development of various cantilever-based sensors, but also holds importance in the engineering of nanoscale structures. Scientists are seeking to build structures using the bottom-up approach, a key characteristic of nanotechnology. One approach involves using chemical self-assembly as the driving force in creating nanoscale structures, while controlling growth conditions including using stress engineering as a tool to tailor these structures to the desired outcome.

Alkanethiol self-assembly is one of the most extensively studied self-assembled systems due to the stability of the resulting SAMs, and to their relatively simple chemical composition. But studies into the origins of the induced surface stress remain scarce. Berger *et al* [11] first measured the surface stress induced by the formation of alkanethiol SAMs on gold, and found that the measured surface stress increased with molecular chain length. This chain length dependence was attributed to an increase in the net dipole moment of the alkanethiol molecule (when adsorbed to a gold surface) for increasing molecular chain length. The SAM being fully-formed, the parallel alkanethiol molecules would reportedly repel each other resulting in a measurable compressive surface stress.

However, the results of *Section 5.3.1 (Effect of Gold Surface Morphology)* suggest that the surface stress results found by Berger *et al* [11] are for SAM formation on small-grained gold surfaces, where the resulting SAM is composed of a mixture of structural phases, but predominantly in the lying-down phase. The interpretation that the surface stress originates from electronic dipole repulsion between adjacent alkyl chains in a fully formed SAM should be re-examined with this in mind.

This chapter seeks to establish both the molecular chain length dependence, and the effect of the gold grain size on the measured surface stress. Several possible mechanisms will be examined as possible origins of the induced surface stress, and will be compared to experimental results.

## **6.2 Chain Length Independence of Surface Stress**

The surface stress resulting from alkanethiol SAM formation was measured as a function of molecular chain length. Hexanethiol (C6), octanethiol (C8) and decanethiol (C10) SAMs were investigated. Figure 6.1 shows the mean equilibrium surface stress values measured as a function of alkanethiol chain length.

No chain length dependence was found for these three alkanethiol lengths. In all these cases, the gold surfaces had an average grain size of  $500 \pm 400$  nm as assessed by STM imaging. Dodecanethiol (C12) was not included here as the evolution of surface stress profiles for this chain length on this type of gold was typically too slow ( $> 24$  hours); the surface stress often never reach equilibrium (even after 48 hours). The error bars are the standard errors associated with the number of experiments performed for each chain length (3 for C6, 4 for C8 and 11 for C10). A total of 18 experiments are included in Figure 6.1, which show a constant overall mean surface stress of  $-6.3 \pm 0.2$  N/m. Although the instrument



is capable of much greater precision (see *Section 4.3: Instrument Sensitivity and Resolution*), the larger error bars associated with each chain length indicate that the surface stress induced by the formation of alkanethiol SAMs is still considerably variable despite careful control over the factors (temperature, alkanethiol purity, gold surface morphology, etc.) that influence self-assembly. It should be pointed out that the gold surface grain size was not assessed for gold surfaces used in each experiment. Similar evaporation conditions were used in producing the gold surfaces for all these experiments, thus ensuring a consistent gold morphology from experiment to experiment. Nevertheless, small variations in gold grain size could result from slight differences in evaporation conditions, thus yielding some variability in the measured surface stress from one experiment to the next. Any model that seeks to explain the origin of the surface stress should not only consider the lack of chain length dependence, but this variability as well.

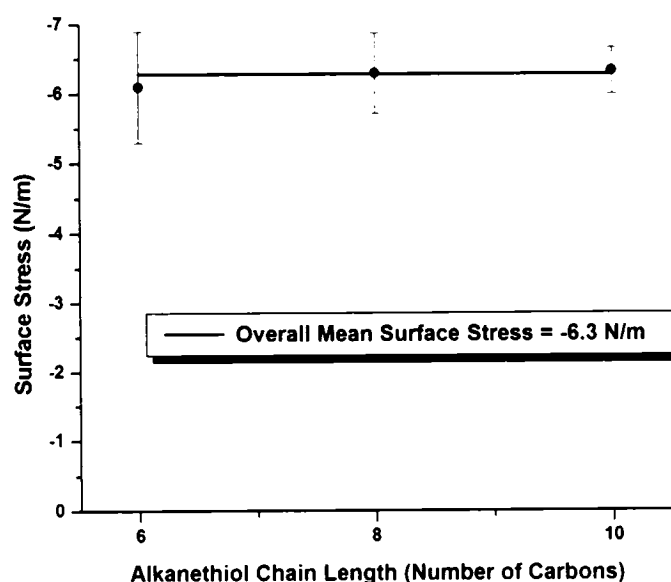


**Figure 6.1:** The mean surface stress resulting from hexanethiol (C6), octanethiol (C8) and decanethiol (C10) SAM formation on gold-coated cantilevers. The gold substrate used in these experiments had grain sizes of  $500 \pm 400$  nm.

### 6.3 Gold Grain Size Effects on Surface Stress

The influence of the gold substrate's morphology on the measured surface stress was investigated for octanethiol SAM formation on gold-coated cantilevers. Gold surface with various grain sizes were produced by thermal evaporation, as described in *Section 3.4: Sample Preparation*, with the exception that the substrate (cantilever) temperature was set to various values (between 100°C and 260°C) prior to the start of the evaporation, and different thicknesses of gold films were produced (50 nm or 100 nm). Figure 6.2 shows a graph of the induced surface stress as a function of the gold substrate's average grain area (square of the grain size). These experiments were conducted in the 3 ml cell with an octanethiol droplet-to-cantilever distance of 3 mm, as defined in *Section 5.3.3: Diffusion Effect on SAM Formation* (Figure 5.9). The surface stress increases linearly with the average gold grain area, following the empirical relationship:

$$\sigma = (-0.2 \pm 0.2 \text{ Nm}^{-1}) + ((-2.5 \pm 0.2) \times 10^{-5} \text{ Nm}^{-1} \text{ nm}^{-2}) * \text{Grainsize}^2 \quad \text{Equation 6.1}$$

Based on the result of *Section 5.3.1: Effect of Gold Surface Morphology*, it is expected that there should be a critical grain size at which the SAM can undergo the transition from the lying-down phase into the standing-up phase. Below this critical grain size, the SAM remains in the metastable lying-down phase. The data of Figure 6.2 do not show clear evidence of a critical grain size at which this transition into the standing-up phase is allowed. However, different structural phases can co-exist in adjacent domains forming a SAM, as is evident from Figure 5.7, where the SAM formed on small-grained gold was found to be predominantly in the lying-down phase, but co-existed with a very small number of standing-up domains. Because of the large variability of grain sizes for a given sample, as evident from the large standard deviations quoted with average grain sizes (i.e.  $600 \pm 400$  nm for large-grained gold), it is expected that some grains are

too small to allow the transition into the standing-up phase, even for so-called large-grained gold. For intermediate grain sizes (between small- ( $90 \pm 50$  nm) and large- ( $600 \pm 400$  nm) grained gold), we expect that monolayer formation results in a SAM composed of a mixture of lying-down and standing-up domains. As the average gold grain size increases, a greater area is covered by standing-up domains as compared to that covered by lying-down domains. The grain size data of Figure 6.2 suggests that as the gold grain size increases, the areal ratio of standing-up to lying-down domains also increases, resulting in an increased measured surface stress.

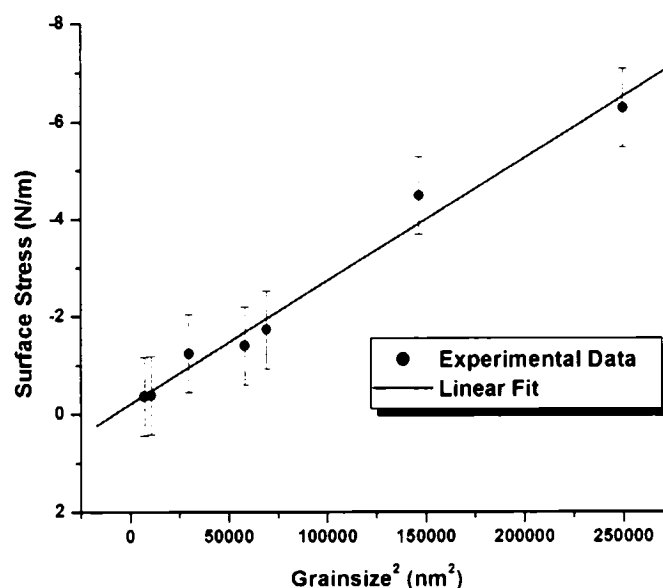


**Figure 6.2:** The surface stress induced by octanethiol SAM formation as a function of the square of the gold substrate grain size. The data is fitted with a linear relationship of the form  $y = (-0.2 \pm 0.2 \text{ Nm}^{-1}) + (-2.5 \pm 0.2 \times 10^{-5} \text{ Nm}^{-1} \text{ nm}^{-2}) * x$ . The standard deviations of the grain sizes are not shown.

The maximum theoretical surface stress induced by the formation of an alkanethiol SAM on gold remains to be determined. The result of Figure 6.2 does not yield this maximum value, but rather yields a lower bound in the maximum theoretical surface stress. Since the critical gold grain size at which the transition into the standing-up phase occurs is not known, it is difficult to extrapolate what

this maximum theoretical surface stress value might be. Nevertheless, these data do yield a lower bound for the theoretical surface stress induced by a perfect SAM on a perfect surface. It is assumed that the theoretical surface stress value is close to the value measured in the case of large-grained gold (Figure 5.5), of approximately -16 N/m.

## **6.4 Modeling**

The origin of the induced surface stress at the molecular level is not known. Many driving forces are involved in the formation of alkanethiol SAMs, all of which can contribute to the overall observed surface stress. Inter-molecular interactions between adsorbed species are often cited as the main mechanism in the development of the induced surface stress [16,22,146]. Electrostatic repulsion between adsorbed molecules can arise from the electronic redistribution that occurs as a result of adsorption onto the surface. Modification of the underlying gold substrate's electronic structure due to adsorption also has to be considered as a mechanism responsible for the development of the induced surface stress. With this in mind, modeling of the molecular origins of the surface stress was undertaken. Several models were considered in parallel to the experimental results discussed above.

### **6.4.1 Chain-Chain Interactions: Van der Waals**

Inter-molecular Lennard-Jones (van der Waals) -type interactions provide a simple mechanism that could account for the measured surface stress due to molecular adsorption. In order to assess the contribution of these interactions to the overall induced surface stress in the case of alkanethiol SAM formation, a molecular mechanics approach using the universal force field (UFF) [147] was used to calculate the variations in energy as a function of molecular separation between two adjacent (parallel) alkanethiol molecules. Atomic positions in

individual alkanethiol molecules were optimized by energy minimization using Gaussian98.

Gaussian98 [148,149] is a commercially-available computational chemistry program capable of modeling a variety of different molecular or atomic systems predicting a multitude of properties such as molecular energies, structure, bond energies, molecular orbitals, and atomic charge distribution within a molecule. The atomic positions of the atoms composing an alkanethiol molecule were determined using Gaussian98's optimization feature which uses energy minimization calculations to predict stable molecular conformations. Gaussian98 allows for the use of various different types of calculations depending on the system under investigation. In this case, we have used a Restricted Hartree-Fock (RHF) calculation using the 6-31G(d) basis set in structure optimization mode [150]. Figure 6.3 shows a decanethiol molecule after optimization by Gaussian98. Although Gaussian98 is in principle capable of yielding metastable structures (local energy minima), we accept that this structure is the lowest energy, and therefore most likely structure for decanethiol based on comparison to expected molecular and individual bond lengths [76] and based on symmetry.

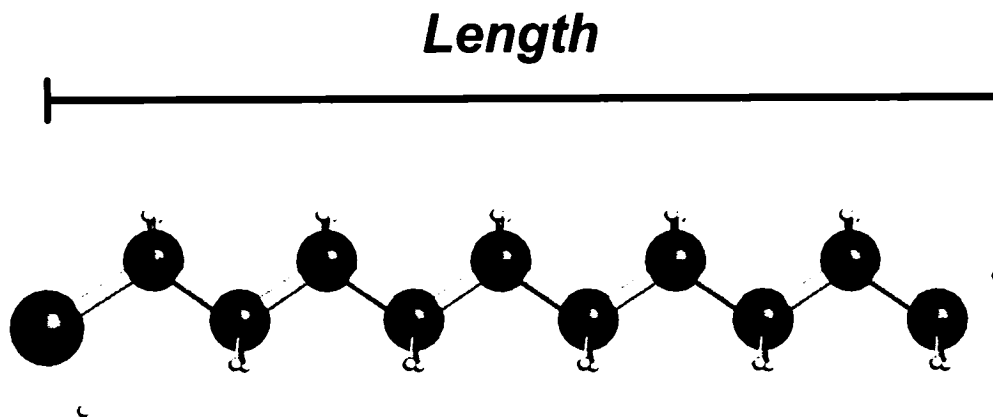


**Figure 6.3:** The relative atomic positions composing a decanethiol molecule as calculated using Gaussian98. The calculated length (distance between the sulfur atom and the furthest hydrogen atom) of decanethiol is 1.39 nm.

The Lennard-Jones interaction energies between two adjacent alkanethiol molecular chains were calculated as a function of inter-molecular separation using the parameters in the universal force field (UFF). A Lennard-Jones (6-12) type expression was used to evaluate the non-bonded interactions (van der Waals forces) between two parallel decanethiol molecules. The energy,  $E_{vdw}$ , between two atoms (i and j) predicted by the UFF approach takes the form [147]:

$$E_{vdw} = D_{ij} \left\{ -2 \left[ \frac{x_{ij}}{x} \right]^6 + \left[ \frac{x_{ij}}{x} \right]^{12} \right\} \quad \text{Equation 6.2}$$

where  $D_{ij}$  is the well depth and  $x_{ij}$  is the van der Waals bond length, and  $x$  is the distance between the two atoms belonging to each molecule. These parameters are published [147].

Figure 6.4 shows the Lennard-Jones energy contribution as a function of inter-molecular separation for two parallel decanethiol molecules. The summation of the energy terms (Equation 6.2) is for atomic pairs between the two molecules, and not within a molecule. The energy contribution within a molecule would simply add a constant term to the total energy values since the relative atomic positions within the molecules are kept fixed. The equilibrium inter-molecular separation, given by the minimum in energy of Figure 6.4, is unaffected by this constant term. An equilibrium separation distance of 0.47 nm is found for two parallel decanethiol molecules.

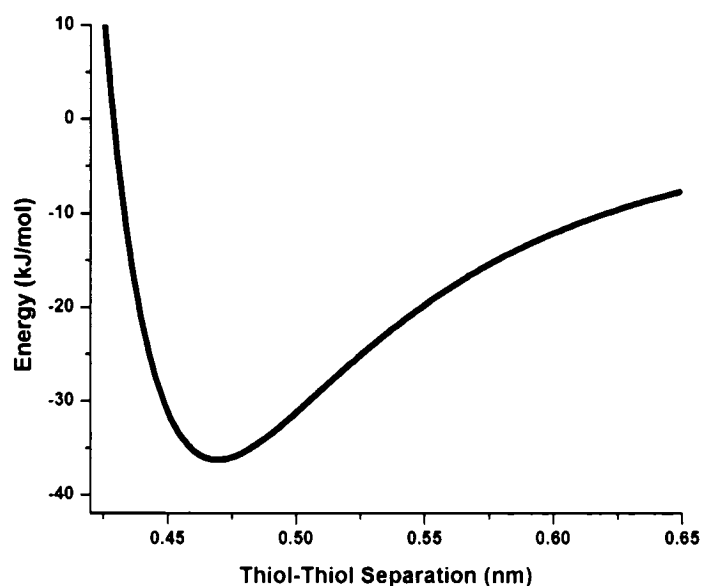


**Figure 6.4:** Lennard-Jones energy calculation as a function of separation between two parallel decanethiol molecules. The energy minimum occurs at a separation of 0.47 nm.

The equilibrium hexagonal lattice structure of a high quality decanethiol SAM in the standing-up phase is  $(\sqrt{3} \times \sqrt{3})R30^\circ$ . The inter-molecule distance in a SAM in the standing-up phase is  $\sqrt{3} \times 0.28837 \text{ nm} \approx 0.5 \text{ nm}$  (where 0.28837 nm is the minimum equilibrium inter-atomic distance of bulk gold) [151]. This implies that the equilibrium separation distance of 0.47 nm between two adjacent decanethiol molecules would result in a tensile surface stress if the surface stress were mainly the result of attractive inter-molecular Lennard-Jones interactions. Our measurements show that the actual surface stress induced during the formation of alkanethiol SAMs is always compressive, where the molecules seem to repel each other. This result suggests that the observed compressive surface stress does not result from Lennard-Jones-type interactions between the chain molecules.

A similar calculation was performed for two parallel decane molecules. Again, atomic position optimization within a molecule was performed using Gaussian98. Figure 6.5 shows the energy as a function of separation distance for two decane

molecules. The predicted equilibrium molecular separation, as indicated by the position of the minimum in energy in Figure 6.5, is found to be 0.44 nm.

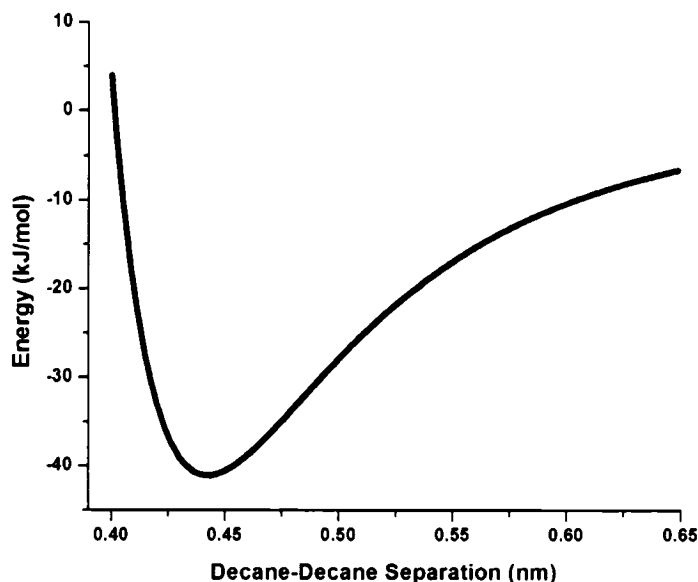


**Figure 6.5:** Lennard-Jones energy calculation as a function of separation between two parallel decane molecules. The energy minimum occurs at a separation of 0.44 nm.

It is interesting to consider the tilt of the alkyl chain typically found in high-quality alkanethiol SAMs. In the case of decanethiol, the molecular tilt has been previously measured to be approximately  $30^\circ$  [120]. As the tilt angle is increased, the actual separation between two adjacent alkyl chains in a high-quality alkanethiol SAM is reduced, as predicted above. Since the equilibrium spacing between the molecular chains is smaller than the spacing between thiol species ( $\sim 0.5$  nm) adsorbed on the gold surface, the net attractive van der Waals force between the alkyl chains is expressed as a reduction of the chain-chain separation via the molecular tilt. A  $30^\circ$  tilt angle results in an effective alkyl chain separation of 0.43 nm, as depicted in Figure 6.6. This measured chain-chain separation is in close agreement with the equilibrium separation calculated for decane (0.44 nm), strongly suggesting that the molecular tilt is in fact governed by van der Waals



interactions between the molecular chains. However, this observation implies that the induced surface stress resulting from alkanethiol SAM formation is not governed by van der Waals interaction between the alkyl chains of adjacent alkanethiol molecules in a SAM. In addition, the fact that the attractive van der Waals forces result in observable molecular tilt in SAMs in the standing-up phase suggest that any electrostatic repulsion (dipole repulsion) between alkyl chains, as suggested by Berger *et al* [11] can also be ruled out as a possible source of the surface stress. If these forces would dominate, the SAM would not exhibit a molecular tilt, since repulsive forces would tend to maximize inter-chain distances.

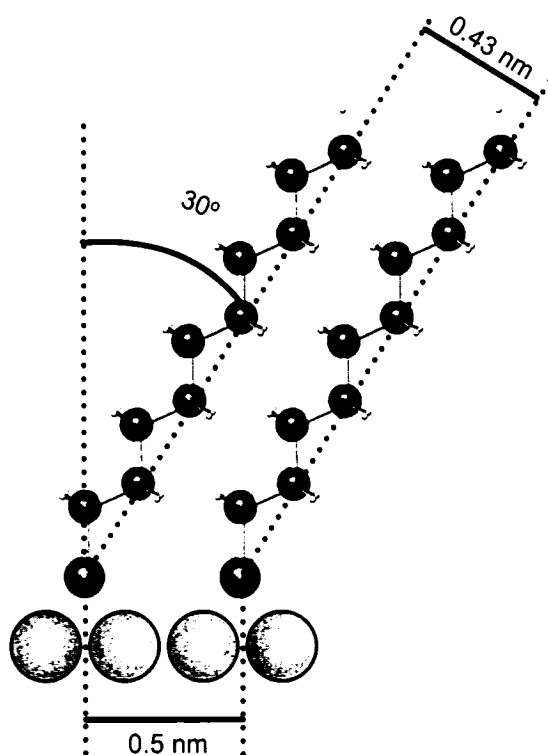


**Figure 6.6: The molecular tilt of approximately 30° found in decanethiol SAMs reduces the inter-molecular distance between adjacent molecules forming the SAM.**

### 6.4.2 Electrostatic Repulsion Model

The self-assembly of an alkanethiol SAM on a gold surface is primarily driven by the sulfur's (thiol) high affinity for gold. In fact, the thiol head group chemisorbs to the gold surface via the formation of a covalent Au-S bond [87,115,117]. The Au-S bond is slightly polar, as it is accompanied by a shift in electron density from the Au towards the S atom [119,130,152]. It has been suggested that such local charge density changes result in a shifting of Au surface atoms (Au-Au bond elongations) due to Coulombic repulsion. Fitts *et al*'s [153] STM studies have monitored such Au surface modifications by tracking changes in gold reconstruction (herringbone structure) resulting from alkanethiol adsorption. The Au-S bond results in partial charge transfer where a charge of approximately 0.3 e ( $0.48 \times 10^{-19}$  C) is transferred between the sulfur and gold atoms forming an  $\text{Au}^+\text{S}^-$  bond [152]. This charge separation at the thiol-gold interface results in the formation of a sheet of like-charges covering the gold surface covered by the SAM. This simplistic picture is depicted in Figure 6.7.

It has been suggested [11] that the surface stress induced during the formation of an alkanethiol SAM on gold originates from the repulsion of adjacent dipolar  $\text{Au}^+\text{S}^-$  bonds. The repulsive force exerted between adjacent negatively charged thiol headgroups, and positively charged Au atoms contributes to the overall observed surface stress. In order to estimate this contribution to the overall observed surface stress, we must estimate the electrostatic energy involved.

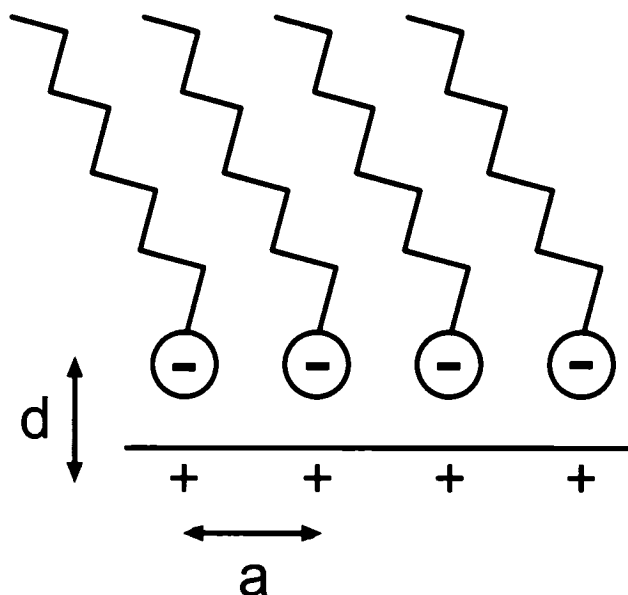


**Figure 6.7:** Alkanethiol SAM formed on a gold surface. The electrostatic model considers the partial charge transfer at the  $\text{Au}^+\text{S}^-$  bond to be like point charges repelling each other. In a SAM, these charges appear as two ‘sheets’ of point charges separated by a distance,  $d$ . The inter-molecule distance,  $a$ , is the distance between adjacent alkanethiol molecules.

The electrostatic energy contribution to this surface stress can be evaluated in a rather simplistic model where the electrostatic energy is summed over all  $\text{Au}^+\text{S}^-$  bonds forming a SAM (on a gold-coated cantilever beam). This total electrostatic energy is counterbalanced by a restoring potential energy resulting from the bent surface of the cantilever. Minimization of the sum of these two energy contributions yields an equilibrium intermolecular separation, which can be converted and interpreted as a surface stress.

In this model, the partial charge transfer at the  $\text{Au}^+\text{S}^-$  bond is treated as two point charges (dipole) separated by a distance  $d$ , while the distance  $a$  separates the charges in adjacent  $\text{Au}^+\text{S}^-$  bonds, as depicted in Figure 6.7. The electrostatic energy,  $E_{es}$ , between two point charges,  $q_1$  and  $q_2$ , separated by a distance,  $r$ , is evaluated using:

$$E_{es} = \frac{1}{4\pi\epsilon_0} \frac{q_1 q_2}{r} \quad \text{Equation 6.3}$$

where  $\epsilon_0$  is  $8.8542 \times 10^{-12} \text{ C}^2\text{N}^{-1}\text{m}^{-2}$  [63]. Given a SAM formed on a rectangular cantilever with a surface area,  $A$ , the number of adsorbed alkanethiol molecules forming the SAM,  $N$ , can be estimated to be  $A/A_{(\sqrt{3}\times\sqrt{3})}$ , where  $A_{(\sqrt{3}\times\sqrt{3})}$  is the area ( $\sim 0.216 \text{ nm}^2$ ) covered by a  $(\sqrt{3}\times\sqrt{3})\text{R}30^\circ$  alkanethiol unit cell of the standing-up phase. The total nearest neighbor electrostatic energy contribution of the SAM is evaluated as:

$$E_{es-tot} = \frac{N}{4\pi\epsilon_0} q_1 q_2 \left[ \frac{2}{a} - \frac{2}{d} - \frac{2}{\sqrt{a^2 + d^2}} \right] \quad \text{Equation 6.4}$$

Next-nearest neighbors and next-next-nearest neighbors were also considered, but are not noted here.

The restoring energy of the bent cantilever can be evaluated using Equation 4.8 and written in terms of  $a$ :

$$E_{cantilever} = \left( \frac{4}{3} \right) \frac{1}{2} k (\Delta z)^2 = \frac{2}{3} k \left( \frac{l^2}{ta} (a - a_0) \right)^2 \quad \text{Equation 6.5}$$

where  $a_0$  is the equilibrium inter-molecular distance (between adjacent alkanethiol) before any lattice increase, equal to  $\sqrt{3} \times 0.28837 \text{ nm} \approx 0.49947 \text{ nm}$  for a  $(\sqrt{3}\times\sqrt{3})\text{R}30^\circ$  lattice. The substitution for  $\Delta z$  is developed in the *Appendix*.

The total energy of the SAM/cantilever system can now be written as:

$$E_{tot} = E_{es-tot} + E_{cantilever} \quad \text{Equation 6.6}$$

The equilibrium value of  $a$  can be found by minimizing Equation 6.6, and the corresponding surface stress can be evaluated using Equation 4.15.

Several groups have attempted to calculate the amount of charge transfer resulting from the adsorption of alkanethiols on a gold surface. Unfortunately, most of these calculations only consider very short alkanethiols, such as methanethiol (C1) or ethanethiol (C2), due to the heavy computational requirements needed to perform calculations on larger molecules. Although the exact adsorption site and the amount of charge transfer is still debated in the literature, recent studies found that the thiol preferentially binds in between the fcc hollow site and bridge sites. The formation of the  $\text{Au}^+\text{S}^-$  bond is accompanied by a charge transfer of approximately 0.30 e ( $0.48 \times 10^{-19}$  C), while the distance between the adsorbed thiolate and the Au surface is calculated to be in the 0.19-0.21 nm range [118,154]. Recently, partial charge distribution calculations were performed locally by C. C. Kaun and H. Guo [155] for longer alkanethiols on Au(111). In the case of octanethiol, a charge transfer of 0.31 e ( $0.50 \times 10^{-19}$  C) between the gold surface and the adsorbed molecule was calculated. It was also found that the negative charge transferred to the alkanethiol molecule was further transferred to the alkyl chain. In terms of the electrostatic model, this can be interpreted as an elongation of the created dipole length,  $d$ . Figure 6.8 shows an example  $E_{tot}$  versus  $a-a_o$  graph for a charge transfer,  $q$ , of 0.31 e and a dipole length,  $d$ , of 0.5 nm. Energy is minimized at  $a-a_o = 11.6$  fm, corresponding to a thiol-thiol separation of 0.49948705 nm, increased from 0.49947545 nm, or about 0.002% elongation. These obtained alkanethiol lattice elongations are then converted to a surface stress.

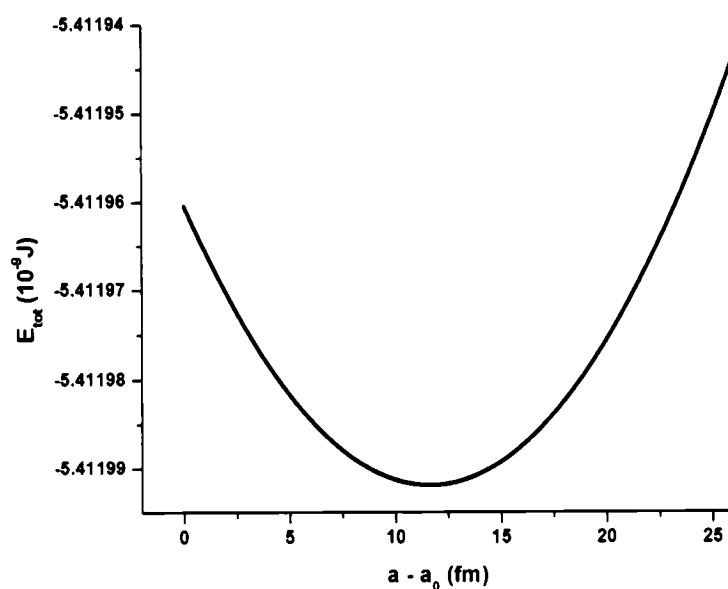
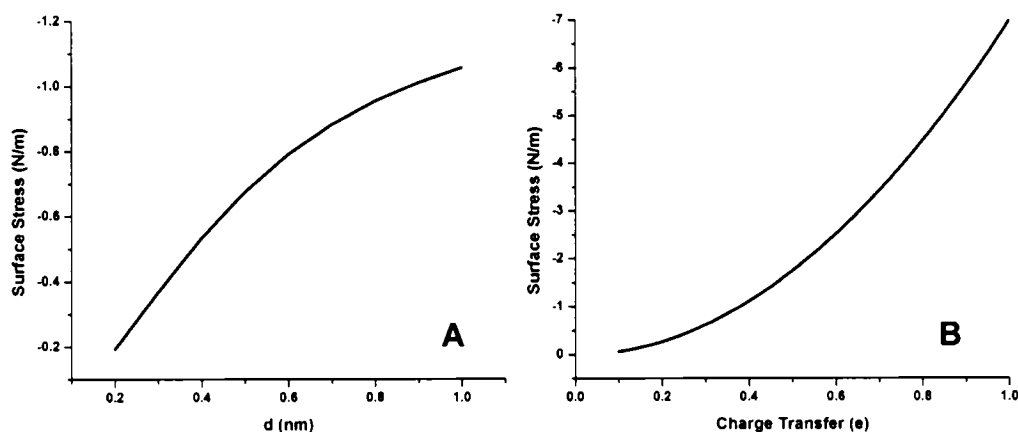


Figure 6.8:  $E_{\text{tot}}$  versus the increase in thiol-thiol separation,  $a - a_0$ . In this example, a charge transfer of 0.311 e was used with a dipole length of 0.5 nm. Energy is minimized at 11.6 fm, corresponding to a thiol-thiol separation of 0.49948705 nm, increased from 0.49947545 nm, or 0.002% elongation.

Figure 6.9 show the surface stress as a function of various values of charge transfer and dipole lengths. Figure 6.9A is a graph of the calculated surface stress as a function of dipole length for a fixed value of charge transfer of 0.31 e ( $0.50 \times 10^{-19}$  C). Figure 6.9B is a graph of the calculated surface stress as a function of charge transfer for a fixed dipole length of 0.5 nm. For a charge transfer of 0.31 e ( $0.50 \times 10^{-19}$  C) and a thiol-to-Au surface distance of 0.2 nm, a compressive surface stress of -0.19 N/m is calculated. If we assume that some charge travels up the alkyl chain, as suggested by calculations performed by Kaun and Guo [155] for octanethiol, we obtain a surface stress of -0.68 N/m for  $q = 0.31$  e ( $0.50 \times 10^{-19}$  C) and  $d = 0.5$  nm. In both these cases, the calculated surface stress is an order of magnitude smaller than what was experimentally measured for a high-quality octanethiol SAM (see Figure 6.2). Considerably larger surface stress values would result from larger values of partial charge transfer, but such charge transfers are unlikely. This suggests that although electrostatic repulsion between

adjacent  $\text{Au}^+\text{S}^-$  units slightly contributes to the overall compressive surface stress, a more detailed model is required to estimate the observed surface stress. This is consistent with the results of Ibach [43] that stipulates that direct repulsive interactions between adsorbate atoms as well as dipolar interactions contribute little to the overall induced surface stress. Although dipole interactions between adsorbed species are important in the formation of adsorbed structures, they do not have a large impact on the surface stress.



**Figure 6.9:** Calculated surface stress due to electrostatic repulsion between adjacent  $\text{Au}^+\text{S}^-$  bonds. The surface stress is plotted (A) as a function of dipole length,  $d$ , with a fixed charge transfer (between Au surface and the adsorbed alkanethiol) of 0.311 e. On the right, the surface stress is plotted (B) versus the amount of transferred charge for a fixed dipole length,  $d$ , of 0.5 nm.

### 6.4.3 Discussion

The simple models developed in this chapter were aimed at gaining some insight into the mechanisms driving the development of a compressive surface stress upon alkanethiol SAM formation on Au(111). Chain-chain interactions were first investigated using a Lennard-Jones (van der Waals) potential. It was found that these interactions would yield an attractive force (tensile surface stress) between

adjacent alkanethiol molecules forming the  $(\sqrt{3}\times\sqrt{3})R30^\circ$  lattice on a Au(111) surface, while the experimentally observed surface stress is compressive. This interaction is expressed as tilting of the alkyl chain formation the SAM. Moreover, published surface pressure measurements acquired using Langmuir-Blodgett techniques [156], sensitive to chain-chain interactions, show no surface stress for molecular packing densities similar to that expected for a SAM in the standing-up phase ( $0.216\text{ nm}^2$ ) [157], as shown in Figure 6.10. At higher packing densities, these measurements show much smaller compressive surface stresses, on the order of mN/m, than what was measured in this work for SAM formation on Au(111) (e.g. Figure 6.1). These results indicate that chain-chain interactions play a minimal role in contributing to the overall induced surface stress.

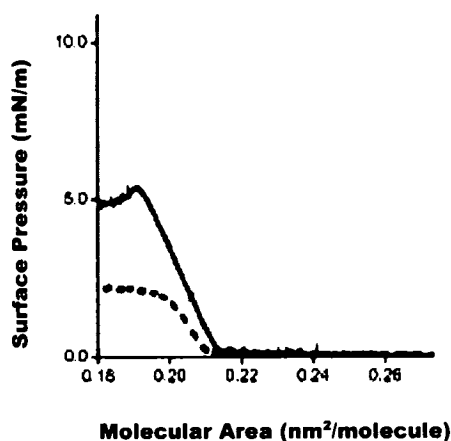


**Figure 6.10:** Surface pressure as a function of molecular density for hexadecanethiol (dashed line) and octadecanethiol (solid line). The graph is modified from [157].

The effect of the polar  $\text{Au}^+\text{S}^-$  bonding was considered next with a simple electrostatic repulsion model, where the  $\text{Au}^+\text{S}^-$  units are treated as adjacent dipoles repelling each other. Although a compressive surface stress is predicted, these electrostatic interactions only account for a fraction (10% at best) of the overall observed surface stress.



These findings seem to indicate that the bulk of the induced surface stress originates at the gold surface, rather than from chain-chain interactions or from direct electrostatic repulsion between adsorbed molecules. Changes in charge distribution of the gold surface atoms can account for the generation of large surface stresses. Surface reconstruction of metals occurs as a mechanism to compensate for the change in charge densities between that of bulk atoms and surface atoms. The formation of a clean metal surface disrupts the electronic charge density present in the bulk of the material. At the surface, the charge smoothing that occurs (to minimize charge density corrugations) results in an increased charge density, effectively strengthening inter-atomic bonds between surface atoms. These stronger bonds are expressed as shorter inter-atomic bond lengths, expressed a tensile surface stress. Au(111) reconstruction relieves some of the inherent tensile surface stress by accommodating an extra Au atom in a  $(23 \times \sqrt{3})$  unit cell of the reconstructed surface, as compared to what is expected for bulk Au, while maintaining the required short bond lengths between gold surface atoms. Upon alkanethiol adsorption, electronic charge moves from the gold surface atoms towards the adsorbed molecule, and reduces the tensile surface stress inherent in a clean surface. In fact, we have found that this induced surface stress is large and compressive. The electronic charge transfer away from the gold surface atoms effectively reduces the bond strength between gold surface atoms, increasing inter-atomic distances, and producing a compressive surface stress. We suggest that alkanethiol adsorption promotes the ejection of gold atoms from the surface to compensate for the decrease in inter-atomic bond strength and to allow for greater inter-atomic bond lengths (by decreasing the density of gold surface atoms). The charge redistribution resulting from alkanethiol adsorption provides the necessary driving force for the creation of the observed etch pits or vacancy islands [121].

The epitaxial growth of a metal atomic monolayer on a metal substrate (different metal than the adsorbed metal) has also been shown to generate large surface

stresses in some cases. For example, the deposition of Ag on a Pt(111) surface results in a compressive surface stress of -8.8 N/m per adsorbed monolayer [158], with as much as -30 N/m induced by the deposition of 7 monolayers. Leiva *et al* [159] used both a simple continuum model and the embedded-atom method (EAM) to calculate the surface stress induced in these epitaxially grown systems. The simple continuum model yields a surface stress by considering the lattice misfit between the adsorbed monolayer and the surface lattice. Given the substrate's Young's modulus and Poisson's ratio, it is possible to estimate the surface stress resulting from monolayer adsorption on a surface. The embedded-atom method also yields a surface stress, but is a more complicated method based on density-functional theory where many-body electronic interactions between electrons are considered, also taking into account the metallic bonding between the adsorbed monolayer and the substrate [160]. Leiva *et al* [159] found good agreement between his calculation using the embedded-atom method (-7.76 N/m) and the result of Grossmann *et al* for the epitaxial growth of Ag on Pt(111). W. Haiss [44] adds that the embedded-atom method is more appropriate (than the continuum model) for monolayer/substrate systems involving a charge transfer between the adsorbed monolayer and the substrate.

Notwithstanding the choice in the theoretical approach used to model the induced surface stress resulting from alkanethiol SAM formation on Au(111), which is beyond the scope of this work, the calculation of surface stress will have to consider changes in the charge distribution of the Au surface atoms as a major mechanism for the generation of the surface stress.

## 6.5 Summary/Discussion

The surface stress induced during the formation of alkanethiol SAMs on gold-coated cantilevers was measured for various molecular chain lengths. It was found that the induced surface stress is not dependent on alkanethiol chain length.

This contradicts the findings of Berger *et al* [11] where chain length dependence was observed. They suggest that the larger measured surface stress for longer alkanethiols resulted from a charge transfer at the  $\text{Au}^+\text{S}^-$  bond that propagates along the alkyl chain. The longer chains imply longer dipole lengths thus a larger induced surface stress. A simple calculation based on an electrostatic repulsion model was considered and found to contradict this assertion. Specifically, the findings presented in *Chapter 5* suggest that the results of Berger are consistent with our surface stress measurements for SAM formation on small-grained gold, where the resulting monolayer is not a high-quality SAM in the standing-up phase, but rather is composed of a mixture of phases, predominantly the lying-down phase. The results presented here are for SAM formation on gold surfaces having much larger average grain sizes. In such cases, the induced surface stress is not only quantitatively much larger, but the resulting SAM is of much higher quality, being predominantly in the standing-up phase. Additionally, the lack of chain length dependence is consistent with the results of Kaun and Guo [155] that shows that the amount of charge transfer at the  $\text{Au}^+\text{S}^-$  bond is independent of chain length for alkanethiols longer than butanethiol (C4).

The induced surface stress was measured as a function of average gold grain size. The equilibrium surface stress increased linearly as a function of Au grain size. This is again consistent with the results of *Chapter 5* where it was shown that SAM formation can be considerably inhibited in the case of formation on gold surface having small grains ( $< 100$  nm). Unfortunately, the results shown in Figure 6.2 did not clearly resolve the threshold grain size at which the transition into the standing-up phase is favored. Gold film deposition by thermal evaporation produce surfaces with a large spread in grain sizes. Therefore, although the SAM formed on large-grained gold will be predominantly in the standing-up phase, there may be a fraction of the SAM that will form on smaller grains, and will therefore not undergo the transition into the standing-up phase. The measured surface stress is therefore the result of a SAM composed of mixed phases. Larger surface stresses are measured for larger average grain sizes since a

larger fraction of the SAM will be grown on large grains as compared to what will be formed on smaller grains. The result of Figure 6.2 gives a lower bound to the theoretical surface stress expected for a perfect SAM formed on an infinitely large gold grain.

Modeling was undertaken in order to determine the possible origins of the induced surface stress. Lennard-Jones (van der Waals) -type chain-chain interactions were ruled out as the main source of the compressive surface stress since these forces would produce tensile surface stresses. Repulsive electrostatic interactions resulting from the polar nature of the  $\text{Au}^+\text{S}^-$  bond account for part (10% at best) of the total compressive surface stress. These calculations revealed that this simple model does not predict the large surface stresses measured experimentally. Nevertheless, these calculations, and ones performed by others for atomic monolayer formation on metals, suggest that the surface stress originates as the result of the changes in electronic configuration of the gold surface atoms. More complex approaches need to be considered to account for the measured surface stress.

Cantilever-based sensors are being developed for a variety of different applications. Optimization of these sensors should consider the fundamental origins of the induced surface stress, as different systems will surely be driven by different mechanisms. For example, the sensing of bulky molecules might produce compressive surface stresses resulting from steric-type interactions between the adsorbed molecules, as opposed to actual modification of the electronic structure of the underlying substrate surface atoms. These effects are expected to lead to much smaller surface stresses than that induced by changes in charge density between surface atoms. The sensitivity of these cantilever-based surface stress sensors can be greatly improved by tailoring the sensor's response, on a molecular scale, such that the binding of a target onto the cantilever modifies the charge density at the surface. Using these sensors in this mode is essential if they are to become a viable technology.

## **7 Summary and Outlook**

### **7.1 Summary**

The self-assembly of alkanethiol monolayers on gold surfaces from the vapor phase was the focus of the present study. This self-assembled system was investigated as a model system in order to obtain a fundamental understanding of the sensor's response and of self-assembled systems in general. The measurement of the surface stress induced during the formation of alkanethiol SAMs on gold-coated cantilevers led to insight into the self-assembly process. These measurements were also used to identify some of the surrounding environmental conditions that affect analyte adsorption on the cantilever surface, and consequently influence the sensor's response. Finally this work also sought to answer some of the open questions found in the literature regarding the mechanisms that drive alkanethiol self-assembly.

The advent of atomic force microscopy (AFM), and the inevitable commercial-availability of AFM cantilevers, has brought about the development of a wide variety of cantilever-based sensors. Moreover, micro-fabrication techniques have made it possible to make micro- and even nano-sized cantilevers resulting in an increase in these sensors' sensitivity and a reduction in response time. Experiments aimed at understanding the mechanisms that provide a sensor response, such as a surface stress in the case of molecular sensing, are essential in eventually improving sensitivity and financial marketability.

A cantilever-based sensor with differential capabilities was designed and built. This system yields sensitive surface stress measurements, and can accommodate cantilevers with various chemistries to be used in numerous sensing applications. This sensor is capable of measuring surface stresses as small as  $5 \times 10^{-5}$  N/m given 0.2 nm deflection sensitivity with the cantilevers used in this study. A unique system combining a cantilever-based sensor and an ellipsometer was also designed and built. This system yields simultaneous *in situ* surface stress and monolayer thickness measurements. Although it was shown that ellipsometric measurements are very difficult to interpret given the assumption of a constant index of refraction for all phases and the presence of a mixture of structural phases in a partially formed SAM, the use of such complementary techniques is important for the understanding of the mechanisms that drive the self-assembly process, and the induced surface stress. STM was also used in conjunction with these instruments to determine structure of the resulting SAMs, making it possible to correlate the observed features in the surface stress profiles with various structural phases that exist during the formation of alkanethiol SAMs.

The following chapter developed a procedure to convert the measured sensor signal into an actual cantilever deflection. In addition, a novel methodology used to convert this measured cantilever deflection into a surface stress was developed. This methodology overcomes some limitations encountered when using the often-used Stoney formula, mainly by eliminating the need to know the cantilever material's Young's modulus, which can have a very large uncertainty. This method lumps the cantilever's elastic properties into a readily measurable spring constant.

The surface stress profiles measured during alkanethiol SAM formation revealed evidence of structural phase transitions, as supported by complementary STM imaging. These phase transitions were also found in simultaneous ellipsometric thickness measurements, but were not as easily interpreted. The same surface stress measurements were used to evaluate the influence of the gold substrate

morphology on the monolayer formation process. It was found that the SAM can become kinetically trapped in an intermediate structural phase when formed on a gold surface having relatively small grains ( $< 100$  nm). SAMs formed on large-grained gold were found to be of high quality reaching the standing-up phase and exhibiting the  $c(4\times 2)$  superlattice of the  $(\sqrt{3}\times\sqrt{3})R30^\circ$  lattice. The equilibrium surface stress was found to increase with the gold grain size. These data did not provide a clear gold grain size value at which the transition into the standing-up phase is allowed. This was attributed to the fact that the gold films prepared by thermal evaporation exhibited average grain sizes with large variances. The result is that even large-grained gold included a certain percentage of small grains. SAMs formed on small-grained gold were further kinetically trapped in the unstacked lying-down phase when the alkanethiol vapor concentration in the early stages of formation was low. Gold surface contamination by exposure to laboratory air was also evident in the surface stress profiles.

The cantilever-based sensor was also used to compare the surface stress induced during the formation of alkanethiol SAMs of various chain lengths. Contrary to what has been previously published by Berger *et al* [11], no chain length dependence was found. These findings were supported by simple modeling of the origins of the surface stress. Lennard-Jones-type chain-chain interactions were ruled out as the origin of the observed compressive surface stress since it predicted tensile surface stresses. Electrostatic repulsion between adjacent  $\text{Au}^+\text{S}^-$  polar covalent bonds correctly predicted a compressive surface stress, but failed to account for the large surface stress measured using the sensor. Consequently, the surface stresses were found to originate at the level of the gold surface atoms. Redistribution of electronic charge at the gold surface is responsible for the observed surface stress. The fact that the amount of charge transfer at the  $\text{Au}+\text{S}$ -bond is chain length independent for alkanethiols longer than butanethiol (C4) is consistent with our finding that the induced surface stress is chain length independent for hexanethiol (C6), octanethiol (C8) and decanethiol (C10). A theoretical understanding of the mechanisms responsible for adsorption-induced

surface stress remains to be further developed, as many different processes are often involved from system to system. A more involved theoretical approach is needed to correctly model the origins of the experimentally measured equilibrium surface stresses induced during the formation of alkanethiol SAMs.

## 7.2 Outlook

Alkanethiol SAM formation is often chosen as a simple model system in the general study of self-assembly. Nevertheless, the countless works found in the literature have exposed the complex nature of alkanethiol SAM formation. Scientists are realizing that this self-assembled system is far from being simple, as there are many questions that remain to be addressed. Although we have started to develop a reliable qualitative picture of the self-assembly process, a full quantitative understanding is far from achieved. This section will suggest some experiments that will complement our current understanding of alkanethiol SAM formation, especially in term of the induced surface stress and corresponding structure.

The measurements presented herein have shown that the surface stress induced by the SAM is independent of the chain length of the alkanethiol molecule. We have also shown that the amount of charge transfer at the  $\text{Au}^+\text{S}^-$  bond as calculated through *ab initio* calculations [155] is also independent for alkanethiol of lengths greater than butanethiol (C4). In other words, the gold surface atoms cannot distinguish alkanethiols of different lengths, as long as they are longer than butanethiol. Measurement of the surface stress induced by the formation of short alkanethiol SAMs ( $< \text{C4}$ ) should show a chain length dependence if the assertion that the bulk of the surface stress results from changes in the electronic structure of the gold surface atoms is correct. These experiments would certainly contribute to a greater theoretical understanding of the origins of the surface stress.



Another major result presented in this work is the effect of the gold surface morphology on the formation process of alkanethiol SAM, and the resulting surface stress. It was demonstrated that there is a critical gold grain size that is required for the transition into the standing-up phase to be allowed. It is difficult to experimentally assess the theoretical maximum value of surface stress induced by a “perfect” SAM. Firstly, gold surfaces with a large average grain size often have some percentage of small grains on which the SAM remains in a lying-down phase. Secondly, any theoretical approach will have to consider that SAMs are composed of adjacent domains of the standing-up phase. The contribution of the resulting domain boundaries to the overall induced surface stress might have to be treated as “defects” in an overall infinitely large single-domain SAM in the standing-up phase. Preparation of better gold surfaces (large grains, fully reconstructed Au(111)) on the cantilever surface should yield an experimentally determined maximum surface stress, as the SAM formed on this surface will exhibit very few defects due to the presence of gold grain boundaries. Annealing of the gold-coated cantilevers produces larger grains, but overheating results in a permanent cantilever bending that can make the sensor difficult or impossible to use. In addition, overheating ( $>350\text{ }^{\circ}\text{C}$ ) of a gold-covered silicon or silicon nitride surface results in a poor quality surface. Improvements of the methods used to prepare gold-coated cantilevers with larger gold grains will help in the determination of the maximum induced surface stress. One possible method to achieve this might be to physically pre-bend the cantilever in the opposite direction during gold evaporation to eliminate excessive permanent bending of the cantilever. Using cantilevers made of different materials might make it easier to anneal the gold surface, yielding better gold films. Producing cantilevers entirely made of gold would certainly eliminate these problems by allowing thorough annealing, producing large Au(111) crystals. In such cases, methods to passivate the opposing (backside) of the cantilever would also have to be developed.

The features in the surface stress profile acquired during alkanethiol SAM formation have been associated with various structural phases that occur during monolayer formation. If SAM formation can be interrupted during formation, STM imaging of these partial SAMs would confirm our findings. STM imaging of the SAM resulting from formation on small-grained gold that exhibit a release in the surface stress profile should be performed to confirm that this SAM is indeed in the unstacked lying-down phase. Currently, this assertion is solely based on simultaneous ellipsometric measurements, which can be difficult to interpret. Challenges obtaining molecular resolution on small gold grains (due to tip convolution effects at grain boundaries) would have to be overcome.

Ellipsometry can provide sensitive monolayer thickness measurements in real-time during SAM formation. Ellipsometric measurements have been used by several authors [140,161,162] in the study of alkanethiol SAM formation. We have shown that SAM thicknesses measured by single-wavelength ellipsometry can be difficult to interpret if not used in complement with other experimental techniques. In fact, phase identification using ellipsometry alone is highly non-trivial, if not impossible. Variations of the SAM's index of refraction (of different structural phases) during formation make conversion of the ellipsometric signal into an actual thickness difficult. Techniques such as multiple wavelength ellipsometry or surface plasmon resonance are capable of yielding [135] thickness and index of refraction measurements. Combining a cantilever-based surface stress sensing with surface plasmon resonance could yield valuable information on the surface stress associated with various structural phases.

We have already begun work on using functionalized alkanethiol SAMs as sensing layer formed on the cantilever surface. Oligonucleotides are chemically attached to alkanethiol molecules. When these functionalized molecules form a SAM on the cantilever surface, the cantilever becomes a tailored sensor capable of sensing ssDNA with specific base sequences. This work will add to the current literature on DNA sensing by aiming to improve on the sensitivity expressed by

current DNA sensing technologies, and to improve on recognition of base sequence mismatches. A label-free method to sense DNA can potentially revolutionize the field of genomics. An understanding of the underlying mechanisms that drive these sensors' response will be crucial in improving on current cantilever-based DNA sensing technologies.

Our group has also combined cantilever-based sensing with electrochemistry. This electrochemical arrangement will allow us to verify some of the findings concerning the origin of the induced surface stress by reversibly adsorbing and desorbing various molecular species on a gold-coated cantilever. This extra control on the adsorption of analyte on the gold surface will make it easier to verify different theoretical models.

A greater understanding of self-assembled systems is essential as scientists seek to build nanoscale structure using a bottom-up approach. This study of alkanethiol monolayer self-assembly has shown the complex nature of this seemingly simple model system. We have investigated the self-assembly of alkanethiol SAMs on gold-coated cantilevers in an effort to characterize these sensors' response, and to provide a greater understanding of the mechanisms responsible for molecular assembly. This thesis identifies and characterizes some of the factors that influence the kinetics, structure, and surface stress of these SAMs. These findings form a strong basis for the development and optimization of new cantilever-based sensor technologies.



---

## Appendix

---

### ➤ *Concentrated Load versus Surface Stress*

The energy stored in the stressed cantilever calculated using Hooke's law,  $E = \frac{1}{2} k \Delta z^2$ , is for a concentrated load at the tip,  $F_{tip}$ , of the cantilever, whereas the deflection caused by surface stress is the result of a bending moment,  $M_{stress}$ , acting over the entire length of the cantilever. Our task is therefore to derive the ratio in energies stored in the stressed cantilever due to the actual surface stress compared to the calculated concentrated-load energy, for a similar deflection.

We start by calculating the elastic strain energy,  $E_{elastic}$ , for both modes of deflection using Equation 4.9, restated below:

$$E_{elastic} = \int \frac{M^2}{2E^* I} dy \quad \text{Equation A.1}$$

where the integration is performed over the length of the cantilever (in the y-direction),  $l$ , and the bending moment is expressed as [104]:

$$M_{tip} = F_{tip} y \quad \text{Equation A.2}$$

for a concentrated load acting at the tip of the cantilever, and as [102]:

$$M_{stress} = \frac{\Delta \sigma W t}{2} \quad \text{Equation A.3}$$

for a deflection resulting from a uniform surface stress,  $\Delta\sigma$ . Here,  $W$  is the width of the rectangular cantilever, and  $t$  is its thickness.

However, Miyatani *et al* [102] also expressed the bending moment due to a uniform surface stress,  $M_{stress}$ , in terms of an equivalent concentrated force,  $F_{tip}$ , for an equal deflection at the end of the cantilever:

$$M_{stress} = \frac{2}{3} F_{tip} l \quad \text{Equation A.4}$$

Finally, we can calculate the ratio of the strain energies for a surface stress,  $E_{elastic/stress}$ , and for a concentrated load,  $E_{elastic/tip}$ , as calculated from Equation A.1. The result is presented in Equation A.5:

$$\frac{E_{elastic/stress}}{E_{elastic/tip}} = \frac{4}{3} \quad \text{Equation A.5}$$

➤ *Writing the deflection,  $\Delta z$ , in terms of the lattice elongation,  $a-a_0$*

From Figure 4.5, we can write  $\Delta z = R - z$  and  $z = R \cos(\beta)$ . Moreover, the arc length defined by the bent cantilever can be expressed as  $s = R\beta = l$ . These expressions allow us to write:

$$\Delta z = \frac{s}{\beta} (1 - \cos(\beta)) \approx \frac{s\beta}{2} = \frac{l\beta}{2} \quad \text{Equation A.6}$$

since  $(1 - \cos(\beta))\beta^{-1} \approx \beta/2$ .

The top surface of the bent cantilever will have a length,  $s'$ ,

$$s' = \left( R - \frac{t}{2} \right) \beta = R\beta + \frac{t\beta}{2} = l + \frac{t\beta}{2} \quad \text{Equation A.7}$$

The top surface of the cantilever will increase in length,  $\Delta s'$ , as a result of a deflection,

$$\Delta s' = s' - l = \frac{t\beta}{2} \quad \text{Equation A.8}$$

From this, the increase in dipole-dipole separation for a given cantilever deflection,  $\Delta z$ , from its equilibrium value,  $a_0$ , can be calculated by combining Equation A.6 and Equation A.8,

$$a - a_0 = \Delta a = \frac{\Delta s'}{l} a_0 = \frac{t\beta}{2l} a_0 = \frac{ta_0}{2l} \frac{2\Delta z}{l} = \frac{ta_0}{l^2} \Delta z \quad \text{Equation A.9}$$

To simplify,

$$\Delta z = \frac{l^2}{ta_0} \Delta a \quad \text{Equation A.10}$$

## References

- <sup>1</sup> J. R. Heath; P. J. Kuekes; G. S. Snider; and R. S. Williams; *Science* 280, 1716 (1998)
- <sup>2</sup> M. A. Reed; J. Chen; A. M. Rawlett; D. W. Price; and J. M. Tour; *Science* 78, 3735 (2001)
- <sup>3</sup> M. R. Diehl; S. N. Yaliraki; R. A. Beckman; M. Barahona; J. R. Heath; *Angewandte Chemie International Edition* 41, 353 (2002)
- <sup>4</sup> J. Alper; *Science* 296, 838 (2002)
- <sup>5</sup> K. L. Prime, and G. M. Whitesides, *Journal of the American Chemical Society* 115, 10714 (1993)
- <sup>6</sup> P. A. DiMilla, J. P. Folkers, H. A. Biebuyck, R. Haerter, G. P. Lopez, G. M. Whitesides; *Journal of the American Chemical Society* 116, 2225 (1994)
- <sup>7</sup> G. Binnig, C. F. Quate, and Ch. Gerber; *Physical Review Letters* 56, 930 (1986)
- <sup>8</sup> F. J. Giessibl, *Science* 289, 422 (2000)
- <sup>9</sup> H. P. Lang, M. Hegner, E. Meyer, and Ch. Gerber; *Nanotechnology* 13, R29 (2002)
- <sup>10</sup> R. G. Nuzzo, D. L. Allara; *Journal of the American Chemical Society* 105, 4481 (1983)
- <sup>11</sup> R. Berger, E. Delamarche, H. P. Lang, Ch. Gerber, J. K. Gimzewski, E. Meyer, and H.-J. Güntherodt; *Science* 276, 2021 (1997)
- <sup>12</sup> Concentris; <http://www.concentris.ch>
- <sup>13</sup> Veeco; <http://www.veeco.com>
- <sup>14</sup> Xsilogy, formerly Graviton Inc.; <http://www.graviton.com/> or <http://www.xsilogy.com>
- <sup>15</sup> J. Fritz; M. K. Baller; H. P. Lang; H. Rothuizen; P. Vettiger; E. Meyer; H.-J. Güntherodt; Ch. Gerber; and J. K. Gimzewski; *Science* 288, 316 (2000)
- <sup>16</sup> J. Fritz; M. K. Baller; H. P. Lang; T. Strunz; E. Meyer; H.-J. Güntherodt; E. Delamarche; Ch. Gerber; and J. K. Gimzewski; *Langmuir* 16, 9694 (2000)
- <sup>17</sup> F. Frederix, K. Bonroy, W. Laureyn, G. Reekmans, A. Campitelli, W. Dehaen, and G. Maes; *Langmuir* 19, 4351 (2003)
- <sup>18</sup> M. Alvarez, A. Calle, J. Tamayo, L. M. Lechuga, A. Abad, and A. Montoya; *Biosensors and Bioelectronics* 18, 649 (2003)
- <sup>19</sup> H. Jensenius; J. Thaysen; A. A. Rasmussen; L. H. Veje; O. Hansen; and A. Boisen; *Applied Physics Letters* 76, 2615 (2000)
- <sup>20</sup> D. R. Baselt; B. Fruhberger; E. Klaassen; S. Cemalovic; C. L. Britton Jr.; S. V. Patel; T. E. Mlsna; D. McCorkle; and B. Warmack; *Sensors and Actuators B* 88, 120 (2003)
- <sup>21</sup> R. Marie; H. Jensenius; J. Thaysen; C. B. Christensen; and A. Boisen; *Ultramicroscopy* 91, 29 (2002)
- <sup>22</sup> G. Wu; H. Ji; K. Hansen; T. Thundat; R. Datar; R. Cote; M. F. Hagan; A. K. Chakraborty; and A. Majumdar; *Proceedings of the National Academy of Sciences* 98, 1560 (2001)
- <sup>23</sup> K. Hansen; H.-F. Ji; G. Wu; R. Datar; R. Cote; A. Majumdar; and T. Thundat; *Analytical Chemistry* 73, 1567 (2001)
- <sup>24</sup> Affymetrix
- <sup>25</sup> Y. Arntz; J. D. Seelig; H. P. Lang; J. Zhang; P. Hunziker; J. P. Ramseyer; E. Meyer; M. Hegner; and Ch. Gerber; *Nanotechnology* 14, 86 (2003)
- <sup>26</sup> G. Wu; R. H. Datar; K. M. Hansen; T. Thundat; R. J. Cote; and A. Majumdar; *Nature* 19, 856 (2001)
- <sup>27</sup> A. Subramanian; P. I. Oden; S. J. Kennel; K. B. Jacobson; R. J. Warmack; T. Thundat; and M. J. Doktycz; *Applied Physics Letters* 81, 385 (2002)
- <sup>28</sup> M. Alvarez; A. Calle; J. Tamayo; L. M. Lechuga; A. Abad; and A. Montoya; *Biosensors and Bioelectronics* 18, 649 (2003)
- <sup>29</sup> J. R. Barnes, R. J. Stephenson, C. N. Woodburn, S. J. O'Shea, M. E. Welland, T. Rayment, J. K. Gimzewski, and Ch. Gerber; *Review of Scientific Instruments* 65, 3793 (1994)



- <sup>30</sup> J. R. Barnes; R. J. Stephenson; C. N. Woodburn; S. J. O'Shea; and M. E. Welland; Review of Scientific Instruments 65, 3793 (1994)
- <sup>31</sup> J. R. Barnes; R. J. Stephenson; C. N. Woodburn; S. J. O'Shea; and M. E. Welland; Review of Scientific Instruments 65, 3793 (1994)
- <sup>32</sup> E. Meyer; J. K. Gimzewski; Ch. Gerber; and R. R. Schlittler; *Nato ASI Series E Applied Sciences – Advanced Study Institute* **292**, 89 (1995)
- <sup>33</sup> C. E. Borroni-Bird, N. Al-Sarraf, S. Andersoon, and D. A. King; Chemical Physics Letters 183, 516 (1991)
- <sup>34</sup> E. Meyer; J. K. Gimzewski; Ch. Gerber; and R. R. Schlittler; *Nato ASI Series E Applied Sciences – Advanced Study Institute* **292**, 89 (1995)
- <sup>35</sup> T. Bachelis; F. Tiefenbacher; R. Schäfer; *Journal of Chemical Physics* **110**, 10008 (1999)
- <sup>36</sup> J. K. Gimzewski, Ch. Gerber, E. Meyer, and R. R. Schlittler; Chemical Physics Letters 217, 589 (1994)
- <sup>37</sup> J. R. Barnes, R. J. Stephenson, M. E. Welland, Ch. Gerber, and J. K. Gimzewski; Nature 372, 79 (1994)
- <sup>38</sup> B. Illic; D. Czaplewski; M. Zalalutdinov; H. G. Craighead; P. Neuzil; C. Campagnolo; and C. Batt; Journal of Vacuum Science and Technology B 19, 2825 (2001)
- <sup>39</sup> A. Gupta; D. Akin; and R. Bashir; Applied Physics Letters 84, 1976 (2004)
- <sup>40</sup> B. Illic; H. G. Craighead; S. Krylov; W. Senaratne; C. Ober; and P. Neuzil; Journal of Applied Physics 95, 3694 (2004)
- <sup>41</sup> H. P. Lang; M. K. Baller; R. Berger; Ch. Gerber; J. K. Gimzewski; F. M. Battiston; P. Fornaro; J. P. Ramseyer; E. Meyer; and H.-J. Güntherodt; Analytica Chimica Acta 393, 59 (1999)
- <sup>42</sup> H. P. Lang; M. Hegner; E. Meyer; and Ch. Gerber; Nanotechnology 13, R29 (2002)
- <sup>43</sup> H. Ibach; Surface Science Reports 29, 193 (1997)
- <sup>44</sup> W. Haiss; Reports on Progress in Physics 64, 591 (2001)
- <sup>45</sup> C. E. Bach, M. Giesen, and H. Ibach; Physical Review Letters 78, 4225 (1997)
- <sup>46</sup> U. Tartaglino, E. Tosatti, D. Passerone, and F. Ercolessi; Physical Review B 65, 241406 (2002)
- <sup>47</sup> R. M. Tromp, A. W. Denier van der Gon, and M. C. Reuter; Physical Review Letters 68, 2313 (1992)
- <sup>48</sup> K. Pohl, M. C. Bartelt, J. de la Figuera, N. C. Bartelt, J. Hrbek, and R. Q. Hwang; Nature 397, 238 (1999)
- <sup>49</sup> V. Heine and L. D. Marks; Surface Science 165, 65 (1986)
- <sup>50</sup> M. W. Finnis and V. Heine; Journal of Physics F: Metal Physics 4, L37 (1974)
- <sup>51</sup> S. Y. Tong, and A. L. Maldonado; Surface Science 78, 459 (1978)
- <sup>52</sup> A. J. Schell–Sorokin, and R. M. Tromp; Physical Review Letters 64, 1039 (1990)
- <sup>53</sup> A. García, and J. E. Northrup; Physical Review B 48, 17350 (1993)
- <sup>54</sup> R. Shuttleworth; Proceedings of the Physical Society A 63, 444 (1950)
- <sup>55</sup> C. W. Mays, J. S. Vermaak, and D. Kuhlmann-Wilsdorf; Surface Science 12, 134 (1968)
- <sup>56</sup> H. J. Wasserman, and J. S. Vermaak; Surface Science 32, 168 (1972)
- <sup>57</sup> M. Godin, O. Laroche, V. Tabard-Cossa, L. Y. Beaulieu, P. Grütter, and P. J. Williams, Review of Scientific Instruments 74, 4902 (2003)
- <sup>58</sup> Silicon-MDT/MikroMasch
- <sup>59</sup> Veeco silicon nitride cantilevers model #MLCT-NOHW
- <sup>60</sup> R. Raiteri; M. Grattarola; H.-J. Butt; and P. Skládal; Sensors and Actuators B 79, 115 (2001)
- <sup>61</sup> D. Rugar, H. J. Mamin, and P. Güthner; Applied Physics Letters 55, 2588 (1989)
- <sup>62</sup> Blue Sky Research Inc.
- <sup>63</sup> E. Hecht; "Optics, 2<sup>nd</sup> Ed.", Addison-Wesley Publishing Company, 1987.
- <sup>64</sup> Newport Corporation.
- <sup>65</sup> OZ Optics
- <sup>66</sup> New Focus
- <sup>67</sup> OPA111 from Burr-Brown used as I-V converters.
- <sup>68</sup> OPA627BP from Burr-Brown.
- <sup>69</sup> MPY634KP from Burr-Brown
- <sup>70</sup> Measurement Computing Inc.
- <sup>71</sup> PEEK (polyetheretherketone) by Victrex.

- <sup>72</sup> KEL-F (Chlorotrifluoroethylene) by 3M.
- <sup>73</sup> Boiling a 50/50 ethanol/chloroform solution can be a fire hazard. The use of a spark-proof heater is recommended.
- <sup>74</sup> W. E. Boyce, and R. C. DiPrima; "Elementary Differential Equations and Boundary Value Problems, 5<sup>th</sup> Ed.", John Wiley & Sons, Inc., 1992.
- <sup>75</sup> N. W. Ashcroft, and N. D. Mermin; "Solid State Physics", Saunders College Publishing, 1976.
- <sup>76</sup> R. C. Weast; "CRC Handbook of Chemistry and Physics, 56<sup>th</sup> Ed.", CRC Press, 1975-1976.
- <sup>77</sup> 
$$\operatorname{erfc}(z) = \frac{2}{\sqrt{\pi}} \int_z^{\infty} \exp(-t^2) dt$$
- <sup>78</sup> Private communication with Dan Friend at NIST.
- <sup>79</sup> E. Delamarche; H. Schmidt; A. Bietsch; N. B. Larsen; H. Rothuizen; B. Michel; and H. Biebuyck; *Journal of Physics Chemistry B* 102, 3324 (1998)
- <sup>80</sup> Sigma-Aldrich
- <sup>81</sup> E. Delamarche; B. Michel; H. Kang; and Ch. Gerber; *Langmuir* 10, 4103 (1994)
- <sup>82</sup> G. E. Poirier; *Langmuir* 15, 1167 (1999)
- <sup>83</sup> T. Kakiuchi, K. Sato, M. Iida, D. Hobara, S.-I. Imabayashi, and K. Niki, *Langmuir* 18, 7238 (2000)
- <sup>84</sup> TE Technologies, Inc.
- <sup>85</sup> McShane Inc., Model #5C7-378
- <sup>86</sup> Oven Industries Inc., Model # STD-1462
- <sup>87</sup> D. K. Schwartz; *Annual Review of Physical Chemistry* 52, 107 (2001)
- <sup>88</sup> Gaertner Scientific Inc.
- <sup>89</sup> O. Laroche; "Study of the Formation Dynamics of Self-Assembled Monolayers by Ellipsometry", M.Sc. Thesis, McGill University (2002)
- <sup>90</sup> Digital Instruments
- <sup>91</sup> Goodfellow
- <sup>92</sup> S.-I. Park, and C. F. Quate; *Applied Physics Letters* 48, 112 (1986)
- <sup>93</sup> <http://www.webelements.com>
- <sup>94</sup> 99.995% purity, Alfa Aesar
- <sup>95</sup> 99.99% purity, Angstrom Sciences
- <sup>96</sup> V-4 grade, SPI Supplies
- <sup>97</sup> M. Godin, V. Tabard-Cossa, P. Grütter, and P. Williams, *Applied Physics Letters* 79, 551 (2001)
- <sup>98</sup> G. G. Stoney; *Proceedings of the Royal Society of London, Series A* 82, 172 (1909)
- <sup>99</sup> J. E. Sader; *Journal of Applied Physics* 89, 2911 (2001)
- <sup>100</sup> L. B. Freund, J. A. Floro, and E. Chason; *Applied Physics Letters* 74, 1987 (1999)
- <sup>101</sup> C. A. Klein; *Journal of Applied Physics* 88, 5487 (2000)
- <sup>102</sup> T. Miyatani, and M. Fujihira; *Journal of Applied Physics* 81, 7099 (1997)
- <sup>103</sup> J. E. Sader, I. Larson, P. Mulvaney, and L. R. White; *Review of Scientific Instruments* 66, 3789 (1995)
- <sup>104</sup> R. J. Roark; "Formulas for Stress and Strain", McGraw-Hill Book Company, 1965.
- <sup>105</sup> G. Y. Chen, R. J. Warmack, T. Thundat, D. P. Allison, and A. Huang; *Review of Scientific Instruments* 65, 2532 (1994)
- <sup>106</sup> D. Sarid; "Scanning Force Microscopy with Applications to Electric, Magnetic, and Atomic Forces", Oxford University Press, New York, 1994. (Chap. 1)
- <sup>107</sup> G. Y. Chen, T. Thundat, E. A. Wachter, and R. J. Warmack; *Journal of Applied Physics* 77, 3618 (1995)
- <sup>108</sup> J. E. Sader, J. W. M. Chon, and P. Mulvaney; *Review of Scientific Instruments* 70, 3967 (1999)
- <sup>109</sup> J. E. Sader; *Review of Scientific Instruments* 66, 4583 (1995)
- <sup>110</sup> J. P. Cleveland, S. Manne, D. Bocek, and P. K. Hansma; *Review of Scientific Instruments* 64, 403 (1993)
- <sup>111</sup> S. Timoshenko, and D. H. Young; "Elements of Strength of Materials, 4<sup>th</sup> Ed.", Van Nostrand, New York, 1962, Chap. 1, p. 11.
- <sup>112</sup> R. Berger, E. Delamarche, H. P. Lang, Ch. Gerber, J. K. Gimzewski, E. Meyer, and H.-J. Güntherodt; *Applied Physics A: Materials Science & Processing* 66, S55 (1998)

- <sup>113</sup> J. M. Neumeister, and W. A. Ducker; *Review of Scientific Instruments* 65, 2527 (1994)
- <sup>114</sup> F. Schreiber; *Progress in Surface Science* 65, 151 (2000)
- <sup>115</sup> G. E. Poirier; *Chemical Reviews* 97, 1117 (1997)
- <sup>116</sup> N. Camillone III; *Langmuir* 20, 1199 (2004)
- <sup>117</sup> H. Kondoh; C. Kodama; H. Sumida; and H. Nozoye *Journal of Chemical Physics* 111, 1175 (1999)
- <sup>118</sup> Y. Yourdshahyan; and A. M. Rappe; *Journal of Chemical Physics* 117, 825 (2002)
- <sup>119</sup> T. Hayashi, Y. Morikawa, and H. Nozoye; *Journal of Chemical Physics* 114, 7615 (2001)
- <sup>120</sup> P. Fenter; A. Eberhardt; K.S. Liang; P. Eisenberger *J. Chem. Phys.* **106**, 1600 (1997)
- <sup>121</sup> G. E. Poirier; *Langmuir* 13, 2019 (1997)
- <sup>122</sup> M. H. Dishner, J. C. Hemminger, and F. J. Feher; *Langmuir* 13, 2318 (1997)
- <sup>123</sup> F. Schreiber, A. Eberhardt, T. Y. B. Leung, P. Schwartz, S. M. Wetterer, D. J. Lavrich, L. Berman, P. Fenter, P. Eisenberger, and G. Scoles; *Physical Review B* 57, 12476 (1998)
- <sup>124</sup> C. D. Bain, E. B. Troughton; Y.-T. Tao; J. Evall; G. M. Whitesides; and R. G. Nuzzo; *Journal American Chemical Society* 111, 321 (1989)
- <sup>125</sup> M. Grunze; *Physica Scripta* T49B, 711 (1993)
- <sup>126</sup> J. Noh, and M. Hara; *Langmuir* 17, 7280 (2001)
- <sup>127</sup> J. Noh, and M. Hara; *Langmuir* 18, 1953 (2002)
- <sup>128</sup> G. Hähner, Ch. Wöll, M. Buck, and M. Grunze; *Langmuir* 9, 1955 (1993)
- <sup>129</sup> O. Dannenberger, M. Buck, and M. Grunze; *Journal of Physical Chemistry B* 103, 2202 (1999)
- <sup>130</sup> G. E. Poirier, W. P. Fitts, and J. M. White; *Langmuir* 17, 1176 (2001)
- <sup>131</sup> Although this superstructure should be referred to as the  $p(3 \times 2\sqrt{3})$  superlattice, it is more often referred to as the  $c(4 \times 2)$  superlattice in the literature. We shall refer to this superlattice as  $c(4 \times 2)$  to maintain consistency with the literature.
- <sup>132</sup> H. Kondoh; C. Kodama; H. Sumida; and H. Nozoye; *Journal of Chemical Physics* 111, 1175 (1999)
- <sup>133</sup> P. Schwartz; F. Schreiber; P. Eisenberger; and G. Scoles; *Surface Science* 423, 208 (1999)
- <sup>134</sup> F. Balzer, R. Gerlach, G. Polanski, and H.-G. Rubahn, *Chemical Physics Letters* 274, 145 (1997)
- <sup>135</sup> K. A. Peterlinz, and R. Georgiadis; *Langmuir* 12, 4731 (1996)
- <sup>136</sup> D. S. Karpovich, and G. J. Blanchard; *Langmuir* 10, 3315 (1994)
- <sup>137</sup> R. G. Nuzzo, L. H. Dubois, and D. L. Allara; *Journal of the American Chemical Society* 112, 558 (1990)
- <sup>138</sup> M. Godin, P. J. Williams, V. Tabard-Cossa, O. Laroche, L. Y. Beaulieu, R. B. Lennox, and P. Grütter; *Langmuir* 20, 7090 (2004)
- <sup>139</sup> C. W. Meuse; *Langmuir* 16, 9483 (2000)
- <sup>140</sup> H. Brunner, T. Vallant, U. Mayer, and H. Hoffmann; *Journal of Colloid and Interface Science* 212, 545 (1999)
- <sup>141</sup> A.G. Hansen, M.W. Mortensen, J.E.T. Andersen, J. Ulstrup, A. Kühle, J. Garnæs, and A. Boisen; *Probe Microscopy* 2, 139 (2001)
- <sup>142</sup> G. E. Poirier, and E. D. Pylant; *Science* 272, 1145 (1996)
- <sup>143</sup> M. Buck, M. Grunze, F. Eisert, J. Fischer, and F. Träger; *Journal of Vacuum Science and Technology A* 10, 926 (1992)
- <sup>144</sup> M. Kawasaki, T. Sato, T. Tanaka, and K. Takao; *Langmuir* 16, 1719 (2000)
- <sup>145</sup> S. Xu, J. N. Cruchon-Dupeyat, J. C. Gamo, G.-Y. Liu, G. K. Jennings, T.-H. Yong, and P. E. Laibinis; *Journal of Chemical Physics* 108, 5002 (1998)
- <sup>146</sup> H.-F. Ji, and T. Thundat; *Biosensors & Bioelectronics* 17, 337 (2002)
- <sup>147</sup> A.K. Rappé, C.J. Casewit, K.S. Colwell, W.A. Goddard III, and W.M. Skiff; *Journal of the American Chemical Society* 114, 10024 (1992)
- <sup>148</sup> Gaussian 98; Revision A.9; M. J. Frisch; G. W. Trucks; H. B. Schlegel; G. E. Scuseria; M. A. Robb; J. R. Cheeseman; V. G. Zakrzewski; J. A. Montgomery, Jr.; R. E. Stratmann; J. C. Burant; S. Dapprich; J. M. Millam; A. D. Daniels; K. N. Kudin; M. C. Strain; O. Farkas; J. Tomasi; V. Barone; M. Cossi; R. Cammi; B. Mennucci; C. Pomelli; C. Adamo; S. Clifford; J. Ochterski; G. A. Petersson; P. Y. Ayala; Q. Cui; K. Morokuma; D. K. Malick; A. D. Rabuck; K. Raghavachari; J. B. Foresman; J. Cioslowski; J. V. Ortiz; A. G. Baboul; B. B. Stefanov; G. Liu; A. Liashenko; P.

- Piskorz; I. Komaromi; R. Gomperts; R. L. Martin; D. J. Fox; T. Keith; M. A. Al-Laham; C. Y. Peng; A. Nanayakkara; M. Challacombe; P. M. W. Gill; B. Johnson; W. Chen; M. W. Wong; J. L. Andres; C. Gonzalez; M. Head-Gordon; E. S. Replogle; and J. A. Pople; Gaussian; Inc., Pittsburgh PA, 1998.
- <sup>149</sup> J. B. Foresman; and A. Frisch; "Exploring Chemistry with Electronic Structure Methods, 2<sup>nd</sup> Ed.", Gaussian Inc., 1993.
- <sup>150</sup> The Hartree-Fock approximation is an ab initio method that treats electron correlation (how electrons react to other electrons' position and motion) as an averaged electron density. The term "restricted" refers to the fact that there are no unpaired electrons in the system. The basis set describes the possible orbitals in a system. A complete description of Gaussian98 and of the various model chemistries can be found in reference 149.
- <sup>151</sup> <http://www.webelements.com>
- <sup>152</sup> H. Groenbeck, A. Curioni, and W. Andreoni; *Journal of the American Chemical Society* 122, 3839 (2000)
- <sup>153</sup> W. P. Fitts; J. M. White; and G. E. Poirier; *Langmuir* 18, 1561 (2002)
- <sup>154</sup> C.-C. Kaun; and H. Guo; *Nanoletters* 3, 1521 (2003)
- <sup>155</sup> Results not published; calculations performed by C. C. Kaun and H. Guo at McGill University. The calculations were performed using an ab initio technique which combines the Keldysh non-equilibrium Green's functions with density functional theory, as described in *J. Taylor, H. Guo, and J. Wang Physical Review B* 63, 245407 (2001).
- <sup>156</sup> Surface pressure measurements acquired using Langmuir-Blodgett techniques yield an experimental measure of molecular interactions. The molecular monolayer is compressed as it floats on a liquid subphase (typically water). Changes in surface tension are measured, and are expressed as a surface pressure measurement as a function of molecular area (area per molecule).
- <sup>157</sup> S. H. Gyepi-Garbrah; and R. Silero; *Physical Chemistry Chemical Physics* 4, 3436 (2002)
- <sup>158</sup> A. Grossmann; W. Erley; J. B. Hannon; and H. Ibach; *Physical Review Letters* 77, 127 (1996)
- <sup>159</sup> E. P. M. Leiva; M. G. Del Popolo; and W. Schmickler; *Chemical Physics Letters* 320, 393 (2000)
- <sup>160</sup> M. S. Daw; and M. I. Baskes; *Physical Review B* 29, 6443 (1984)
- <sup>161</sup> C. E. D. Chidsey, and D. N. Loiacono; *Langmuir* 6, 682 (1990)
- <sup>162</sup> R. C. Thomas, L. Sun, and R. M. Crooks; *Langmuir* 7, 620 (1991)